LA-12724-T
Thesis

Magnetohydrodynamic Simulation of Solid-Deuterium-Initiated Z-Pinch Experiments

This thesis was accepted by the Department of Physics, University of California – Los Angeles, Los Angeles, California, in partial fulfillment of the requirements for the degree of Doctor of Philosphy. The text and illustrations are the independent work of the author and only the front matter has been edited by the IS-1 staff to conform with Department of Energy and Los Alamos National Laboratory publication policies.

An Affirmative Action/Equal Opportunity Employer

LA-12724-T
Thesis

UC-700
Issued: February 1994

Magnetohydrodynamic Simulation of Solid-Deuterium-Initiated Z-Pinch Experiments

*Peter Trogdon Sheehey**

*Graduate Research Assistant at Los Alamos Group X-1.

Los Alamos
NATIONAL LABORATORY
Los Alamos, New Mexico 87545

TABLE OF CONTENTS

MAGNETOHYDRODYNAMIC SIMULATION OF SOLID-DEUTERIUM-INITIATED Z-PINCH EXPERIMENTS

by

Peter Trogdon Sheehey

ABSTRACT

Solid-deuterium-initiated Z-pinch experiments are numerically simulated using a two-dimensional resistive magnetohydrodynamic model, which includes many important experimental details, such as "cold-start" initial conditions, thermal conduction, radiative energy loss, actual discharge current vs. time, and grids of sufficient size and resolution to allow realistic development of the plasma. The alternating-direction-implicit numerical technique used meets the substantial demands presented by such a computational task. Simulations of fiber-initiated experiments show that when the fiber becomes fully ionized (at a time depending on current ramp and fiber thickness), rapidly developing m=0 instabilities, which originated in the coronal plasma generated from the ablating fiber, drive intense non-uniform heating and rapid expansion of the plasma column. The possibility that inclusion of additional physical effects would improve stability is explored. Finite-Larmor-radius-ordered Hall and diamagnetic pressure terms in the magnetic field evolution equation, corresponding energy equation terms, and separate ion and electron energy equations are included; these do not change the basic results. Model diagnostics, such as shadowgrams and interferograms, generated from simulation results, are in good agreement with experiment. Two alternative experimental approaches are explored: high-current magnetic implosion of hollow cylindrical deuterium shells, and "plasma-on-wire" (POW) implosion of low-density plasma onto a central deuterium fiber. By minimizing instability problems, these techniques may allow attainment of higher temperatures and densities than possible with bare fiber-initiated Z-pinches. Conditions for significant D-D or D-T fusion neutron production may be realizable with these implosion-based approaches.

CHAPTER 1: INTRODUCTION

1.1 Motivation

The confinement of plasma by the "pinch effect", in which a unidirectional ("z") current generates a self-constricting azimuthal magnetic field, was one of the earliest investigated routes by which it was hoped to reach and sustain conditions of temperature and density sufficient for controlled thermonuclear fusion. Theoretical analysis of the stability of such a confined plasma, based on the ideal magnetohydrodynamic model, seemed to agree with early experimental observations of gas-initiated Z-pinches: rapid development of "sausage" and/or "kink" instabilities disrupted the discharges, long before desired temperatures and densities could be reached[1]. Efforts to stabilize such pinches by employing additional, more elaborate magnetic fields have led to present-day magnetic confinement configurations, such as the tokamak; however, the simplicity and relatively low cost of the Z-pinch have been lost with such elaboration.

Advances in technology have led to the possibility of obtaining conditions quite different from those obtained in the early experiments. This has led to a new round of high density, fast-current-rise Z-pinch experiments. In one such approach, a very fast rising electrical current (peak reached in O(100 nsec)) is discharged through an initially solid deuterium fiber[2-4]. Some discharges of this type appeared to show 'anomalous stability": absence or greatly delayed onset of visible instability development. If this alleged stability were to hold as current is scaled up to the Pease-Braginskii level (the theoretical limit for a Z-pinch discharge, at which ohmic heating is balanced by Bremsstrahlung radiation cooling[5-7]), the Z-pinch could be the basis for a compact and relatively inexpensive fusion reactor[8-10].

Such dense Z-pinches employ modern high-voltage pulsed power technology, capable of producing current ramps approaching the "Haines-Hammel curve" [9,11,12], which in a constant radius plasma column balances ohmic heating, Bremsstrahlung cooling, and temperature/current increase, up to the steady-state Pease-Braginskii current (roughly 1.4 MA for deuterium)[5-7]. Deuterium fiber experiments, with current peaks up to about half the Pease-Braginskii current, reported very long-lived, compact plasmas showing little indication of disruption by m=0 "sausage" or m=1 "kink" instabilities[2-4], based on visible radiation emission and shadowgram images. Second-generation machines[13-15] designed to reach the Pease-Braginskii current, however, have to date shown stronger indication of expansion and m=0 instability growth, in discharges at greater than half the Pease-Braginskii current (700-900 kA) [13,14].

Can it be expected that the apparent stability seen in low-current dense Z-pinches will be retained as current is scaled up? Analytic stability theory is insufficient to answer this question, as the experimental plasmas produced move through a range of non-ideal conditions (a function of temperatures, densities, etc., varying in time and space) more complicated than any stability calculation can handle. If a computational model of the experiment can be constructed in enough detail to accurately depict existing experiments, it can aid in analysing and understanding such experiments, and may further serve as a starting point for the prediction of the results of future experiments. That is the goal of this thesis. It will be seen as this model is assembled, that the "simplicity" of the Z-pinch is a relative concept; inclusion of sufficient capability and detail to accurately model such an experiment is still a very demanding computational task.

1.2 The Computational Modeling Task

The dense Z-pinch is fairly unique among fusion experimental plasmas, in that for a significant fraction of its lifetime, it meets the classical (collisionality) requirements for description as a magnetohydrodynamic (MHD) fluid (see Appendix A). Therefore, a detailed MHD fluid simulation can be expected to reasonably well describe the behavior of such a system. Furthermore, the consistent (but so far unexplained[16]) observation that three-dimensional (3-d) behavior (e.g., growth of m=1 "kink" instabilities) is virtually absent in such experiments (diagnostic images are highly symmetric about the axis, until quite late in the discharge)[2-4,13,14,17] encourages confidence in the results of simulation in only two dimensions. This is fortunate, because the inclusion of vital experimental details discussed below would at present make full 3-d simulation prohibitively expensive.

Linear ideal MHD stability theory for a Z-pinch plasma in general predicts instability to "sausage" (m=0) and "kink" (m=1) modes[18]. However, the growth rate of such instabilities is dependent on radial pressure profiles of the plasma; indeed, "Kadomtsev" profiles exist which are m=0 stable[18]. Linear stability results for a number of non-ideal fluid regimes (such as resistive MHD) have been developed[19-30]. Any actual experiment is likely to move through several of these regimes, as density, temperature, etc., vary during the discharge; nonlinear effects, as well, are likely to be encountered.

Therefore, it is highly desirable to simulate such experiments starting from time zero (zero current, frozen fiber) if possible, in order for realistic plasma profiles to form and develop linearly/nonlinearly, as they will. Energy terms such as thermal conduction, Joule heating and radiation are clearly going to

be important. And the plasma "surface" must be free to develop as if, as in the experiment, in vacuum, without the influence of an unrealistically confining boundary or an insufficiently resolved grid.

Hence one needs a two-dimensional resistive MHD code with classical (Braginskii[31]) heat conduction, ohmic heating and radiation cooling terms in the energy equation, and the capability to deal with huge density and temperature gradients (e.g., solid deuterium vs. hot plasma vs. vacuum), as well as potentially rapidly changing relevant length and time scales, without running into prohibitive numerical timestep restrictions. This suggests that an implicit algorithm, with some capability to adjust time and space step-sizes as the problem develops, will be desirable. Given that such a code can be found or devised, it should be possible to simulate such experiments in a very direct manner. One may then compare the simulation results directly to experiment, by generating from the results predictions of what diagnostics used in the experiments would show. If agreement of simulation and experiment is good, one may begin to use the computational tool developed to interpret experimental results, and to evaluate new experimental concepts with some confidence.

1.3 Early Work and its Limitations

The first efforts by this author to computationally evaluate the "anomalous stability" of fiber Z-pinches employed a 3-d resistive MHD code developed by Schnack and Nebel[23,30,32]. This code had been developed to model the relatively ideal (non-resistive, non-radiative, non-thermally-conductive) magnetohydrodynamics of such controlled fusion research devices as the reversed field pinch, approximating the toroidal configuration of such machines by cylindrical (r, θ, z) geometry with periodic axial boundary conditions. Details of transport–

resistivity, viscosity, heat conduction–were not implemented to follow classical (Braginskii) MHD; however, resistivity, as expressed by the Lundquist number ("S"= $\tau_{resistive\ diffusion}/\tau_{Alfven\ transit}$, an index of the ideality of the plasma), and a scalar ($\nu\nabla^2\vec{v}$) artificial viscosity (both essential to this code for numerical stabilization purposes), were parameters which one could vary to approach expected classical transport properties of a given experiment, such as the fiber Z-pinch. The algorithm was pseudospectral (going between Fourier and normal space representations when each are of greatest utility) in the z and θ directions, and finite-difference in the r direction, with a semi-implicit time advance.

In order to run even a portion of the high-gradient (solid/vacuum) dense Z-pinch problem with this code, it was found necessary to restrict the model to incompressible, resistive MHD: magnetic field and fluid velocity evolution from resistive MHD, with an adiabatic pressure (energy) equation. Resistivity and Lundquist number were set to values of a plasma of near-solid density, at temperatures believed to be reached in the experiments (eV to keV), and the artificial viscosity was set to the corresponding classical (Braginskii ${\eta_0}^{33}$) viscosity (in effect, assuming that the initial condition frozen fiber has evolved to such plasma conditions). The surrounding vacuum was simulated by an area of very high (10^6 times plasma) resistivity and pressure 10^{-2} times the peak pressure of the plasma. Then various radial Z-pinch pressure/field equilibrium profiles (for a Z-pinch, radial pressure/field profiles satisfying $\nabla p(r) = J_z(r) \times B_\theta(r)$) with small perturbations were time-advanced, to measure the growth rate of m=0 and m=1 instabilities. Even with this restricted model and the efficient semi-implicit algorithm of the code, it was clear that run time was going to be a problem; however, it was possible to survey the linear stability of a range of

plasma profiles and temperatures.

The basic results were unchanged even after this author implemented a more sophisticated explicit full (five-coefficient) Braginskii viscous stress tensor[34], and included an ohmic heating term. They were that at low temperature/Lundquist number (i.e., below S$\sim$ 100), resistive field diffusion could act to very much reduce instability growth rates (both m=0 and m=1). This could be part of the explanation for the observed "anomalous stability", if existing experiments actually remained in this regime. This resistive stabilization effect was more pronounced for field/current profiles concentrated at the plasma edge, which from an ideal MHD standpoint would have been expected to be maximally unstable[18]. An ideal-MHD-stable "Kadomtsev profile" was also tested, and did exhibit the theoretically predicted stability; such a profile has center-peaked pressure and current density profiles, quite the opposite extreme from the edge-peaked, resistively stabilized current profiles. At temperatures in the range of 5 keV, the viscous terms were also observed to exert a strong stabilizing effect, but this is of doubtful physical significance, because such a plasma loses its collisionality (an assumption on which the Braginskii viscosities were calculated; discussed further in Chapter 2 and Appendix A) above about 1 keV.

These results were in agreement with other analytic and computational work going on at the time[19–27], but like these other investigations, rather begged the question of dense Z-pinch stability. Yes, various initial profiles and non-ideal effects will make a difference on stability, but into which profiles and effect regimes do the experimental plasmas actually enter? As mentioned above, one clearly desires to be able to evolve plasma profiles as they do in the experiments, from fiber to hot plasma, and allow linear and nonlinear development in a surround-

ing vacuum. The 3-d code, like other computational and analytical tools in use at the time, could suggest possible stabilizing mechanisms; it clearly could not make the key connection between the plethora of theoretical possibilities, and experimental reality.

Lindemuth, McCall, and Nebel began the effort to do a computer "experiment" which corresponded, as much as feasible, to the actual laboratory Z-pinch experiments, first in one dimension and then in two, using a code developed by Lindemuth[35-38]. This code (about which much more will be said later, because it is the starting point for the bulk of the work reported here) could solve the equations of compressible, resistive MHD with an energy equation including classical heat conduction, ohmic heating, and radiative cooling, utilizing a semi-empirical equation of state and material property data base (SESAME[39]) which can be expected to reasonably follow the state of deuterium from solid to hot plasma.

It was possible with this code to run one-dimensional (radial) simulations[35] of the low-current ($\leq 600kA$) Los Alamos and NRL fiber Z-pinch experiments up to times ($\sim$ 200 nsec) well past the discharge current peak, and two-dimensional (r,z) runs[36,37] up to about half the current peak. The results showed some agreement with experiment, such as visible radiation emission (compared to streak photographs), but suggested some controversial features: current was carried largely in a coronal plasma ablated from the fiber surface, of density several orders of magnitude below solid density, while some non-ionized core fiber could persist for a significant fraction of the discharge time (in Los Alamos HDZP-I, 30 to 100 nsec out of a 125-nsec current peak discharge); this coronal plasma tended to show very early instability development, in seeming contradiction to

the "anomalous stability" observations. Several problems would have to be overcome in order to address this controversy with a more definitive, two-dimensional computational model.

1.4 Needed Additions/Enhancements

Lindemuth's code had features and capabilities vital to performing a realistic simulation of a problem such as the fiber-initiated Z-pinch. The basic magnetohydrodynamic model included important details, and the implicit algorithm was robust enough to deal with the huge temperature and density gradients involved, at a reasonable though not insignificant cost in computer time. However, when this author began collaboration with Lindemuth on the problem of dense Z-pinch simulation, there were a number of problems to be solved before two-dimensional simulations of the low current experiments could be extended to larger fractions of the discharge times (e.g., at least to the current peak), much less before high-current planned experiments could be evaluated.

First, very fine radial zoning in the vicinity of the fiber is required to resolve the early stages of fiber ablation, but in 2-d runs, as current increases, the plasma corona expands to many times the original fiber radius and develops instability, making fine zoning desirable at larger radii. When current nears half the discharge peak in an HDZP-I simulation, a significant amount of plasma and current density has reached the computational radial wall, at a radius of about a millimeter. Mass could be allowed to leave through the wall, preventing an unrealistic mass buildup or bounce-back, but the field and current profiles are limited to this radius; hence the free development of instability and expansion in a vacuum-like environment is lost. Fixed grids of much greater than a millimeter would be prohibitively expensive in 2-d.

Second, resolution of the controversy about early onset of instability requires close examination of experimental data. Ideally, given details of experimental diagnostics, generation of corresponding diagnostics from simulation data would allow direct comparison.

Third, as temperatures increase and densities drop, the criterion for the single-temperature MHD model (see Appendix A) approaches the point where ions and electrons cannot be considered in equilibrium, even though the collisional fluid model may still hold. This point may well be reached in high-current fiber Z-pinch discharges, as well as late in low-current experiments. Hence a two-temperature model is desirable.

Fourth, ideal MHD fluid theory orders out the Hall ($\vec{J} \times \vec{B}/(n_e e)$) and diamagnetic pressure terms in Ohm's Law, and accompanying energy equation terms, on the basis of a small ratio of Larmor radius to plasma scale length [40]. That this ratio may not be small in a Z-pinch, with its field null on axis, is well known[19,41]; also, the fiber Z-pinch will have areas of partial ionization, and a low-density corona, in which the Hall term may become important. It is then potentially important to include such terms in a computational evaluation of such experiments.

How these problems have been solved, and the application of the resulting computational tool to the evaluation of existing and proposed solid-deuterium-initiated Z-pinch experiments, are the subjects of the rest of this report. The first step in this, in Chapter 2, is a derivation of the equations actually solved in the model used here, from the generally accepted Braginskii two-fluid plasma transport equations[31]. In Chapter 3, the adaptation of the basic MHD code to model dense Z-pinch experiments is described, along with the results of that

modeling. Addition of the Hall and associated terms to the code, and the results for the dense Z-pinch, are described in Chapter 4. The application of the computational tool developed to the evaluation of some promising variations to the fiber-initiated Z-pinch is the subject of Chapter 5. Finally, the conclusions of this work are summarized in Chapter 6, and some directions for future work are discussed.

CHAPTER 2: DERIVATION OF MODEL EQUATIONS

2.1 Braginskii Collisional Two-Fluid Model

The detailed two-fluid equations of plasma transport derived by S. I. Braginskii[31] from the Landau kinetic equation[42] in the 1950's are still the most widely accepted formulation of the classical plasma transport theory. R. Balescu, in his recent comprehensive book Transport Processes in Plasmas[43], expresses his admiration for, and only limited disagreements with, the Braginskii work. Braginskii's equations for a fully ionized plasma consisting of electrons and a single ion species of charge Ze are (rewritten here in Systeme International–meter, kilogram, second–units, and as vector equations):

$$\frac{\partial n_e}{\partial t} + \nabla \cdot (n_e \vec{v}_e) = 0 \tag{2.1.1}$$

$$\frac{\partial n_i}{\partial t} + \nabla \cdot (n_i \vec{v}_i) = 0 \tag{2.1.2}$$

$$m_e n_e (\frac{\partial \vec{v}_e}{\partial t} + (\vec{v}_e \cdot \nabla)\vec{v}_e) + \nabla p_e + \nabla \cdot \Pi_e + e n_e (\vec{E} + \vec{v}_e \times \vec{B}) = \vec{R} \tag{2.1.3}$$

$$m_i n_i (\frac{\partial \vec{v}_i}{\partial t} + (\vec{v}_i \cdot \nabla)\vec{v}_i) + \nabla p_i + \nabla \cdot \Pi_i - Z e n_i (\vec{E} + \vec{v}_i \times \vec{B}) = -\vec{R} \tag{2.1.4}$$

$$\frac{3}{2} n_e (\frac{\partial T_e}{\partial t} + (\vec{v}_e \cdot \nabla) T_e) + p_e \nabla \cdot \vec{v}_e + \nabla \cdot \vec{q}_e + (\Pi_e : \nabla \vec{v}_e) - Q_e = 0 \tag{2.1.5}$$

$$\frac{3}{2} n_i (\frac{\partial T_i}{\partial t} + (\vec{v}_i \cdot \nabla) T_i) + p_i \nabla \cdot \vec{v}_i + \nabla \cdot \vec{q}_i + (\Pi_i : \nabla \vec{v}_i) - Q_i = 0 \tag{2.1.6}$$

where subscripts e or i refer to electron or ion species, e is the magnitude of charge of an electron, n is particle (number) density, $\vec{v}$ is velocity, $\vec{B}$ is magnetic field, $\vec{E}$

is electric field, p is pressure, T is temperature, Π is the stress tensor (minus, as in Braginskii, the isotropic pressure part), $\vec{R}$ is the momentum transferred from ions to electrons by collisions, $\vec{q}$ is heat flux, Q_e is heat generated in electrons due to collisions with ions, and Q_i is heat generated in ions due to collisions with electrons. Electric and magnetic fields are governed by Maxwell's equations. These equations are for a fully ionized plasma; the simulations reported here also deal with the partially ionized case. How this is accommodated for these, and for the derived single-fluid MHD equations which the computer code employed actually solves, is discussed in section 2.4, below.

It should be noted that Braginskii derives his equations and transport coefficients using the assumption of a collisional plasma[40,43,44], as discussed here in Appendix A. He alludes to the "highly magnetized" regime in which fluid-like equations hold for motions perpendicular to the magnetic field, and supplies transport coefficients for both highly magnetized ($\omega_{cyclotron}\tau_{collision} \gg 1$) and arbitrary $\omega_c\tau$ conditions. The equations and transport coefficients given, however, are for a collisional plasma; the distinction between this and the highly magnetized "collisionless MHD" regime is well discussed in Freidberg[40]. In Appendix A it is argued that the experiments modeled here (and the corresponding simulations) take place substantially in the collisional plasma regime, unlike many controlled fusion experiments (at which one can marvel that MHD predictions work so well, or scoff that MHD ultimately fails to work for such experiments). In general, the code developed here will run outside the collisional regime, and some care has been taken that in this case non-physical results will be avoided (for instance, by employing a cutoff density below which highly resistive, low density "vacuum" plasma regions do not undergo ohmic heating). However, this

author is wary of making claims about MHD simulation results for collisionless plasmas. The modification of this code to give fully consistent physical results in the "collisionless MHD" regime is a worthy subject for further research, but beyond the scope of this thesis.

The full Braginskii two-fluid equations are still a highly nonlinear (particularly in the transport coefficients), strongly coupled set of equations, involving a very wide range of length and time scales. They include the motion of the very low-inertia electron fluid, as well as what is more commonly considered the plasma fluid motion, that of the ion fluid (properly in a one-fluid model, as shall be developed here, fluid motion is that of the center of mass of ions and electrons; in general, because of the much greater mass of the ions, they dominate the fluid motion).

From a computational perspective, these equations present a formidable challenge. Even if one assumes that in a given problem to be computationally modeled, the equations will act relatively linearly (so that primarily linear numerical analysis results might hold), one is faced with two choices, neither of which is likely to be fully satisfactory. An explicit computational algorithm will require excessively small timesteps in order to satisfy Courant-Friedrichs-Lewy (CFL) numerical stability restrictions ($(v_{convective}\Delta t/\Delta x) < 1$) [45] due to the very high speeds of information propagation by the electron plasma fluid; this is carried by electron plasma waves, which transport information at essentially the electron thermal speed[46]. Implicit algorithms are theoretically (for linear equations) numerically stable for any timestep, but if one chooses very large timesteps, the accuracy of the solutions suffers, particularly if important phenomena are occurring at the electron fluid time scale. This author is not aware

of any computational implementation of the complete two-fluid Braginskii equations in more than one dimension. Multi-dimensional particle and kinetic theory codes do exist, which should duplicate all the physics contained in Braginskii's equations (which are derived from such models) and then some, but they too must face the computational difficulties mentioned above.

2.2 Transformation to Center-of-Mass Equations / "Hall MHD"

The model equations used here, in simulating the dense Z-pinch, solve for magnetic field, plasma specific internal energy (either total or separate ion and electron energies), total mass density, and center-of-mass plasma velocity. By solving for total mass density and center-of-mass velocity and using quasineutrality, the need to resolve the full Braginskii model's electron fluid motions is avoided, although it will be seen that the Hall and associated terms do bring some electron fluid effects into the model (in effect, preserving a distinction between electron motion and center-of-mass plasma motion; see Appendix C). Their introduction brings a corresponding price in required temporal resolution. It is instructive to go through the derivation of the model equations from the full Braginskii equations, to highlight the numerous assumptions that must be made to obtain a model with which two-dimensional simulations of these experiments can be carried out. At the end of this chapter, the plasma parameters for the dense Z-pinch, which justify such assumptions, will be worked out.

Define the (total) mass density, $\rho \doteq n_i m_i + n_e m_e$, and the center-of-mass velocity, $\vec{v} = (n_i m_i \vec{v}_i + n_e m_e \vec{v}_e)/(n_i m_i + n_e m_e)$. Before going further, a considerable simplification of the algebra can be gained by invoking the assumption of quasineutrality, that is, $n_i \simeq n_e$. This assumption exploits the fact that the energy required to produce an appreciable separation of the ions from the elec-

trons is so large (much larger than the thermal energy, for regions larger than a Debye length[47], $\lambda_D = (\epsilon_0 kT_e/(ne^2))^{\frac{1}{2}}$; much larger than the magnetic energy, for regions larger than $\lambda_D/\beta^{\frac{1}{2}}$) that no significant deviation of n_i from n_e occurs on scales greater than λ_D: $|n_i - n_e|/(n_i \text{ or } n_e) \ll 1$. By assuming electrons move "quickly" (i.e. instantaneously) to take up their neutralizing positions, the inertia of electrons is ignored (this will be returned to in the Ohm's Law derivation); hence time and length scales dealt with in the model must be much longer than those involving electron inertia, specifically the characteristic times and lengths of the electron cyclotron frequency ($\omega_{ce} = eB/m_e$) and the electron plasma frequency ($\omega_{pe} = (ne^2/(\epsilon_0 m_e))^{\frac{1}{2}}$). The effect of this on the model is to remove Poisson's equation, $\epsilon_0 \bigtriangledown \cdot \vec{E} = e(n_i - n_e)$, from the set of equations, requiring that $\vec{E}$ be obtained by other means; it does not imply that $\vec{E} = 0$ everywhere or that $\bigtriangledown \cdot \vec{E} = 0$, only that $\epsilon_0 \bigtriangledown \cdot \vec{E}/e(n_i \text{ or } n_e) \ll 1$ [48].

Number densities $n_i \simeq n_e$ will thus henceforth be written simply n (except in the Hall and associated terms, for reasons which shall be discussed later). Now mass density is simplified to $\rho = n(m_i + m_e)$, and center-of-mass velocity to $\vec{v} = (m_i\vec{v}_i + m_e\vec{v}_e)/(m_i + m_e)$. Multiplying the Braginskii electron continuity equation by m_e and the ion continuity equation by m_i, adding the two equations, and applying the definitions of mass density and center-of-mass velocity gives the total mass continuity equation:

$$\frac{\partial \rho}{\partial t} + \bigtriangledown \cdot (\rho \vec{v}) = 0 \tag{2.2.1}$$

the first of the model equations.

If one drops the electron inertia term,

$$m_e n_e (\frac{\partial \vec{v}_e}{\partial t} + (\vec{v}_e \cdot \bigtriangledown)\vec{v}_e) \tag{2.2.2}$$

from the Braginskii electron momentum equation and solves for $\vec{E}$, an "Ohm's Law" expression for the electric field can be derived:

$$\vec{E} = \frac{1}{n_e e}(-\nabla p_e - \nabla \cdot \Pi_e + \vec{R}) - \vec{v}_e \times \vec{B}. \tag{2.2.3}$$

The electron viscous stress tensor Π_e, even more so its divergence, $\nabla \cdot \Pi_e$, is a complicated series of terms [49,50]. The leading-order terms (for large $\omega_c \tau$, these are the diagonal terms $\Pi_{e,jj}$) are proportional to Braginskii's electron viscosity coefficient η_0, and to the divergence of the electron velocity[50]:

$$\Pi_{e,jj} \sim \eta_0(2\nabla_{\|} \cdot \vec{v}_{e\|} - \frac{2}{3}\nabla \cdot \vec{v}_e) \sim (n_e T_e \tau_{ee})(\frac{v_{th_e}}{a}) \tag{2.2.4}$$

where v_{th_e} refers to the electron thermal speed, the parallel marks refer to the direction parallel to the magnetic field, and a is a relevant scale length, typically in this problem the effective radius of the plasma column. Then the ratio of $\nabla \cdot \Pi_e$ to ∇p_e is:

$$|\frac{\nabla \cdot \Pi_e}{\nabla p_e}| \sim \frac{(\frac{1}{a}) n_e T_e \tau_{ee}(\frac{v_{th_e}}{a})}{(\frac{n_e T_e}{a})} \sim (\frac{v_{th_e} \tau_{ee}}{a}) \ll 1 \tag{2.2.5}$$

if electron collisionality holds, as established in Appendix A. Exactly the same argument holds for the ratio of $\nabla \cdot \Pi_i$ to ∇p_i (although the ion viscosity effects are a factor of $(m_i/m_e)^{\frac{1}{2}}$ larger than the electron), if the subscripts e for electron quantities are replaced with i for ion quantities; this result will be utilized below in the derivation of the center-of-mass momentum equation.

The above argument somewhat glosses over the complexity of the stress tensor and its divergence: it is conceivable that $\nabla \cdot \vec{v}$, $\nabla \cdot \Pi$, and ∇p will have different scale lengths; and the non-parallel viscosity coefficients η_1 through η_4 can be of the same order as η_0 when $\omega_c \tau \not> 1$ [49,51] (at the end of this chapter it

will be seen that the plasmas modeled here are not generally highly magnetized). There is good reason to place the inclusion of these terms on a lower priority than other terms (such as the Hall and associated terms) which have been included in the present work. Our own early computational results with the Nebel/Schnack code[23] suggest that viscosity (a full five-coefficient stress tensor, or portions of such) does not have a strong stabilizing effect until temperatures are in the several keV range, temperatures so high that the collisionality-dependent Braginskii coefficients are not applicable to the problem under consideration. Parallel computational work by Glasser[23,30] agrees with this result. Furthermore, an attempt to reconcile earlier theoretical and computational results[25,26], which suggested that "viscoresistive" (due to resistivity and viscosity) effects could account for the claimed "anomalous stability" of the experiments modeled here, concluded "viscoresistive effects are inadequate to account for these observations"[29]. Hence one is not confident of seeing much of a payoff in return for the significant amount of work involved in adding $\nabla \cdot \Pi$ to a code, particularly if one maintains energy consistency by adding viscous heating, $(\Pi : \nabla \vec{v})$, to the energy equation as well.

Bowers and Haines[52] and others have developed fluid equations for a collisionless, magnetized plasma which include finite-Larmor-radius (FLR) ordered viscous stress terms, related to the Braginskii "gyroviscous" non-diagonal stress terms (his η_3 and η_4[33,53]). Haines has projected[22,54] that the nominally 2-MA fiber-pinch machine "MAGPIE", recently completed at Imperial College, may take a Z-pinch into the regime where these are important, unlike the (largely collisional) experiments modeled here. Simulating such a plasma would then call for a consistent "collisionless MHD" model, which among its FLR effects should include such viscous stress terms, as well as the Hall and associated terms which

are included in the present collisional, finite-Larmor-radius "Hall MHD" model. It has been argued that for high $\omega_c\tau$, the Braginskii "gyroviscous" stress terms [33,53] become independent of collision time. However, it will be seen that when typical ion and electron $\omega_c\tau$'s are computed for the experiments modeled here, the large $\omega_c\tau$ assumption necessary to consider these gyroviscous stress terms independent of collisions is not satisfied, so it is consistent for these to be ignored, as long as collisionality holds.

$\vec{R}$, the change in momentum of electrons due to electron-ion collisions, can reasonably be related to the relative velocity of the two species, $\vec{v}_e - \vec{v}_i$, which is proportional to the current density[55,56]:

$$\vec{J} = n_i e\vec{v}_i - n_e e\vec{v}_e = ne(\vec{v}_i - v_e). \tag{2.2.6}$$

In the case of a plasma without a magnetic field, the constant of proportionality between $\vec{R}$ and $\vec{J}$ is a scalar, and can be written so that

$$\vec{R} = \eta n_e e\vec{J} \tag{2.2.7}$$

where η is the electrical resistivity of the plasma. In the case, such as dealt with in this paper, of a plasma with a magnetic field, the relationship between $\vec{R}$ and $\vec{J}$ is a tensor relationship, with a resistivity (or its inverse, a conductivity) tensor. This is because the magnetic field introduces an anisotropy into the plasma: particle motion parallel to the field will be unaffected, because of the nature of the Lorentz $\vec{v}_\alpha \times \vec{B}$ force (and in fact the parallel resistivity will be identical to the unmagnetized one), but particle motion perpendicular to $\vec{B}$ is influenced by $\vec{B}$ and must be dealt with separately, resulting in different resistivity coefficients. Due to the symmetry of the problem[57], there can be only three

independent coefficients: resistivities parallel and perpendicular to the field, and a non-diagonal effective resistivity, relating current in one direction to electric field in another direction. This non-diagonal effective resistivity in fact leads to the Hall effect, which has already been incorporated (i.e., separated out from $\vec{R}$) in the Braginskii transport equations, and will be pointed out shortly.

Braginskii[58] and others[57] also discuss non-diagonal thermoelectric effects (Nernst and Ettinghausen effects) which are due to ion-electron collisions. The ordering of these effects is not simple. As $\omega_c\tau$ gets much larger than one, a $1/(\omega_c\tau)$ dependence emerges (as in all the non-diagonal transport coefficients, including the above-mentioned gyroviscous coefficients; in the gyroviscous case, an additional τ factor can cancel out the collision time dependence). These thermoelectric effects are also dependent upon electron density, the gradient of temperature, and $\vec{J} \times \vec{B}$. Chittenden and Haines[59] in a recent paper state that these effects "cannot be ignored when electron and ion temperatures are sufficiently decoupled." They have not been implemented in the present model; some implications of the Chittenden/Haines work will be discussed later. Replacing the $(1/(n_e e))\vec{R}$ term in the Ohm's Law with the two diagonal components of the resistivity tensor (additionally dropping the $\nabla \cdot \Pi_e$ term) then gives

$$\vec{E} = \frac{1}{n_e e}(-\nabla p_e) + \eta_{\parallel}\vec{J}_{\parallel} + \eta_{\perp}\vec{J}_{\perp} - \vec{v}_e \times \vec{B}. \tag{2.2.8}$$

Using the definitions given above of current density $\vec{J}$ (2.2.6) and center-of-mass velocity $\vec{v}$ (above 2.2.1), and using $n_e = n_i = n$, one can solve for $\vec{v}_e$ and $\vec{v}_i$ in terms of $\vec{v}$ and $\vec{J}$. Here we use

$$\vec{v}_e = \vec{v} - \frac{\vec{J}}{n_e e(1 + \frac{m_e}{m_i})} \simeq \vec{v} - \frac{\vec{J}}{n_e e} \tag{2.2.9}$$

where the m_e/m_i factor for a deuterium plasma (approximately 1 over 3698) can be dropped with very little effect, to give an Ohm's Law:

$$\vec{E} = \frac{1}{n_e e}(\vec{J} \times \vec{B} - \nabla p_e) + \eta_{\parallel}\vec{J}_{\parallel} + \eta_{\perp}\vec{J}_{\perp} - \vec{v} \times \vec{B}. \tag{2.2.10}$$

This is the "Hall MHD" Ohm's Law, where specifically $(1/n_e)\vec{J} \times \vec{B}$ is known as the Hall term.

Neither $\vec{J}$ nor $\vec{E}$ is solved as a separate variable in the model used here. Faraday's Law can be used to transform the above Ohm's Law into an equation for the time evolution of magnetic field, removing $\vec{E}$:

$$\frac{\partial \vec{B}}{\partial t} = -\nabla \times \vec{E} = -\nabla \times (\frac{1}{n_e e}(\vec{J} \times \vec{B} - \nabla p_e) + \eta_{\parallel}\vec{J}_{\parallel} + \eta_{\perp}\vec{J}_{\perp} - \vec{v} \times \vec{B}). \tag{2.2.11}$$

Finally, the usual "low-frequency" assumption of magnetohydrodynamics neglects the displacement current in the full Ampere's Law, i.e.,

$$-\vec{J} + \frac{(\nabla \times \vec{B})}{\mu_0} = \epsilon_0 \frac{\partial \vec{E}}{\partial t} = 0. \tag{2.2.12}$$

This requires that electromagnetic disturbances of interest have phase velocities (such as the Alfven speed, $v_A = B/(\mu_0 \rho)^{\frac{1}{2}}$) much less than the speed of light, as must be the thermal speeds. Note that the restricted geometry employed in the model (discussed in section 2.4), that $\vec{B}$(r,z) $\perp$ plane of computation, removes many possible waves (such as ion cyclotron waves) from the problem. Then using $\vec{J} = (\nabla \times \vec{B})/\mu_0$,

$$\frac{\partial \vec{B}}{\partial t} = -\nabla \times (\frac{1}{n_e e}((\frac{\nabla \times \vec{B}}{\mu_0}) \times \vec{B} - \nabla p_e) + \eta_{\parallel}\vec{J}_{\parallel} + \eta_{\perp}\vec{J}_{\perp} - \vec{v} \times \vec{B}). \tag{2.2.13}$$

This is the "Hall MHD" equation for advancing the magnetic field.

The two Braginskii momentum equations must be added to obtain a center-of-mass momentum equation. The two viscous stress divergences are dropped,

following the above argument that their respective pressure gradients will dominate. The forces due to $\vec{E}$ cancel out under charge neutrality, that is, $Zn_i = n_e$ (the quasineutral deuterium plasma generally discussed here has $Z = 1$ and hence $n_i = n_e$). Now first in the $\vec{v}_{i\,or\,e} \times \vec{B}$ expressions, substitute for $\vec{v}_e$ (as above, 2.2.9) in terms of $\vec{v}$ and $\vec{J}$, and for $\vec{v}_i$ by the corresponding expression:

$$\vec{v}_i = \vec{v} + \frac{\vec{J}}{n_i e(1 + \frac{m_i}{m_e})} = \vec{v} + (\frac{m_e}{m_i + m_e})\frac{\vec{J}}{n_e e} \tag{2.2.14}$$

(where writing the second expression will be seen to be helpful in ordering terms, shortly). A number of terms cancel out, leaving:

$$m_e n_e(\frac{\partial \vec{v}_e}{\partial t} + (\vec{v}_e \cdot \nabla)\vec{v}_e) + m_i n_i(\frac{\partial \vec{v}_i}{\partial t} + (\vec{v}_i \cdot \nabla)\vec{v}_i) + \nabla \cdot (p_i + p_e) + \\ -(1 + \frac{m_e}{m_i})\vec{J} \times \vec{B} = 0. \tag{2.2.15}$$

At this point, substituting $\vec{v}_e(\vec{v}, \vec{J})$ and $\vec{v}_i(\vec{v}, \vec{J})$ in the inertial (convective derivative) expressions, further cancellation, and replacing $(m_i + m_e)n$ with ρ gives:

$$\frac{\partial(\rho\vec{v})}{\partial t} + \rho(\vec{v} \cdot \nabla)\vec{v} + \vec{v}\,\nabla \cdot (\rho\vec{v}) + \nabla(p_i + p_e) - \vec{J} \times \vec{B} + \\ +(terms\ proportional\ to\ m_e) = 0. \tag{2.2.16}$$

Dropping the electron-mass-order terms, writing $\vec{J}$ in terms of $\vec{B}$, and use of a tensor identity[60] gives:

$$\frac{\partial(\rho\vec{v})}{\partial t} + \nabla \cdot (\rho\vec{v}\vec{v}) + \nabla(p_i + p_e) - (\frac{\nabla \times \vec{B}}{\mu_0}) \times \vec{B} = 0 \tag{2.2.17}$$

This is the model momentum equation; using the dyadic tensor "$\rho\vec{v}\,\vec{v}$" form has been found helpful in coding the equation in a conservative form[61].

One can multiply the Braginskii continuity equations (2.1.1, 2.1.2) by $\frac{3}{2}kT_\alpha$ and add them (because these still equal 0) to the first terms of the respective

Braginskii energy equations (2.1.5, 2.1.6), to obtain energy equation terms in conservative form:

$$\frac{3}{2}n_\alpha\left(\frac{\partial T_\alpha}{\partial t}+(\vec{v}_\alpha\cdot\nabla)T_\alpha\right)=\frac{\partial(\frac{3}{2}n_\alpha kT_\alpha)}{\partial t}+\nabla\cdot\left(\frac{3}{2}v_\alpha n_\alpha kT_\alpha\right) \tag{2.2.18}$$

where subscripts α refer to electron or ion species. The code used here solves for the specific internal energy ϵ_α (energy per unit mass); energy per unit volume, which in Braginskii (ideal gas) is $\frac{3}{2}n_\alpha kT_\alpha$, is in these terms $\rho\epsilon_\alpha$. Then the first terms in the Braginskii energy equations can be written

$$\frac{\partial(\rho\epsilon_\alpha)}{\partial t}+\nabla\cdot(\vec{v}_\alpha\rho\epsilon_\alpha). \tag{2.2.19}$$

The heat fluxes q_α, analogously to the discussion of the resistivity tensor, have parallel (to $\vec{B}$), perpendicular, and off-diagonal components. Heat fluxes coupled to the previously mentioned (and neglected) off-diagonal thermoelectric effects (Nernst/Ettinghausen effects), and diagonal thermoelectric heat fluxes (Balescu discusses "thermoelectric coefficients", relating $\vec{E}$ and heat flux[62]), are not included in the present model. This leaves the more familiar "Fourier's Law"-type heat conduction, again split into components parallel and perpendicular to $\vec{B}$:

$$\vec{q}_\alpha=\kappa_{\alpha\parallel}\nabla_\parallel T_\alpha+\kappa_{\alpha\perp}\nabla_\perp T_\alpha \tag{2.2.20}$$

where κ_α's are prescribed by Braginskii[63] (the formulas used are given in section 3.1).

Of course if viscous stress is neglected, as discussed above, the viscous heating terms ($\Pi_\alpha:\nabla\vec{v}_\alpha$) also drop out. Collisional heat source terms, Q_α, follow Braginskii[64]: both include an electron-ion energy equilibration term Q_{ei}

($3m_e n_e(T_e - T_i)/(m_i \tau_{ee})$; note the inverse $\tau_{ee} m_i/m_e$ dependence, characteristic of the electron-ion collision time τ_{ei}[65]), while the electron heat source also includes ohmic heating, $\eta_\parallel {J_\parallel}^2 + \eta_\perp {J_\perp}^2$, but does not include any thermoelectric heating. This leaves only the compressional work terms, $p_\alpha \bigtriangledown \cdot \vec{v}_\alpha$, and the replacement of $\vec{v}_i$ and $\vec{v}e$ by their expressions in terms of $\vec{v}$ and $\vec{J}$. After rearranging, the energy equations (2.1.5, 2.1.6) become:

$$(2.2.21) \quad \frac{\partial(\rho\epsilon_e)}{\partial t} + \bigtriangledown \cdot (\vec{v}\rho\epsilon_e) + \bigtriangledown \cdot ((\frac{-\vec{J}}{n_e e})\rho\epsilon_e) + p_e \bigtriangledown \cdot \vec{v} + p_e \bigtriangledown \cdot (\frac{-\vec{J}}{n_e e}) +$$

$$-\bigtriangledown \cdot (\kappa_{e\perp} \bigtriangledown_\perp T_e + \kappa_{e\parallel} \bigtriangledown_\parallel T_e) - \eta_\perp {J_\perp}^2 - \eta_\parallel {J_\parallel}^2 + Q_{ei} = 0.$$

$$(2.2.22) \quad \frac{\partial(\rho\epsilon_i)}{\partial t} + \bigtriangledown \cdot (\vec{v}\rho\epsilon_i) + p_i \bigtriangledown \cdot \vec{v} +$$

$$-\bigtriangledown \cdot (\kappa_{i\perp} \bigtriangledown_\perp T_i - \kappa_{i\parallel} \bigtriangledown_\parallel T_i) - Q_{ei} = 0$$

where Q_{ei} is the electron-ion energy equilibration term (energy lost from electrons to ions), $\vec{J} = (\bigtriangledown \times \vec{B})/\mu_0$, and the two terms in the ion equation proportional to $m_e/(m_i + m_e)$ have been dropped,

$$(2.2.23) \quad (\frac{m_e}{m_i + m_e}) \bigtriangledown \cdot ((\frac{\vec{J}}{n_e e})\rho\epsilon_i) + (\frac{m_e}{m_i + m_e}) p_i \bigtriangledown \cdot (\frac{\vec{J}}{n_e e}).$$

These are the "Hall MHD" (two-temperature) energy equations.

If one makes the further assumption of temperature equilibration ($T_i = T_e$, $p_i = p_e$, $\epsilon_i = \epsilon_e$, $p = p_i + p_e$, $\kappa = \kappa_i + \kappa_e$, and $\epsilon = \epsilon_i + \epsilon_e$) and adds the two energy equations, the total energy equation is:

$$(2.2.24) \quad \frac{\partial(\rho\epsilon)}{\partial t} + \bigtriangledown \cdot (\vec{v}\rho\epsilon) + \bigtriangledown \cdot ((\frac{-\vec{J}}{n_e e})\rho\epsilon_e) + p \bigtriangledown \cdot \vec{v} + p_e \bigtriangledown \cdot (\frac{-\vec{J}}{n_e e}) +$$

$$-\bigtriangledown \cdot (\kappa_\perp \bigtriangledown_\perp T + \kappa_\parallel \bigtriangledown_\parallel T) - \eta_\perp {J_\perp}^2 - \eta_\parallel {J_\parallel}^2 = 0.$$

The above developed equations for the time development of mass (2.2.1), momentum (2.2.17), energy (2.2.21 and 2.2.22, or single-temperature 2.2.24), and magnetic field (2.2.13) constitute the "Hall MHD" model used here in simulation of dense Z-pinches (the geometric restriction, that $\vec{B}$(r,z) $\perp$ plane of computation, discussed in section 2.4, eliminates the parallel resistivity and parallel heat conduction terms). The equations are valid subject to the numerous assumptions mentioned. These assumptions will be summarized and examined for the dense Z-pinch at the end of this chapter. Quotes are used in this paper around "Hall MHD" to distinguish this model from the Hall MHD, dealt with by numerous authors[19,66,67], which includes only the magnetic or electric field Hall term, $\vec{J} \times \vec{B}/(n_e e)$. The other terms (diamagnetic pressure and associated energy equation terms) included here shall be shown in the next section to have the same ordering as the Hall term.

2.3 Elimination of Finite-Larmor-Radius Terms/Standard MHD

The equations derived in section 2.2 represent a relatively standard single-fluid MHD model, with the following exceptions. Ideal MHD drops the resistive field diffusion and ohmic heating terms. Many MHD simulations use a simpler energy equation, isothermal or adiabatic, because the Braginskii heat conduction coefficients, which can be drastically different parallel and perpendicular to the magnetic field, can present numerical difficulties. These difficulties are geometrically avoided in the simulations done here, as will be pointed out in section 2.4. When the Hall term is included in the magnetic field evolution, this is generally termed Hall MHD. Sometimes the diamagnetic pressure term ($\nabla p_e/(n_e e)$) is also included, but it will be shown shortly that unless the $p_e \nabla \cdot(-\vec{J}/(n_e e))$ energy equation term is also included, total (thermal plus magnetic) energy will not be

conserved. The electron-current energy convection term $\nabla \cdot (\rho \epsilon_e (-\vec{J}/(n_e e)))$ is rarely included, although Haines[68,69] has done some theoretical work with it, notably a calculation of tolerable energy end-losses for a fusion Z-pinch[70]. In this thesis, the Hall, diamagnetic pressure, and the two just-mentioned energy equation terms are referred to as "Hall and associated terms." It will be shown that these all have a similar, finite-Larmor-radius ordering; hence a consistent finite-Larmor-radius model should include them all.

Some vector algebra will illustrate the above-mentioned problem of conservation of total energy when the Hall and diamagnetic pressure terms are included. These terms' effect on the time derivative of magnetic energy, $B^2/(2\mu_0)$, is proportional to $\vec{B} \cdot (\partial \vec{B}/\partial t)$, hence to $\vec{B} \cdot (\nabla \times \vec{E}_H)$, where $\vec{E}_H$ is the electric field due to the Hall and diamagnetic pressure terms. A vector identity gives

$$\vec{B} \cdot (\nabla \times \vec{E}_H) = \nabla \cdot (\vec{E}_H \times \vec{B}) + \vec{E}_H \cdot (\nabla \times \vec{B}). \tag{2.3.1}$$

The first term, a divergence, is already in conservative form for an equation giving the time development of magnetic energy; that is to say, if one spatially integrates the divergence in order to obtain the change in magnetic energy $\partial(B^2)$ in time ∂t, by Gauss's theorem that integral will be the sum of the fluxes of $\vec{E}_H \times \vec{B}$ across the surface of the volume integrated. The second term becomes

$$\vec{E}_H \cdot \vec{J} = \frac{1}{n_e e}(\vec{J} \times \vec{B} - \nabla p_e) \cdot \vec{J} = \frac{-1}{n_e e} \nabla p_e \cdot \vec{J}. \tag{2.3.2}$$

If the equation for magnetic energy is added to the thermal energy equation, one should still have conservation of total energy, but this term is clearly not in conservative form. However, if the $p_e \nabla \cdot (-\vec{J}/(n_e e))$ term has been included in the thermal energy equation, it can be added to the offending magnetic energy

term, to obtain the desired conservative form:

$$p_e \nabla \cdot (\frac{-\vec{J}}{n_e e}) - \frac{1}{n_e e} \nabla p_e \cdot \vec{J} = \nabla \cdot (p_e(\frac{-\vec{J}}{n_e e})). \tag{2.3.3}$$

The ∇p and $\vec{J} \times \vec{B}$ terms are both in the momentum equation and should be comparable; in fact, for an isotropic equilibrium with $\vec{v} = 0$, these terms should be equal (hence the "pressure balance" expression $p_{B=0} = {B_{p=0}}^2/(2\mu_0)$). Therefore, the ratio of the diamagnetic pressure term to the $\vec{v} \times \vec{B}$ term in the Ohm's Law expression (2.2.10), should be similar to the ratio of the Hall term to $\vec{v} \times \vec{B}$. A characteristic fluid speed to use in such scaling is the ion thermal speed[71] $v_{th_i} = (kT_i/m_i)^{\frac{1}{2}}$; one might prefer the Alfven speed $v_A = B/(\mu_0 \rho)^{\frac{1}{2}}$, but under pressure balance $p = nkT \simeq B^2/2\mu_0$, this scales the same way (in section 2.5 it will be seen that these quantities are similar for the dense Z-pinch). Then for a plasma near temperature equilibrium ($T_i \sim T_e$):

$$\frac{|\nabla p_e/(n_e e)|}{|\vec{v} \times \vec{B}|} \sim \frac{\frac{1}{a} n_e k T_e/n_e e}{(kT_i/m_i)^{\frac{1}{2}} B} \sim \frac{r_{Li}}{a} \tag{2.3.4}$$

where $r_{Li} = v_{th_i}/\omega_{ci} = m_i v_{i\perp}/(eB)$ is the ion Larmor radius.

Using similar scaling, that $J \sim \nabla p/B$ and that $\partial(\rho\epsilon)/\partial t$ goes as $nkT v_{th_i}/a$ (again for a near-temperature-equilibrium, $T_i \sim T_e$, and quasineutral, $n_i \sim n_e$, plasma), the ratios of the electron "work" term $p_e \nabla \cdot (-\vec{J}/(n_e e))$ and the electron current energy convection term $\nabla \cdot (\rho\epsilon_e(-\vec{J}/(n_e e)))$, to the time derivative of thermal energy $\partial(\rho\epsilon)/\partial t$, are also shown proportional to ion Larmor radius over scale length:

$$\frac{|\nabla \cdot (\rho\epsilon_e(-\vec{J}/(n_e e)))|}{|\partial(\rho\epsilon)/\partial t|} \sim \frac{\frac{1}{a} n_e k T_e (nkT/aB)/n_e e}{nkT v_{th_i}/a} \sim \frac{r_{Li}}{a}; \tag{2.3.5}$$

$$\frac{|p_e \nabla \cdot (-\vec{J}/(n_e e))|}{|\partial(\rho\epsilon)/\partial t|} \sim \frac{n_e k T_e \frac{1}{a} (nkT/aB)/n_e e}{nkT v_{th_i}/a} \sim \frac{r_{Li}}{a}. \tag{2.3.6}$$

Hence if $(r_{Li}/a) \ll 1$ in the plasma to be modeled, these terms can be ignored. This reduces our model equations to a relatively standard one-fluid resistive MHD, with perhaps a more detailed energy equation (including heat conduction) than is often used. It will be seen that for the dense Z-pinch, $(r_{Li}/a) \ll 1$ is not necessarily a good assumption. This has motivated our efforts to add the Hall and associated terms to the computational model. However, simulation of dense Z-pinches with the standard MHD model presented in the next chapter, still shows remarkably good agreement to experiment.

2.4 Additional Details

There are a number of additional details concerning the model used here which should be noted. First, as mentioned in Chapter 1, is the geometrical simplification to cylindrical symmetry. The computational model is two-dimensional, solving for mass density, radial and axial velocities, specific internal energy (or separate ion and electron energies), and azimuthal magnetic field, as functions of radius r and axial location z only; i.e., azimuthal symmetry is assumed. Experimental evidence that this is a good assumption, at least for a significant portion of the experiments, has already been noted [2-4,13,14,17]. Because quantities are computed only in the plane perpendicular to $\vec{B}$, terms proportional to parallel resistivity (parallel field diffusion and ohmic heating) and parallel heat conductivity are not needed; hence the scales of resistivity and heat conductivity with which the numerics must deal, depend only on the perpendicular values.

The Braginskii transport equations, and the single-fluid models derived above, assume a fully ionized plasma. The intent of the simulations done here is to follow these experiments all the way from "cold-start", that is, the solid,

neutral deuterium fiber, up to the hot, fully ionized plasma state. To allow this with a Braginskii-like set of equations would require additional equations for the density, momentum, and energy of the third, neutral fluid species. A means of relating the neutral and plasma densities, such as the Saha equation[72], would be necessary (this would be reflected in "source terms" in the continuity equations), as would be other terms coupling the neutral and plasma equations. Details of transport (e.g. resistivity), which were calculated by Braginskii for a fully ionized plasma, would need to be re-examined for the neutral-dominated case.

To allow "cold-start" simulations with the derived, single-fluid model equations, an assumption is made that neutral atoms will move as the ions do: $\vec{v}_n = \vec{v}_i$, i.e., no ion-neutral slip. Center-of-mass velocity $\vec{v}$ is then redefined as $\vec{v} = (n_n(m_i + m_e)\vec{v}_n + n_i m_i \vec{v}_i + n_e m_e \vec{v}_e)/(n_n(m_i + m_e) + n_i m_i + n_e m_e)$, and total mass density $\rho = n_n(m_i + m_e) + n_i m_i + n_e m_e$. When $\vec{v}_e$ and $\vec{v}_i$ in terms of the redefined $\vec{v}$ (with $\vec{v}_n = \vec{v}_i$) and $\vec{J}$ are incorporated into the derived equations, the results are very little different from the original derivation; terms proportional to $m_e/(m_i + m_e)$, which were dropped, are still small quantities, proportional to $n_e m_e/\rho$. The meanings of $\rho\epsilon$ (or, in a two-temperature model, $\rho\epsilon_i$) and p (or p_i; also T_i) have changed: these are now quantities including energy and pressure due to neutral particles. Appropriate values for these quantities are obtained from equation(s) of state (relating specific internal energy, density, and temperature), pressure(s), resistivity, and average ionization level, contained in a semi-empirical data base, the Los Alamos SESAME tables[39], which provide the best available (to my knowledge) values for such quantities over the wide range of temperatures and densities covered. The SESAME energies and pres-

sures include the effects of energy going into phase changes and ionization, which a simple ideal gas model does not; it is remarkable, however, how closely these quantities follow the ideal gas values from 0 K up to the fully ionized plasma state. MHD runs were done using ideal gas temperatures and pressures, and very little difference could be seen from those done with SESAME values.

In the "Hall MHD" model used here, correct values of p_e, ϵ_e, and n_e, which in conditions of partial ionization can be substantially less than total pressure, energy, or number density values, have been incorporated. This is done by obtaining the average ionization fraction "zb" as a function of mass density and temperature from the SESAME table, then computing $n_e = zb\,\rho/(m_i + m_e)$, $\epsilon_e = \epsilon\,zb/(1 + zb)$, and $p_e = p\,zb/(1 + zb)$.

Braginskii's transport equations do not include an energy loss term for radiative effects. The Z-pinches modeled here were designed to reach conditions where radiative cooling is very significant in the energy balance. An energy loss term is incorporated in the energy equation (electron energy equation, in the two-temperature case) to account for this. The values are also obtained from SESAME tables[39], and include line and Bremsstrahlung radiation.

2.5 Dense Z-Pinch Plasma Parameters

In Appendix A, the case is made that the dense Z-pinch experiments modeled here exist for significant times in the collisional regime in which Braginskii's transport equations are valid. To go from those equations to the single-fluid equations actually used in the simulations (as is done in this chapter), a number of additional assumptions have been pointed out. Quasineutrality and the dropping of the electron inertia require that plasma scale lengths be greater than the Debye length, and that time scales be greater than electron cyclotron or electron

plasma oscillation times. Further, the "low-frequency" assumption (dropping of displacement current) requires that characteristic speeds of important disturbances, such as the Alfven speed or ion thermal speed, be much less than the speed of light. If the standard MHD equations are to hold, the ion Larmor radius should be much less than plasma scale lengths; otherwise, the "Hall MHD" model should be used.

The scale length a used here is typically the radius of the plasma column, which can vary from tens of microns to several millimeters or more. For a given radius, other plasma quantities can be estimated. For instance, the small radii occur generally very early in the discharge, when temperatures and fields/currents are relatively low; larger radii occur when the plasma has expanded, and may correspond to lower densities. Thus one needs to compute the desired plasma parameters for a range of plasma conditions. For given parameters' functional dependencies, it may be possible to compute "worst-case" values, that is, the combination of conditions (temperature, density, etc.) which can occur in the plasma, which will give the parameter value closest to violating an assumption.

The Debye length[73], $\lambda_D = (\epsilon_0 k T_e / n e^2)^{\frac{1}{2}} = 7.4 (T_{eV} / n_{cm^{-3}})^{\frac{1}{2}}$ m, will be largest at high temperature and low density. The highest temperature at which the fluid model for these simulations can generally be taken seriously is about 1000 eV, and the lowest density is about 10^{-4} solid, or $O(10^{18}$ cm$^{-3})$. This gives a λ_D of about 2×10^{-7} m., much less than the smallest radius, about 10^{-5} m.

Characteristic times for comparison to the electron cyclotron or plasma oscillation times, can be derived by dividing characteristic speeds–thermal speed or Alfven speed–into the scale length a. The "worst-case" thermal speeds, of course, occur for the electron fluid at the highest temperatures; 1000 eV corresponds to

a $v_{th_e} \simeq 2 \times 10^7$ m/sec. Dividing this into the smallest scale length, $\sim 2 \times 10^{-5}$ m, the characteristic time is about 10^{-12} sec. This compares to a slowest plasma oscillation time (for the smallest density, 10^{18} cm^{-3}), of $1/\omega_{pe} \sim 10^{-13}$ sec; the comparison for higher densities or slower ion motion will be much more favorable. The ion thermal speed for 1000 eV is about 3×10^5 m/sec. If one assumes pressure balance ($p = B^2/2\mu_0$) to obtain field and density values with which to compute an Alfven speed ($B/(\mu_0 \rho)^{\frac{1}{2}}$), it will be of the same order as ion thermal speed. "Worst-case" Alfven speeds, for fields of 20 megagauss at densities of 10^{18} cm^{-3} ($\rho \sim 10^{-2}$ kg/m^3) still are of the order 10^7 m/sec. Hence these ion motion times will be larger than the electron plasma oscillation time (and ion motions will be slower). These ion speeds are generally much less than the speed of light, satisfying the "low-frequency" assumption.

The electron cyclotron time $1/\omega_{ce} = m_e/eB$ for a 20 megagauss field is $O(10^{-15})$ sec, and the electron Larmor radius for such a field at 1000 eV is $O(10^{-8})$ m. These are well below the characteristic scale times and lengths of the plasma modeled. Of course, in a Z-pinch the field goes to 0 at r=0, so the cyclotron times and Larmor radii become large (Z-pinch particle orbits in the vicinity of the origin are actually of more complexity than a simple "Larmor radius" orbit, as pointed out by Haines[70]). Hence the zero-electron-inertia requirement, that electron cyclotron times and lengths be much less than plasma scale times and lengths, may be questionable near the origin, although this area is surrounded by a plasma which does satisfy this assumption. The plasmas modeled here do remain collisional near the origin, where the density remains relatively high (for a near-solid density plasma at 1000 eV, the mean free path is $O(10^{-4}$ cm)), until very deep instability development sets in (collisionality is

further discussed in Appendix A).

Ion Larmor radii, even for the conditions (20 megagauss, 1000 eV) which satisfied the small gyroradius assumption for electrons, are relatively large: on the order of microns, approaching the initial fiber/plasma column radius (as small as 15 μ). The above-mentioned worsening of this ratio as the origin is approached, is thus much more serious, where r_{Li}/a is concerned. Hence inclusion of the r_{Li}/a ordered terms, as done in the "Hall MHD" model here, is important.

Typical like-particle collision times (proportional to $T_\alpha^{\frac{3}{2}}/n_\alpha$) are calculated here for two extreme conditions: 1) "core" plasma: 100 eV, solid density ($\sim 5 \times 10^{22} cm^{-3}$, in which case $\tau_{ee} \sim 10^{-16}$ sec, and $\tau_{ii} \sim 10^{-14}$ sec; 2) "coronal plasma": 1000 eV, density 5×10^{18} cm^{-3}, in which case $\tau_{ee} \sim 10^{-10}$ sec, and $\tau_{ii} \sim 10^{-8}$ sec. Hence τ_{ee} values may range from 10^{-10} to 10^{-16} sec, while τ_{ii} values range from 10^{-8} to 10^{-14} sec. Above, an electron cyclotron frequency of 10^{15} sec^{-1} was calculated; for the same, 20-megagauss field, the ion cyclotron frequency will be O(10^{11} sec^{-1}). Hence $\omega_{ce}\tau_{ee}$ values may range from 10^{-1} to 10^5, and $\omega_{ci}\tau_{ii}$ values from 10^{-3} to 10^3. It is thus not safe to assume $\omega_\alpha \tau_\alpha \gg 1$, to justify the use of some simplified transport coefficients or a "collisionless MHD" model, requiring $\omega_\alpha \tau_\alpha \gg 1$.

Although it is here indicated that the "Hall MHD" model is of greater validity than the basic MHD (negligible Larmor radius) model, the results of simulation using the basic MHD model will be presented first. It will be seen that, even with the basic MHD model, reasonably good agreement with experiment has been obtained.

CHAPTER 3: MHD MODELING OF HDZP-I AND HDZP-II

3.1 Detailed Basic MHD Model of Experiments

The primary experiments modeled here were performed on the Los Alamos High Density Z-Pinch (HDZP) machines HDZP-I[3,4] and -II[4,14]. These machines employed Marx bank generators with water-insulated pulse-forming networks to apply maximum voltages of 600 kV (HDZP-I) and 2 MV (HDZP-II) to the deuterium fiber loads; this would bring current roughly linearly in time to peaks of 200-250 kA at 125 nsec (HDZP-I) and 800 kA (to date; design maximum 1.2 MA) at 100 nsec (HDZP-II). Frozen deuterium fiber loads were typically 30 μm in diameter by 5 cm long. Diagnostics included X-ray pinhole photography and filtered PIN diodes, neutron counting with various techniques and time history, electrical diagnostics, and highly time-resolved (better than 0.2 nsec) optical imaging (shadowgrams and interferograms; see Appendix B).

The computations reported here represent an extension of Lindemuth's MHRDR (Magneto-Hydro-Radiative-Dynamics-Research) code [38]. MHRDR uses a time- and space-centered alternating-direction-implicit (ADI) numerical method which avoids "splitting" of the equations: all quantities are solved in vector equations, which include representation of all terms in the equations at every step of the solution procedure. Newton-Raphson-like iteration[74] is employed to deal with nonlinear quantities, i.e., nonlinear terms are approximated by the first two terms in a Taylor series, then the resulting linear implicit problem (solution of a block tri-diagonal matrix) is iterated to convergence. The model applied to the dense Z-pinch problem in this chapter is basic (negligible r_{Li}) MHD, the two-dimensional (r,z) equations of magnetohydrodynamics including thermal conduction, radiative energy loss, and resistive diffusion (as developed in

Chapter 2: equations 2.2.1, 2.2.17, 2.2.24, and 2.2.13, dropping the "Hall MHD" terms noted in section 2.3, and with the additional details noted in section 2.4):

$$\frac{\partial \rho}{\partial t} + \nabla \cdot (\rho \vec{v}) = 0 \tag{3.1.1}$$

$$\frac{\partial (\rho \vec{v})}{\partial t} + \nabla \cdot (\rho \vec{v} \vec{v}) + \nabla p - \vec{J} \times \vec{B} = 0 \tag{3.1.2}$$

$$\frac{\partial (\rho \epsilon)}{\partial t} + \nabla \cdot (\rho \vec{v} \epsilon) + p \nabla \cdot \vec{v} - \nabla \cdot (\kappa_{\perp} \nabla T) - \eta \vec{J}^2 + Q_{rad} = 0 \tag{3.1.3}$$

$$\frac{\partial \vec{B}}{\partial t} + \nabla \times (-\vec{v} \times \vec{B} + \frac{\eta}{\mu_0} \nabla \times \vec{B}) = 0 \tag{3.1.4}$$

where ρ is mass density, $\vec{v}$ is velocity, $\vec{B}$ is magnetic field, $\vec{J} (= \nabla \times \vec{B}/\mu_0)$ is electrical current density, ϵ is specific internal energy, p is pressure, T is temperature, Q_{rad} is the radiative energy loss, η is the electrical resistivity, and $\kappa_{\perp}$ is the (perpendicular) thermal conductivity. When a two-temperature model is used, the single energy equation above is replaced by ion and electron energy equations (from 2.2.21 and 2.2.22, again as modified in sections 2.3 and 2.4):

$$\frac{\partial (\rho \epsilon_e)}{\partial t} + \nabla \cdot (\rho \vec{v} \epsilon_e) + p_e \nabla \cdot \vec{v} - \nabla \cdot (\kappa_{\perp e} \nabla T_e) - \eta \vec{J}^2 + \tag{3.1.5}$$

$$+ Q_{rad} + Q_{ei} = 0$$

$$\frac{\partial (\rho \epsilon_i)}{\partial t} + \nabla \cdot (\rho \vec{v} \epsilon_i) + p_i \nabla \cdot \vec{v} - \nabla \cdot (\kappa_{\perp i} \nabla T_i) - Q_{ei} = 0 \tag{3.1.6}$$

where ϵ_α, p_α, T_α, and $\kappa_{\perp \alpha}$ refer to the appropriate ion or electron quantities, and Q_{ei} is the electron-ion energy equilibration term.

The basic alternating-direction-implicit solution algorithm is as follows[38] (portions of Reference 38, which describes this in much greater detail, are reproduced in Appendix D). The component forms of the equations to be solved (such as shown in Appendix D) contain terms which are exactly spatially integrable in one direction (i.e., in "conservative" form), representing fluxes of mass, momentum, etc., and terms which are not so integrable, which Lindemuth refers to as "forces." Spatial integration of these terms is done at a given finite-difference cell; one then has expressions for the fluxes, at the interfaces between cells, and approximates the "force" terms, by taking the average of such terms at the two interfaces of a cell. Each flux and force term at a given cell interface is then written in finite-difference form, i.e., in terms of the cell and neighboring cell values of the quantities to be solved. The key to the alternating-direction-implicit algorithm is that the finite-difference equations which result at this point, are the sum of terms depending on quantity values and their spatial derivatives in one direction, and terms depending on quantities and derivatives in the other direction. This is because none of the equations to be solved contains mixed spatial derivatives (the presence of mixed derivatives in the Hall term thus presented a major problem, the solution of which is described in Chapter 4).

One can then treat the terms dependent on quantities and derivatives in one direction implicitly (on this step leaving the other direction terms explicit), and the resulting matrix to be solved (after linearization) is not the huge matrix which a full two-dimensional implicit solution would require, but only a much more tractable block tri-diagonal one-dimensional implicit matrix, because the unknown quantities are only along a single line in the implicit direction. On the next step, the alternate direction is treated implicitly. In MHRDR, which is

"time-centered" (in a Douglas-Gunn sense[75]), the first step includes implicit and explicit flux and force terms in one direction, plus explicit terms (which have just been solved for in the previously completed full step, incorporating implicit and explicit contributions) in the other direction; the second step includes implicit and explicit terms in the second direction, plus the just-computed implicit terms and explicit terms in the first direction. Both steps include a representation of all terms in the equations (in both directions) at once. Hence, each step results in solution values which are entirely consistent with the complete set of partial differential equations, in contrast to the results of "operator splitting," where each intermediate value is actually inconsistent. In MHD, where physical processes "compete," the MHRDR method should in principle allow the use of larger timesteps than splitting methods.

The program proceeds using essentially a Newton-Raphson iterative linearization method[74]. At each cell interface on a given line, the implicit fluxes and forces are approximated by calculating the explicit fluxes and forces and the explicit derivatives of those fluxes and forces with respect to the quantities to be solved (e.g., $\vec{B}$, ρ, etc.). These numbers become elements in the block tridiagonal matrix to be solved for the implicit quantities. When all the elements have been calculated for a given line, the implicit matrix is solved by forward-backward substitution[76]. If the solution values have not converged to a preset degree (for each quantity, typically 10^{-5} times its largest value), they are used as explicit values with which to compose a new matrix, the solution of which is iterated until convergence for that line is reached (up to a limited number of iterations; if convergence is still not reached, the timestep will be cut). When all the lines in one direction have been solved in this way, the implicit and explicit

flux values are stored (because they will be used in the second step), and the implicit solve procedure is repeated for all the lines in the second direction. The solution values of this second step are the final values for the solved quantities at the new time.

By careful differencing of the equations, the code has uncommon conservation properties[77]. The spatial differencing (in the limit $\Delta t \rightarrow 0$) not only conserves mass, momentum, energy, and magnetic flux, but also maintains "subconservation" properties, that partial sums of component energies (thermal, kinetic, magnetic), such as the sum of kinetic and magnetic energies, are conserved where appropriate (i.e., each pair of corresponding terms individually maintains energy conservation). In general, the time- and space-centered algorithm is second order accurate in Δt and Δx.

MHRDR employs an "artificial viscosity" in the vicinity of strong shocks (large velocity gradients) in order to more accurately depict the physics in such areas (give the correct increase in entropy when a shock traverses the plasma, irreversibly converting ion kinetic energy to ion thermal energy). Lindemuth[77–79] strongly argues that "artificial" is a misnomer here, because the numerical results will be farther from physically correct without it. The functional form of the artificial viscosity is such that it is very localized to the large velocity gradient regions. Intrinsic to the use of such artificial viscosity is a shock heating term, included in the energy equation (ion energy equation in a two-temperature model, because of the mass dependence of viscous effects) for consistency.

For certain types of linear equations[80], the time- and space-centered alternating-direction-implicit algorithm employed in MHRDR is unconditionally numerically stable, i.e. there is no limit on the size of the timestep allowable.

For the nonlinear equations which are being solved here, this is probably not true; one is hard put in advance to know what timestep will be desirable to resolve important details of a given problem, even if such a timestep is numerically stable. MHRDR uses an adaptive timestep: a starting timestep and minimum/maximum allowable timesteps are set, then, as the simulation proceeds, the timestep goes up or down, depending on a number of conditions. If quantities are not changing much, the timestep will go up until the largest change in any quantity reaches a preset value, often a percentage such as 30% of the given quantity; timesteps will be cut if changes exceed this value, if non-physical results such as negative temperatures or densities are encountered, or if the iterations are not converging. In this way, it is possible to relatively efficiently follow a problem, such as the fiber-initiated Z-pinch, with timesteps which resolve interesting physical phenomena as they develop.

The magnetohydrodynamic model used requires for completeness the specific internal energy, the pressure, the thermal conductivity, the average ionization level, the radiative energy loss, and the electrical resistivity as functions of the density and temperature. To obtain the equation of state (specific energy and pressure), the ionization level, the radiative energy loss, and the resistivity, the Los Alamos SESAME[39] tabulated atomic data base computer library is used. SESAME Planckian opacity is employed for the radiative energy loss term, appropriate for on optically thin condition ($\omega_{rad} > \omega_{pe}$), which fiber pinches such as HDZP-I and -II can be shown to maintain for temperatures and densities typical of such discharges. Thermal conductivity follows the (arbitrary $\omega_c\tau$) Braginskii formalism[63], as does electron-ion energy equilibration. Hence the thermal

conductivities are:

$$\kappa_{\perp e} = \frac{n_e T_e \tau_{ee}}{m_e} \frac{4.66\,\omega_{ce}^2 \tau_{ee}^2 + 11.92}{(\omega_{ce}^4 \tau_{ee}^4 + 14.79\,\omega_{ce}^2 \tau_{ee}^2 + 3.77)}; \tag{3.1.7}$$

$$\kappa_{\perp i} = \frac{n_i T_i \tau_{ii}}{m_i} \frac{2\,\omega_{ci}^2 \tau_{ii}^2 + 2.64}{(\omega_{ci}^4 \tau_{ii}^4 + 2.7\,\omega_{ci}^2 \tau_{ii}^2 + 0.68)}. \tag{3.1.8}$$

Single-temperature $\kappa_\perp$ is the sum of these. The electron-ion energy equilibration term[64] is

$$Q_{ei} = \frac{3 m_e n_e}{m_i \tau_{ee}} (T_e - T_i) \tag{3.1.9}.$$

Actual experimental current vs. time values provide the boundary condition for magnetic field at the outer radial wall: Ampere's Law prescribes $B_\theta(r_{wall}) = \mu_0 I/(2\pi r_{wall})$. The code employs a method by which field and plasma can realistically pinch inward from a radial wall, if equations and boundary conditions so dictate, and later expand back to the wall in a consistent fashion[81] (at early stages of the simulation, field very rapidly diffuses across the low-density "vacuum" region to the current-carrying surface of the fiber). Mass is allowed to leave through the outer radial wall, if it is moving in that direction; this prevents an unrealistic build-up or "bounce-back" of mass at the outer radius, which is intended to simulate the surrounding vacuum. When it was found that significant current and plasma density needed to be resolved in the vicinity of the outer radius, a means was found to expand the grid to treat this appropriately; this is described below. The axial boundary conditions are usually taken to be electrically conducting and heat insulating, giving "mirror" conditions at these boundaries for field and energy; axial walls are intended to be solid, as are the real electrodes, hence $\vec{v}_{normal} = 0$. Haines has done some theoretical work

predicting that end losses of energy from such a pinch will not be significant over the typical O(100 nsec) discharge time[70], and a single simulation run with zero-temperature axial boundaries agreed with this result.

"Cold-start" initial conditions are a solid, cryogenic deuterium fiber (density 88 kg/m^3, which is half that of solid deuterium, to account for observed voids and other non-uniformities in the fiber; temperature 0.001 eV; radius 15 μm; 2% random density fluctuations provide perturbations for instability growth) surrounded to about twice the fiber radius by a low density, "warm" halo plasma (e.g., density 0.088 kg/m^3, with no perturbations; temperature 1 eV), which provides an initial current conduction path. Computed results are insensitive to the details of this halo plasma after a short-lived (<10 nsec) transient, because of the small mass involved relative to the fiber-generated plasma. The surrounding vacuum is simulated by a cold, very low density region (e.g., density 10^{-7} kg/m^3, temperature 0.025 eV) of total mass less than 1% of the fiber, extending out to a zero-temperature, electrically insulating wall. To avoid unrealistic ohmic heating of the highly resistive "vacuum region", a "cutoff density" is used, below which ohmic heating is turned off. Because the bulk of the plasma in such discharges may go from high, near-solid densities to expanded, much lower densities, this author implemented a variable cutoff density, which adjusts itself, within programmed limits, so that (typically) 99% of the plasma (presumably the bulk of the fiber-generated plasma) remains above cutoff at all times. The results from runs with both fixed cutoff densities, and these adaptively varying cutoff densities, showed no significant differences (typical cutoff densities are from 10^{18} to 10^{16} cm^{-3}).

The early fiber-ablation stage of the discharge necessitates relatively fine ra-

dial grid spacing, but this stage can be followed by an explosive expansion of the heated plasma. Because of this, Lindemuth's initial two-dimensional simulations could only be run to about half the HDZP-I current peak before "running out of grid": significant current and plasma density needed to be resolved outside the original, maximum affordable radial grid. To overcome this problem, this author explored the use of an existing capability in the code, allowing pre-programmed radial grid expansion. This was found to be impractical, because one doesn't know in advance when and how fast the grid should be expanded. It was necessary to implement an adaptive system, capable of expanding or contracting the grid (within programmed limits) to follow an expanding or contracting plasma. The radial grid is checked at each timestep, and adjusted so that the outer boundary is always at least 150% of the radius within which 95% of the total axial current is contained. Provision for this grid motion is written into the "generalized Eulerian" (moving-orthogonal-grid) difference equations, avoiding the complications of the Lagrangian approach: i.e., finite-difference equations are written and solved for quantities, such as velocity, relative to a known (pre-programmed, or now, adaptively set) grid velocity.

To allow direct comparison of simulation results with experimental data, this author wrote an addition to the code's graphical post-processor to generate shadowgrams and interferograms, as collected on the experiments, from simulation results (this is done by tracing a grid of rays through the simulated plasma; see Appendix B). A dynamically developing instability may be overlooked in a plasma imaging diagnostic which lacks temporal resolution (visual and X-ray images require rather long exposure times relative to the nanosecond-scale dynamics of such pinches). It has been possible to produce very highly time-

resolved (better than 0.2 nsec) experimental shadowgrams and interferograms. Hence these present experimental data of primary interest for comparison with the simulations.

In the simulations reported here, radial grids of 80 to 100 points, more finely spaced near the axis (zones smaller than 2 μ) to better resolve the fiber/plasma column, cover a radius as small as 1 millimeter, but ultimately as large as several centimeters, if rapid expansion is followed. It would be desirable to cover the full 5 centimeter axial length of the experimental chamber with many hundreds of grid points, to resolve the smallest and largest instability scales possible, but this is prohibitively expensive at present. It has been possible to cover axial sections as large as 2 centimeters, and as small as 0.25 millimeters, with uniformly spaced axial grids of 31 (sometimes 62) points. These are respectively capable of resolving the largest (X-ray "beads") and smallest (shadowgram "spicules"– fine spikes radiating outward from the main axial column at early times in the discharge) features observed in any of the experiments. Although the smallest, most finely resolved grids do show fine-scale instability growth starting earlier than the larger grids, these fine-scale instabilities are not ultimately the most unstable or fastest expanding disturbances, because as heating and expansion take place, shorter wavelengths saturate, and larger-scale instabilities tend to dominate the system. Mid-size grids, covering about 2 millimeters axially, show the most rapid instability growth and expansion; larger grids show a delay before the larger modes they can resolve begin to develop. Hence the timing of instability development and expansion may vary by as much as 20 nsec (in 100-nsec current-peak discharges) for different grid sizes. This is comparable to experimental timing uncertainties (e.g., the relation between driving voltage, current,

and diagnostic images in time).

With these improvements implemented, it has been possible to run simulations to about 120 nsec for HDZP-I, near its 200-250 kA current peak, and to 44 nsec (about 300 kA) for HDZP-II (also as high as 430 kA for an as yet not experimentally realized 1.2 MA-peak shot on HDZP-II). At these points, not only is it numerically difficult and expensive to deal with the very rapidly expanding and highly irregularly developing plasma, but large parts of the plasma have reached temperatures and densities where the validity of the fluid model is very much in doubt; this will be discussed further below. Extending the simulation beyond these points, then, is as much a matter of finding an appropriate physical model, as it is a matter of numerical technique.

A potentially important limitation of these computations is geometric: quantities vary only as functions of r and z, and only the azimuthal magnetic field and velocity components perpendicular to the field (v_r,v_z) are computed, along with scalar mass density and internal energy. Within the fluid model, the finite-Larmor-radius ordered terms in the magnetic field equation (Hall term and diamagnetic pressure), the viscous stress tensor, and accompanying terms in the energy equation, are ignored as well. Up to the point where the fluid description and classical transport break down, comparison of the results of such a simulation with experiment can suggest whether or not any of the aspects left out, geometric or otherwise, were essential to the behavior of the system.

3.2 Results of Basic MHD Model[82-84]

An account of the low-current experiment HDZP-I described plasma columns "free from visible instabilities for typically 80 nsec into the current discharge, at which time the [m=0] instability growth times would be expected

to be $\approx$1 nsec...m=1 modes are not observed."[3] Fastest growth times for ideal m=0 (and m=1) instabilities[18] are on the order of the Alfven time $\tau_A = a/v_A$, where a is a scale length of the plasma, and v_A is the Alfven speed. Typical Alfven speeds and scale lengths of these plasmas (discussed in section 2.5) do indeed correspond to Alfven times on the order of 1 nsec, if not smaller. Plasma columns also appeared to be relatively compact (radius $\leq 200\mu$m), based on shadowgram images (Figs. 1a, 2a; note that these are electronically collected images of finer resolution than the original photographic shadowgrams on which the above comments were based; see Appendix B), which were employed to provide well time-resolved images without the complex temperature dependence of passive radiation emission. A similar experiment[2] at the Naval Research Laboratory (about which more will be said later) also appeared to exhibit such compactness and relative stability, on the basis of visible and X-ray emission imaging of the plasma.

The two-dimensional (2-d) basic MHD simulations of HDZP-I discharges show significant expansion and m=0 instability development (Figs. 1c, 1d) before the fiber has become fully ionized, which occurs in the simulations at 30 to 50 nsec. Model shadowgrams generated from simulation of HDZP-I reasonably agree, in size and instability wavelength, with those from experiment (Figs. 1a, 1b). The width of the shadowgrams tends to remain smaller than the effective diameter of the plasma column, in terms of mass (Fig. 1c) or current (Fig. 1d). This is true because light ray deflection (which creates the shadow) depends on density gradients, and is greatest near the central core of the plasma column (particularly while this is still being fed from the ablating fiber), where these density gradients are the largest. The lower density, more gently varying outer

regions of the plasma column do not provide enough ray deflection to cause obvious shadows, even though a significant fraction of the mass or current may reside there. Significant instability development in these outer regions (Figs. 1c, 1d) only shows up as slight variations in the shadowgrams (Fig. 1b). After the fiber is completely ionized, the simulation-generated shadowgrams expand and become more irregular, even disappearing at some points along the axis, again in agreement with experimental results (Figs. 2a, 2b, also 1a, right-hand image, 3a, 3b). This may be interpreted as evidence of full development of the instability, to the extent that line density (total number of particles per unit axial length, Fig. 5c) along the axis becomes very irregular (i.e., plasma column separates into distinct "blobs", ultimately reflected in formation of "beads" in X-ray images[2,14]).

Simulations and observations of the Los Alamos high-current experiment HDZP-II [4,14] resemble the higher-current, later phases of HDZP-I discharges. In the simulation of HDZP-II, the higher current fully ionizes the ($15\mu m$ radius) fiber in 10 to 20 nsec (where 0.75 to 1.2 MA current peaks would occur at 100 nsec, although HDZP-II simulations were not run all the way to current peak). Instabilities develop rapidly, and drive intense nonuniform heating and rapid column expansion to radii on the order of centimeters, within 50 nsec. Only very early in the experiment is there enough density gradient to give a useful shadowgram at all (Fig. 3a), and this wide and irregular image resembles the late shadowgrams of the low-current experiment HDZP-I (Fig. 2a). The computed shadowgram (Fig. 3b) has many features (width and instability wavelength) of the observed one (Fig. 3a).

Because late time shadowgrams were impossible to obtain on HDZP-II, in-

terferometric imaging techniques (see Appendix B) were then employed. Interferograms give images integrated directly off plasma density rather than density gradient (as in shadowgrams). These images, both experimental[14] and simulated, show characteristic "island" patterns of large amplitude m=0 modes (Figs. 4a, 4b); again, a repeat of what is seen in late low-current simulations (Figs. 4c, 4d, 4e). The line density along the axis, derived from the simulations, is in good agreement with the results from experimental interferograms (Figs. 5a, 5b, 5c). Experimental variation in fiber size, and the use in simulations of starting fiber density one-half that of pure solid deuterium (to compensate for possible voids in the experimental fiber), account for the minor differences between computed and measured line density.

Theoretical and computational investigation into the reported "anomalous stability" of the early, low-current experiments has concentrated on the connection between driving current ramp times and plasma profiles[24,85,86], and the stability of such profiles as modified by non-ideal effects such as resistivity[19-30]. In particular, it has been found that low-temperature plasma columns which are relatively resistive, with Lundquist number ($\tau_{resistive\ diffusion}/\tau_{Alfven\ transit}$) up to about 100, may be m=0 stable[21,23,24,30]. The plasmas for which these results have been derived are constant-radius, uniform (Bennett[87]) temperature, and of near-solid density (i.e., fully ionized, and expanded to no more than a few hundred μm). In contrast, what is seen in early (pre-complete ionization) stages of these one- and two-dimensional simulations (e.g., Fig. 1 of Ref. 35) is a low-density (e.g., $10^{-3}\times$solid) coronal plasma with a temperature peak at the edge that may be considerably higher than the Bennett temperature. Such profiles resemble those discussed by Bobrova, et al, for exploding copper wire

and deuterium fiber Z-pinches[88]. Low density and high temperature are factors which would raise the effective Lundquist number of such a plasma from "safe" Lundquist numbers of order 1, beyond the critical values around 100, even during the low current, early stages of the discharge. Once instabilities begin to grow in the corona, expansion of the column is enhanced, leading to still lower densities, larger radii, and still higher Lundquist numbers.

The presence of the cold core does seem to inhibit full nonlinear instability development, such as displayed in Figs. 4d and 4e (note the drop in density in the m=0 "neck" region, in contrast to the earlier density contours, Fig. 1c), which appears connected with the explosive expansion of higher-current discharges on HDZP-II. The simulations show re-connection of the outer regions of such m=0 lobes, and current jumping across them at progressively increasing scale lengths; this may not only directly contribute to the physical expansion of the column, but may lead to instability heating[89], which further drives expansion (note in this regard the two-temperature simulation results discussed below).

The high temperatures and low densities, which may be seen in the fully developed instability/expansion stage of the discharges, are likely to drive the plasma out of the one-temperature regime (ions and electrons in energy equilibrium), as noted in Appendix A. Lindemuth's code has an existing two-temperature capability, but it was found impossible to run the fiber Z-pinch problem in the two-temperature mode, due to problems either with the very low temperature sections of the two-temperature SESAME equation-of-state tables, or with the energy equilibration section of the code; these problems have not yet been resolved. However, it was possible to do two-temperature runs using an ideal gas equation of state in place of the SESAME tables (still using SESAME resistiv-

ity, ionization state, and radiation); confidence in this procedure was bolstered by the fact that one-temperature ideal gas runs showed little overall difference from all-SESAME one-temperature runs. The ion and electron energy equations differ, in addition to the use of appropriate ion or electron pressures and thermal conductivities, in that the electron equation has the ohmic heating and radiative cooling terms, while the ion equation has an "artificial viscosity" shock heating term (both have complementary equilibration terms).

The general instability/expansion behavior was still seen in these two-temperature runs, but an interesting detail emerged in the heating pattern (see Fig. 6). In 1-d and early stages of 2-d runs, ohmic heating of electrons was the primary heating source, and electron temperature thus either led or remained in equilibrium with ion temperature. However, when instability development led to extreme and irregular density and velocity gradients (such as in Figs. 4d and 4e), shock heating of ions caused the ion temperatures to exceed those of the electrons, by as much as 50 eV for average temperatures (Fig. 6a), and hundreds of eV for peak temperatures (Fig. 6b). This fits the pattern of instability heating suggested by R. Lovberg[89], which is under experimental investigation by Lovberg and R. Riley Jr.

Chittenden and Haines in a recent paper have stated that the thermoelectric Nernst and Ettinghausen effects "cannot be ignored when electron and ion temperatures are sufficiently decoupled."[59] In 1-d Lagrangian two-temperature simulations using Braginskii perpendicular resistivity, they see such decoupling in the very low density outer edge of the coronal plasma; this region carries a lot of current, and hence has large ohmic heating of the electrons, but they do not equilibrate with the ions. The ions could normally conduct much of

the heat away, because the ion cross-field thermal conductivity (3.1.8) is larger than that of the electrons (3.1.7) by the factor $(m_i/m_e)^{\frac{1}{2}}$. In this case, the low electron-ion thermalization rate (3.1.9, proportional to $n_e^2/T_e^{\frac{3}{2}}$), leads to a runaway electron temperature situation at the plasma edge; higher temperature (lower resistivity and thermalization) leads to higher currents, more heating, etc. However, if the Nernst and Ettinghausen effects (which cause a radial flow of heat and current density) are included, the ion and electron temperatures stay much closer together, resulting in a much more uniform current distribution. Chittenden has also found a similar effect, causing current to be more uniformly distributed across the pinch radius, due to anomalous (micro-turbulence generated) resistivity[90].

In the two-temperature runs done here, one does not see a significant decoupling of the electron and ion temperatures at the edge, as seen in the Chittenden/Haines paper, for several reasons. There is a cutoff density in MHRDR, below which ohmic heating is not included, in order to avoid unrealistic heating (and runaway processes such as described above) in the low-density "vacuum" plasma regions. Although the use of such a cutoff does introduce a somewhat arbitrary, physically inconsistent element into the model, the intent is to use it only in "vacuum" areas which do not meet the criteria for the fluid model, and which do not have a decisive effect on the bulk plasma dynamics. Cutoff density values have been varied over two orders of magnitude without seeing any significant differences in the simulation results. Also, the resistivity used here is from the SESAME tables, rather than Braginskii. The semi-empirical SESAME resistivity tables give values for a wider range of temperatures and densities than the Braginskii fully-ionized plasma model; in particular, for conditions where

neutrals are dominant, and for conditions of such low density that almost no current-carriers are available. Hence it may be that SESAME resistivity, in the low-density coronal edge regions where the above discussed phenomena take place, is greater than Braginskii resistivity, and so tends to exclude current from such regions.

In a one-temperature model, as noted above, ohmic heating at the edge can be balanced by (predominantly ion) heat conduction away from the edge. Hence not including the Nernst and Ettinghausen effects in the one- and two-temperature simulations presented here did not lead to the runaway edge current and heating problem brought up by Chittenden and Haines. There are other situations in which ion and electron temperatures may decouple, such as the instability ion heating discussed above. Shock-heated ions, in areas of low density and high temperature, would also have a low electron-ion thermalization rate. The possibility of Nernst and Ettinghausen effects playing an important role in such situations makes addition of these effects desirable.

A major difference between the Los Alamos experiments and the deuterium-fiber-initiated experiments at the Naval Research Laboratory (NRL)[2,13] is the thickness of the fiber: NRL used 40- to 60-μm-radius fibers, as opposed to 15-μm at Los Alamos. Current rise rates have also varied among the two Laboratorys' experiments, from about 1 to 10 kA/nsec. A striking observation of the early NRL experiments[2] (current peaks up to 640 kA at 125 nsec) is that significant expansion of the originally very compact visible emission image (taken to indicate onset of gross instability) does not occur until current peak (dI/dt=0). Thus the pinch would appear to remain stable "as long as the current is rising."[2]

The NRL experiments have not been as comprehensively modeled as the

Los Alamos ones, but 2-d simulations have been carried out for 60-μm-radius fiber, 640 kA at 125 nsec NRL discharges; a simulation was also done of a planned 40-μm-radius fiber on Los Alamos' HDZP-II with current peak 750 kA at 100 nsec. In these simulations, the fibers did survive considerably longer (40-50 nsec for the 40-μm fiber, as opposed to 10-20 nsec in the analogous, HDZP-II 15-μm fiber run; survival was longer than 60 nsec for the 60-μm fiber). Onset of drastic instability development and expansion did not occur until the 40-μm fiber was gone (around 55 nsec, as opposed to 30 nsec for the 15-μm run). The 60-μm simulation could not be run beyond 60 nsec (260 kA), because portions of the coronal plasma had reached the highly irregularly developed, high temperature, low density (fluid model invalid) conditions which have ultimately defeated the numerical algorithm used in all these simulations. At this point in the 60-μm simulation, a cold ($\leq$1 eV) core remained, surrounded by a medium-hot ($\sim$100 eV) corona of about 10^{-1} times solid density out to about 100 μm (which could be responsible for the visible radiation image of about this radius at this time), surrounded by a hot (into keV range), several orders of magnitude lower density, strongly unstably developing outer corona. This resembles the pre-complete-ionization coronal plasma seen at earlier times in the 15-μm-fiber HDZP-I and -II runs. In two-dimensional simulations, the expansion and severe instability development, which occur shortly after complete fiber ionization and are reflected in shadowgram and interferometric imaging, would also be reflected in a sudden expansion in the visible emission images[36]. Hence if ionization of the fiber is completed prior to current peak, one would expect the above "dI/dt=0 hypothesis"[2] to be violated, and visible expansion to occur while the current is still rising. Such instabilities and expansion while the current is rising

were reported for the later, higher current NRL experiments[13]. These later experiments did employ a current ramp (920 kA peak at 840 nsec) much slower than that of the original NRL experiments, which were considered to use an optimum current rise value (~4 kA/nsec). The 2-d simulations of the original NRL experiments are consistent with the fibers becoming completely ionized very near the time of current peak, making it difficult to distinguish between whether the visible expansion at this time is due to dI/dt=0, or due to completed fiber ionization. It would be desirable to run a series of experiments on a single well-diagnosed machine, accompanied by a series of simulations, in which fiber thickness and current ramp rates were varied, so that one could clarify the effects of each. Because at this point in time, operations have ceased on the Los Alamos and NRL machines, it is hoped that such work may be done on the Imperial College high-current fiber-pinch machine[54].

Comparison of simulation and experimental results on HDZP-I and -II leads to the following interpretation. The "anomalous stability" reported for the thin-fiber HDZP-I experiments may have been a misinterpretation based upon limited diagnostics; "stability" in any event is limited to the earlier, lower-current stages of the discharge. Even at early times, there appears to be instability development in the outer corona which is only faintly reflected in shadowgram images. Full nonlinear instability development does appear to be held back, as long as some portion of the heat-sinking fiber persists. Because of the higher currents encountered earlier in HDZP-II discharges, the fiber becomes completely ionized earlier, allowing drastic instability development to drive rapid expansion at a very early point. It appears thicker fibers, such as those used in the NRL experiments, could delay the early onset of gross instability and expansion (although

the simulations still show an unstable coronal plasma). However, this would almost certainly reduce the temperature and may prevent conditions for significant neutron production from being reached; this is a question to be settled by further experiment and computation.

Once a computational tool shows the capability to give results in agreement with existing experiments (and in the next chapter, an effort is made to include terms which might enhance this agreement), one can with caution begin to use it to predict the outcome of new experiments. A natural area to explore for fiber-initiated discharges is the effect of the driving current ramp. Both theoretical and experimental investigations have related the current ramp to the resulting plasma profiles, and the connected issue of stability[19-30,85,86]. One example is the Haines-Hammel curve[9,11,12], which will theoretically maintain a constant radius plasma column while raising the current up to the Pease-Braginskii limit, where ohmic heating is just balanced by radiative cooling. Of course, the actual experiments, and the simulations done here, start with a cold fiber, not a plasma with the fiber's dimensions. One-dimensional simulations using such a current ramp did show roughly constant radius behavior; however, in 2-d, the characteristic explosive instability/expansion set in strongly by the time the current reached 500 kA. Extremely fast rising current ramps (as much as 30 kA/nsec) gave similar results. Ramps as slow as 1 kA/nsec have been tried; they also show instability and expansion. This code was also used to do a simulation of a "flat-top" current ramp discharge, in which current goes to 160 kA in about 20 nsec (at which point no instability or unusual expansion is evident), then is held at that value. The same explosive instability/expansion as seen in the rising current case, still occurred within 20 nsec of the time current was flat-topped; the

plasma did then settle into a low-density (expanded out to centimeters radius), less unstable configuration. There is some interest in using a slow-ramped or flat-top current rise fiber-inititated Z-pinch as a means of providing an initial fill plasma for a heavy liner "magnetized target fusion" implosion[91,92]. In this case, the expansion of the plasma is not critical, because the intent is to re-compress it to fusion conditions, by imploding a surrounding liner.

The pattern which is seen repeatedly in these fiber-initiated pinch simulations is formation of a low-density (orders of magnitude below solid) coronal plasma, which carries most of the current; consequently, it heats rapidly into the hundreds of eV range. Such a plasma has a relatively high Lundquist number, well beyond the levels for which resistive stabilization has been theoretically or computationally predicted. Accordingly, it acts like a classical ideal MHD Z-pinch: it is an unstable plasma, and when there is no longer a low-temperature core to provide some restraint to instability development, violent instability and expansion result. These simulations have been run far into the nonlinear stages of instability development (see Figs. 4d and 4e), although plasma conditions tend to occur at this stage which make doubtful the validity of the fluid model. The only nonlinear "stabilization" mechanism seen is re-connection of the outer plasma lobes; this produces an expanded, lower density plasma, which is not what one looks for in an ostensibly self-confining, self-heating fusion device.

It has been noted by Kies[93] and others that the plasma initiation stage of an initially non-conducting fiber-into-plasma discharge may be crucial to its subsequent development. As discussed above, instabilities first develop in the low-density, early coronal plasma; higher density may be stabilizing here (lower Lundquist number). Some pre-ionization of the fiber, by a voltage pre-pulse or

radiation flash, may be desirable to set up current/density profiles which may lead to a stable or relatively stable high density Z-pinch. To this end, simulation parameters of the initial conduction (coronal) plasma were varied, without much effect. Although the details of current initiation at the beginning of such a discharge are unknown, it would seem that providing an initial conducting corona, of negligible mass compared even to the quickly appearing ablation-generated corona, should not have a crucial effect. 2-d simulations attempting to model flash-ionized fibers have been done, including a 2 eV, half-solid-density pinch which immediately starts at 200 kA current, to prevent sudden expansion; it too ultimately showed explosive instability and expansion. Investigation of experimental variations, such as plasma initiation techniques, is continuing. Some hope for obtaining the desired micron-scale, high-density plasma current channel has recently been generated by experiments utilizing the "plasma-on-wire" (POW) technique[94], which will be examined in Chapter 5.

As temperatures rise and density drops, particularly in and around the narrow m=0 "necks" which develop in the simulations, the appropriateness of the fluid model breaks down. Thus late development of instabilities may well be controlled by effects absent from the model. An improvement in the fluid model would come from the inclusion of terms usually ordered out on the basis of small Larmor radius (which may indeed not be small in the case of the Z-pinch[19,41], as noted in Chapter 2 and Appendix A): the Hall and diamagnetic pressure terms in the Ohm's Law (magnetic field evolution) equation, and accompanying terms in the energy equation.

Analytic and numerical work on the influence of the Hall term gives equilibri-

um-dependent results (lower m=0 growth rates for some equilibria, higher for others)[19], so the present simulation work's close-to-the-experiment approach is important, to insure that realistic equilibria are evaluated. That the Hall term may have drastic effects on the important scales of an instability is graphically illustrated in a recent paper by Huba, Lyon, and Hassam[66]. The implementation of Hall and associated terms in the 2-d code used here, which required a major adaptation of the alternating-direction-implicit algorithm, is described in the next chapter.

CHAPTER 4: HALL MHD SIMULATIONS

4.1 "Hall MHD" Computational Modeling Task

The "Hall MHD" model developed in Chapter 2 requires the addition of four similarly ordered terms to the standard MHD equations. These are the Hall and diamagnetic pressure terms (added to the magnetic field evolution equation), and the electron "work" and electron current energy convection terms (added to the energy equation): $\nabla \times (\vec{J} \times \vec{B}/(n_e e))$, $\nabla \times (\nabla p_e/(n_e e))$, $p_e \nabla \cdot (-\vec{J}/(n_e e))$, and $\nabla \cdot (\rho \epsilon_e (-\vec{J}/(n_e e)))$. From a practical point of view, these are four separate numerical modeling tasks; it's hard enough to debug and benchmark a single new term in a large code, without trying to do four terms at once. By doing terms one at a time, one may initially miss compensating effects between two or more terms, which the MHRDR code, with its simultaneous solution of all quantities, is able to exploit. It is the most practical approach, however, to implement one term at a time, deal with the obvious problems which it presents, then go on to the next term, and any inter-relationships which then arise. A look at the algebra in section 2.3, in which it is shown that if the diamagnetic pressure term is included, energy consistency requires that the electron "work" term be included, also reveals that the Hall term by itself only conservatively re-distributes magnetic energy. Hence a natural division of the task is as follows: do the Hall term first, then the diamagnetic pressure term, then the "work" term, and finally the electron current energy convection term. In this chapter, development of the additional terms is reported in that order; then the results of simulations of the dense Z-pinch will be given, including some of the new terms (physically inconsistent, but potentially informative cases), and finally including all of the new terms.

To the extent possible, it will be desirable to follow the existing MHRDR algorithm, which has proven suitable to the demands of the fiber Z-pinch problem. However, all the new terms introduce a significant complication: they involve cross-derivative quantities. For the limited-geometry MHD model solved by MHRDR in Chapter 3, a key feature of the equations, which made the alternating-direction-implicit approach possible, was that the flux of any quantity in a given coordinate direction, depended only on quantities and their spatial derivatives in that direction. Hence the problem very naturally splits into one-dimensional implicit lines to be solved (sequential implicit solves for both directions give the final values for the new time). The curl of the pressure gradient ∇p_e, in the diamagnetic pressure term, and the curl or divergence of the current $\vec{J}$ in the other terms, couple the fluxes of quantities in one direction to the cross-derivatives (the derivatives in a perpendicular direction). Hence, if an implicit approach is to be used, some means must be found to deal with this, hopefully compatible with the existing ADI coding.

The computational physicist, searching for an answer to an interesting physical problem, may take a more pragmatic approach than a numerical analyst or mathematician. The elegance of a solution is of less importance to the physicist than its accuracy, in the broad sense of the term: does the numerical technique used preserve the essential physics of the problem to be modeled? Of course, advanced numerical techniques may be vital to the possibility of solving a physical problem, even with today's impressive computing hardware; the present investigation would have been impossible without the extremely robust implicit algorithm employed. However, even though ordering of terms in the fluid model suggests the possible importance of the Hall and diamagnetic pressure effects,

one could not know in advance that these would be significant relative to other complex processes taking place as the plasma develops (such as the distribution of heat and current density over the ablating fiber and coronal plasma). Nor could one know whether or not the new terms would have an overriding effect on numerical stability (though some 20/20 hindsight will later be displayed on this matter). One might desire the relative freedom from timestep restrictions (of unknown severity) provided by implicit methods. However, implicit methods tend to be programming intensive: the additional coding complexity and computing time required discourage one from starting with this approach. Hence, the logical first step in adding these terms to the present simulation is through explicit additional fluxes of magnetic field.

4.2 Explicit Hall and Diamagnetic Pressure Terms

The Hall and diamagnetic pressure terms, as additions to the left-hand side of the magnetic field evolution ($\nabla\times$(Ohm's Law)) equation 3.1.4, are:

$$\nabla \times (\frac{1}{n_e e}((\frac{\nabla \times \vec{B}}{\mu_0}) \times \vec{B} - \nabla p_e)) \tag{4.2.1}$$

These terms were spatially center-differenced in conservative form using the explicit values of (electron) density, pressure, and magnetic field. "Conservative form" means that the component forms of the equations (such as given in Appendix D) are the sum of all spatial derivative terms, so that after an exact spatial integration, they will represent fluxes across a cell interface. No analytic manipulation is done to the terms before differencing. A center difference for a spatial derivative is a second-order accurate approximation for the derivative:

$$\frac{\partial f}{\partial x} \simeq \frac{(f_{j+1} - f_{j-1})}{2\Delta x} \tag{4.2.2}$$

where the j's are the indices of the grid in the x-direction.

These explicit fluxes of magnetic field (in the appropriate direction) were then added to the time-centered (i.e., half implicit and half explicit) magnetic fluxes in each direction, on each alternating-direction step. "Floor" values of the electron density were implemented (similar to the cutoff density values mentioned in chapter 3, below which ohmic heating is turned off to prevent unrealistic heating of "vacuum" regions), so that very low density "vacuum" regions would not show an unrealistic Hall effect. After constant density runs (which for this geometry will result in complete cancellation of Hall and diamagnetic pressure effects) were done to establish that this differencing would have the expected null effect, the same fiber-initiated Z-pinch problems described in the previous chapter were started.

These would run only a few nanoseconds before fine-scale perturbations in the magnetic field would begin to appear at the edge of the still relatively cool (e.g. 10 eV) coronal plasma (Fig. 7a), long before any instability growth had been noted in the MHD runs. Unfortunately, this was quickly accompanied by a breakdown of the numerics: the adaptive timestep setting routine found that it could not cut the timestep enough (within the pre-set limits of 10^{-9} to 10^{-18} seconds) to keep field at some point from growing uncontrollably (see Fig. 7b).

If the other terms (magnetic convection, diffusion, and diamagnetic pressure) in the field evolution are neglected, and the Hall term (in r,z coordinates) is transferred to the right-hand side, one has the following equation:

$$(4.2.3)\quad \frac{\partial B_\theta}{\partial t} = \frac{1}{e\mu_0}\{-\frac{\partial B_\theta}{\partial r}\frac{B_\theta}{{n_e}^2}\frac{\partial n_e}{\partial z} + \frac{\partial B_\theta}{\partial z}\frac{B_\theta}{{n_e}^2}\frac{\partial n_e}{\partial r} - \frac{{B_\theta}^2}{{n_e}^2}\frac{\partial n_e}{\partial z} + \frac{2B_\theta}{n_e r}\frac{\partial B_\theta}{\partial z}\}$$

Characteristic of the Z-pinch is a large radial density gradient. At points with such large density gradients, the second term in the above equation may

strongly exclude field where the axial gradient of field has one sign, and gain field where the sign is opposite, leading to the perturbation growth seen. However, if enough field is excluded that the sign of the field at that point changes, the sign of the second term also changes, leading to a reversal of the process described. Hence the "hole" in the field should not grow without limit (of course, accompanying changes in field and density gradients can also affect this). It does appear, however, that the explicit algorithm misses this self-limiting effect (see Fig. 7b), and the field "hole" tries to reach large negative values; in essence, this is a numerical instability.

Can this be simply explained? Numerical stability analysis is most easily done for linear equations. For nonlinear equations such as the above, one may start by finding a linearization that preserves important features of the problem, and then analyse the linearized equations (of course, stability of the linear case does not guarantee stability of the nonlinear case, as shall be seen). First, assume that all but the second term of the above equation can be ignored, and there is a large fixed density gradient in r, but no density gradient in the z-direction. Then linearize about a constant field ($B_\theta = B_1(r,z,t) + B_0$):

$$\frac{\partial B_1}{\partial t} = \frac{B_0}{e\mu_0 {n_e}^2}\frac{\partial n_e}{\partial r}\frac{\partial B_1}{\partial z} = v_{convective}\frac{\partial B_1}{\partial z}. \tag{4.2.4}$$

The result is a simple (one-direction) convection equation for B_1 in the z-direction. A constant field is perhaps not a very good model for the Z-pinch; one could try a second linearization, for example, about a field varying only in z with a large constant axial gradient (axial gradients could be expected to appear for a number of reasons, such as if any MHD m=0 mode growth were present,

or due to axial boundary effects). Then where the B_0 field equals 0, one has:

$$\frac{\partial B_1}{\partial t} \simeq \frac{1}{e\mu_0 {n_e}^2} \frac{\partial B_0}{\partial z} \frac{\partial n_e}{\partial r} B_1 = k_{exp} B_1 \tag{4.2.5}$$

where $B_\theta = B_0(z) + B_1(r,z,t)$ with constant $\partial B_0/\partial z$ and $\partial B_0/\partial z \gg \partial B_1/\partial z$: a simple exponential equation.

Both these linear equations bode ill for an explicit algorithm. Numerical stability for the exponential equation is subject to strict timestep limits[95] (which may become insuperable due to the nonlinear dependence of the linearized "constant" k_{exp}), and the simple convection equation can be shown to be unconditionally unstable for a spatially centered (as this code is, although also time-centered for all other terms) explicit algorithm[96] (the reasons for which shall be much further discussed). At this point it is apparent that an implicit treatment of these terms will probably be necessary.

4.3 Adaptation of Implicit (ADI) Algorithm for Hall Term

There are good reasons for trying to stay within the existing alternating-direction-implicit algorithm, when adding new physics to the numerical code used here. First, it is known that this particular code, with the modifications described, can handle the not insignificant demands of this problem; a different approach might have trouble with the strong gradients, for instance, before even running into the additional numerical demands of the new terms. No doubt related to the demonstrated robustness of the present algorithm is an integral feature of its design which, though probably not unique among multi-dimensional MHD codes, is at least uncommon: there is no operator splitting. MHRDR solves for the complete vector of time-advanced quantities (e.g., density, magnetic field, velocities v_r and v_z, and internal energies) simultaneously, always including all

terms of a given equation (e.g. magnetic convection and diffusion). Although only one direction is handled implicitly on each half-step, every (half-step) set of difference equations solved is a complete representation of the differential equations, including the effects of implicit and explicit fluxes in the implicit direction, and the previous half-step's implicit and explicit fluxes in the other (presently non-implicit) direction. Thus, a very natural simultaneous treatment of all physical effects is maintained, while any unnatural effect of the directional splitting (which makes the implicit solve task a relatively tractable one-dimensional one) is minimized. To separately solve in some other manner for the Hall and diamagnetic pressure effects, and then add them in, would violate this scheme, and potentially lose its demonstrated robust nature.

The fiber-initiated Z-pinch, and the effect of the Hall term on it, are problems on which there is no definitive theoretical, and only limited experimental, knowledge of the outcome. In attempting to model complicated physical systems such as this, it is extremely desirable to find one or more test problems with clear-cut results dependent on the newly added physics, to serve as "benchmarks" of the code. If the computational tool gives correct physical results in such known cases, one gains confidence in its application when the results are unknown. The Hall term is difficult in this regard, in that it is an intrinsically two dimensional effect; one cannot first do a simpler one-dimensional case, and then deal with the more complex two dimensions. Fortunately, computational and analytic research on Hall-driven magnetic penetration into highly conducting plasmas into which no penetration would occur without this term, has yielded an excellent test problem for a Hall MHD code: Kingsep-Mokhov-Chukbar (KMC) magnetic penetration[67].

Kingsep, Mokhov, and Chukbar have shown that the Hall MHD magnetic evolution equation becomes a Burgers equation (a nonlinear equation, which can be transformed by substitution into a linear equation with exact analytic solutions) under certain conditions. Mason, et al[97] have further developed their solution into a shock-like magnetic penetration along a density ramped channel (see Fig. 8); the result resembles the penetration of magnetic field in a plasma opening switch. The problem sets up as follows: the field evolution by the Hall term can be written

$$\frac{\partial \vec{B}}{\partial t} = - \nabla \times (\frac{1}{n_e e}(\frac{\nabla \times \vec{B}}{\mu_0}) \times \vec{B}) \tag{4.3.1}$$

This can be simplified for B_z(x) and n_e(y) to

$$\frac{\partial B_z}{\partial t} = -\frac{\partial}{\partial y}(\frac{B_z}{\mu_0 e n_e}\frac{\partial B_z}{\partial x}) = -u_w \frac{\partial B_z}{\partial x} \tag{4.3.2}$$

where $u_w = (B_z/(\mu_0 e))\partial(1/n_e)/\partial y$.

Kingsep, Mokhov, and Chukbar found shock-like solutions travelling to positive x at speed $u_w/2$ for $B_z < 0$ and $\partial n_e/\partial y > 0$. Mason's density ramp channel is a channel in which $\partial/\partial y(1/n_e)$ is a known constant value (hence u_w will be fixed), above and below which are constant density regions (see Fig. 8); in this case the penetration occurs only along the density ramp region. This is a striking, nonlinear result, and provides a clear (and numerically challenging) test problem for a Hall MHD code. It has been successfully modeled with Mason's multi-fluid/hybrid code ANTHEM[97] (ANTHEM has not proven suitable to performing the very detailed simulation of dense Z-pinch experiments such as performed here, although perhaps it could be modified to do so; it could be used to do short runs–e.g. ~1 nsec–to evaluate the stability of late-time plasma profiles generated by MHRDR).

As mentioned above, a major problem must be overcome before the additional terms can be implemented in the alternating-direction-implicit algorithm. In the limited-geometry standard MHD solved by MHRDR originally ($\vec{B}$(r,z) $\perp$ plane of computation), the equations are free of mixed partial derivatives. This has the effect that the flux of any quantity in one direction depends only on the values (and derivatives) of all quantities in that direction. Thus, the equations divide easily for purposes of the alternating-direction-implicit advance. The Hall and associated terms, however, intrinsically involve mixed derivatives; this leads to the unusual property that a gradient in one direction drives fluxes of magnetic field (or energy) in the perpendicular direction (a discussion of the physics behind this is contained in Appendix C). If these cross-derivatives must be fully implicitly evaluated to maintain numerical stability, an ADI approach will not suffice.

However, one can approximate the implicit value of the cross-derivatives by using a first-order spatial backward difference between (implicit) quantities on the line presently being solved implicitly, and quantities on the adjacent, just implicitly solved line. That is to say, $(\partial f/\partial y)^{n+1} \simeq (f_k^{n+1} - f_{k-1}^{n+1'})/\Delta y$, where k is the index of the y- (cross-) direction grid, and the prime on $f_{k-1}^{n+1'}$ is to indicate that this is an "implicit" (time $n+1$) value, but from the previously solved adjacent line, and is not being implicitly solved for on the present line. This drops spatial accuracy from second to first order, and could have the result that differences all in one direction would lead to a spatial biasing of the solution. These effects can be mitigated by alternating the order of solution of lines between bottom to top (using backward differences) and top to bottom (using forward differences), on succeeding timesteps. Because the average of a

forward difference and a backward difference is a (second-order accurate) central difference, the effect of this should be in the direction of higher accuracy.

Using the method just described for treating cross-derivatives, but in all other respects following the existing MHRDR space- and time-centered differencing scheme, the Hall and diamagnetic pressure terms were implemented. If the Hall term were to act, as suggested in the above analysis of the explicit approach's numerical instability, as a convective operator on the magnetic field, this implicit scheme could be expected to work, as in fact it does for the $(\nabla \times (\vec{v} \times \vec{B}))$ convection already implemented in the code; ADI schemes have been shown to be stable for simple convective equations[98]. Of course, the highly nonlinear nature of the Hall term's effective convective velocity (including the special treatment of cross-derivatives) could still prove troublesome.

After successful testing of simple null cases, the KMC problem was set up and run on the MHRDR Hall coding described above. Since MHRDR is written in generalized coordinates, going from cylindrical to Cartesian coordinates required only minor changes. An "open" magnetic field boundary condition, to simulate the infinite space in which the solutions were derived, had to be added; this entailed allowing magnetic flux convection through the boundaries, as if an infinite expanse of plasma and field were available. The first runs brought out some previously undiscovered bugs in the coding, which were removed. The debugged code then showed the formation of the magnetic penetration front, which begins to move along the density ramp into the field-free area. However, large positive and negative spikes in magnetic field appear and grow rapidly, disrupting the solution and driving the required timestep down unacceptably, i.e., numerical instability still appeared to be present. The coding was thoroughly

checked, and it was determined that the fluxes from one cell to another were exactly as had been planned. That nonlinearity can render unstable algorithms which are stable for related linear equations is well known; in particular, the nonlinear effective convection velocity, which involves the cross-derivatives discussed above, was known as a possible source of trouble. A simpler approach for the cross-derivatives was tried: explicit central differences; this removes any part of the cross-derivative from the implicit line solved, except as explicit matrix coefficients. This still appeared numerically unstable.

If the field equation could be considered as fundamentally a convection equation (though nonlinear), the appearance of positive field anywhere in a problem which started with all negative field raises a red flag: from where can this positive field have been convected? It was seen that the positive field spikes originated in zero-field cells, adjacent to negative-field cells in which the convection velocity pointed from the zero-field cell into the adjacent cell. The value of field to be convected, based on our center differences, was the average value of the two cells, hence less than zero. The result was that negative field was convected from the zero-field cell into the adjacent one, leaving behind a positive spike. If the algorithm used had been an explicit one, this would have been a classic example of "wrong-way" (i.e., not upwind) differencing for a convection equation: only values behind (in the sense of the convective velocity) a point can affect its value at future times [99]. The time-centered implicit algorithm using central spatial differences is supposed to be immune to this problem, because it solves for all points at one time self-consistently, but the stability analysis yielding this result is for a linear convection equation with constant convective velocity, not for the nonlinear convective velocity dealt with here. This nonlinear convective velocity,

$-\vec{J}/(n_e e)$, can change magnitude and direction as field and density vary.

However, if in this case even the implicit space-centered algorithm is going to give clearly nonphysical results, i.e., convecting field from points where there is no field to be convected, one can prevent this in the same way a proper explicit algorithm does. A donor-cell scheme convects only the quantity from the cell behind (again in the sense of convective velocity) the interface between two cells, not the average value of the two cells. This results in only first-order spatial accuracy for the spatial derivative driving convection at the interface, but insures that perturbations will be convected only in the proper direction (the so-called "transportive" property[100]), and will not convect something that is not there out of a cell. Adapted so that the correct donor-cell is selected based on the local, nonlinear convective velocity (using the second scheme for this, based on explicit central-differenced cross-derivatives), MHRDR with the Hall term finally gives the correct result: a well-defined magnetic penetration along the density ramp channel (see Figs. 9a and 9b). For the values of field and density ramp used in this problem (B=-1.5 Tesla, n_e ramped from 10^{13} to 10^{14} cm^{-3}), the shock front advances at the correct speed, approximately 2 cm/nsec. Some Gibbs phenomenon-like noise is seen originating at the steep field gradient (Fig. 9c), but this does not grow out of control. Spatial definition of the front along the channel is good, and can be improved by a finer (half the cell width) mesh (Fig. 10). Noise suppression was enhanced by limiting the timestep to 3×10^{-12} seconds (even with an implicit algorithm, smaller timesteps will still give a solution with less error $O(\Delta t^2)$), but the algorithm is stable and fundamentally correct at considerably larger timesteps.

An explicit donor-cell convection algorithm works well, but has the disad-

vantages of potentially significant numerical diffusion proportional to Δt and Δx, and strict Courant-Friedrichs-Lewy (CFL) numerical stability restriction $((v_{convective}\Delta t/\Delta x) < 1)$ [45]. One can show by doing a Hirt's analysis[101] of the time-centered implicit donor-cell scheme used here, that this differencing removes that numerical diffusion present in explicit donor-cell which is proportional to Δt. In a Hirt's analysis, one studies the differential equation which most closely corresponds to a difference equation, to reveal properties of the difference equation, such as the nature of its error terms. This procedure, applied to the implicit donor-cell scheme used here, reveals that the time-differencing numerical error is proportional to $(\Delta t)^2$ and is dispersive, not diffusive. The explicit scheme's numerical diffusion, proportional to Δt, is closely related to the CFL timestep restriction (if the restriction is violated, this error term represents a physically inadmissible negative diffusion), so it is anticipated that the timestep restriction will be relaxed.

This is confirmed by doing a von Neumann stability analysis[102,103]. For purposes of analysis, the effective convection velocity $c = (1/(n_e e\mu_0))\partial B/\partial y > 0$, and all other quantities are taken to be constant. Then the implicit donor-cell equation has the form

$$\frac{B_j^{n+1} - B_j^n}{\Delta t} = -\frac{c}{2\Delta x}(B_j^{n+1} - B_{j-1}^{n+1} + B_j^n - B_{j-1}^n) \tag{4.3.3}$$

where subscripts j refer to the spatial grid number and superscripts n refer to the timestep. If a spatially periodic solution is assumed of form $B(x,t) = e^{ikx}f(t)$ (where $x_j = j\Delta x$), and the resulting equation is multiplied by $e^{-ikj\Delta x}$, then (4.3.3) becomes

$$\frac{f^{n+1} - f^n}{\Delta t} = -\frac{c}{2\Delta x}(f^{n+1}(1 - e^{-ik\Delta x}) + f^n(1 - e^{-ik\Delta x})). \tag{4.3.4}$$

This can be rearranged to give the relative amplitudes of f^{n+1} and f^n:

$$\frac{f^{n+1}}{f^n} = \frac{|1 - \frac{c\Delta t}{2\Delta x}(1 - e^{-ik\Delta x})|}{|1 + \frac{c\Delta t}{2\Delta x}(1 - e^{-ik\Delta x})|}. \tag{4.3.5}$$

This ratio must be less than or equal to 1 if numerical stability is to hold. Because $e^{-ik\Delta x} = cos(k\Delta x) - i\, sin(k\Delta x)$, the ratio is

$$\frac{|1 - \frac{c\Delta t}{2\Delta x}(1 - cos(k\Delta x)) - \frac{c\Delta t}{2\Delta x}(i\, sin(k\Delta x))|}{|1 + \frac{c\Delta t}{2\Delta x}(1 - cos(k\Delta x)) - \frac{c\Delta t}{2\Delta x}(i\, sin(k\Delta x))|}. \tag{4.3.6}$$

The complex contribution to the magnitude, $\propto sin^2(k\Delta x)$, is the same for top and bottom. $(1 - cos(k\Delta x))$ is always between 0 and 2, and $c\Delta t/(2\Delta x)$ is always positive. Thus, the contribution to the magnitude of the real part of the upper expression is always smaller than that of the lower expression; this assures unconditional numerical stability of the algorithm. That the nonlinearity of the full set of equations solved, and the necessity of using explicit cross-derivatives in the effective convection velocity, did not apparently upset this numerical stability (as seen in the results on the KMC and Z-pinch problems), is indeed fortunate.

Numerical dispersion is present in many other implicit schemes[104] (and likely already present in the rest of MHRDR). In the time-centered implicit donor-cell scheme used here for the Hall term, there is a residual numerical diffusion proportional to Δx. This can be controlled by choosing appropriately small Δx, without any concern about simultaneously satisfying CFL restrictions. The sharpness of the magnetic penetration front visible in Fig. 9 is evidence that this implementation of the Hall term does not give unreasonably diffusive results; the "rounding" of the bottom corner, where the front leaves the initial field area, may be due to dispersive effects.

The first-order spatial accuracy of the scheme does represent a drop from MHRDR's otherwise second-order accuracy (second-order temporal accuracy is

also compromised by the use of the purely explicit cross-derivatives), so some investigation was made into alternate schemes of potentially higher accuracy. Van Leer convection schemes[105] vary between donor-cell and average quantity convection, depending on the speed of convection and whether or not the result will change the nature of the solution (e.g. change its monotonicity). Flux-corrected transport[106] convects potentially unstable quantities such as averages, then goes back in an anti-diffusion step to restore a more correct solution. Neither of these methods fit readily into the existing code. However, a simple technique was tried which brings the method closer to second order spatial accuracy: average field was convected whenever velocities and relative field values in neighboring cells were such that this could take place without causing the nonphysical changing of signs noted above. This did seem to sharpen some of the edges of the advancing magnetic front (Fig. 11), but some thought about the approach, which convects donor-cell quantitities at some points and average quantities at other points, reveals a potentially serious drawback: this may result in a distortion of the shape of a field configuration, such as a wave, as it is convected. This is because the rising part of a wave might be convected with donor-cell differencing, while the falling part could be convected with average differencing, leading to a "wave-breaking"-like effect of the wave changing shape as it travels. Because the Hall term is intrinsically nonlinear, and hence is expected to do this itself (e.g. the formation of the nonlinear shock front in the test problem), it would seem inadvisable to use numerics which might add their own, nonphysical contribution to this effect (any more than existing numerical dispersion–which causes different Fourier spatial components to travel with different speeds–already does).

An effort was made to use donor-cell convection with the original implicit

scheme, which used alternating forward/backward differences from the implicit lines for the cross-derivatives. This would be no worse in spatial accuracy (first order or better) than other donor-cell schemes, but by using more nearly implicit cross-derivatives, is closer to second-order accurate in time. Several variations of this idea were tried, and all appeared to be numerically unstable on the magnetic penetration test problem. Donor-cell Hall magnetic convection, using center-differenced explicit cross-derivatives, is the algorithm found here to correctly execute the KMC magnetic penetration problem (the differencing of this term is shown in Appendix D). This is the algorithm used in the dense Z-pinch runs reported later in this chapter, which yielded a number of interesting results. Discussion of some details regarding boundary conditions will be deferred until then, because these tie in to some of the results noted.

4.4 Diamagnetic Pressure and Electron "Work" Terms

As pointed out in the previous section, the Hall term $\vec{J} \times \vec{B}/(n_e e)$ splits up into an effective convection velocity $-\vec{J}/(n_e e)$ (the minus sign comes in because of the curl operator in Ampere's Law) and a magnetic field $\vec{B}$ to be convected (such as in equation 4.3.2). The diamagnetic pressure term, while still nonlinear and involving a cross-derivative of the electron pressure, is not clearly a convective term, but more resembles a new source of field (magnetic energy exchanged with electron thermal energy). Therefore, it may be that MHRDR's original time- and space-centered differencing will work, again employing explicit values for the electron pressure cross-derivatives. However, one must be careful to include the accompanying electron "work" ($p_e \bigtriangledown \cdot (-\vec{J}/(n_e e))$) term in the electron energy equation, to account for the energy which goes into (or leaves) magnetic field by this term (expansion or compression of the electron fluid by the magnetic field

as the two move together).

The diamagnetic pressure term was installed in the code in this manner (differencing appears in Appendix D), first without the accompanying energy term. A "benchmark" problem comparable to the Hall term KMC problem could not be found, so debugging and evaluation of the algorithm had to be done on constant-density null cases (these ran correctly), mock "Z-pinch" problems containing some very strong density gradients (along which instability patterns quickly developed), and on the dense Z-pinch problem itself. The time- and space-centered algorithm appears to run stably on these problems, with similar effects on the self-adaptive timestep to those of the Hall term (these shall be discussed in section 4.6).

The electron "work" term presents some new challenges. The Hall and diamagnetic pressure terms (and the electron current energy convection term, to be discussed later) all have the form of fluxes: terms which can be exactly spatially integrated in one direction, giving expressions at the front and back interfaces of a cell which represent the fluxes of conserved quantities entering or leaving the cell. To insure proper conservation (and for efficiency), MHRDR computes the flux at any interface only once, then uses that quantity, properly signed, for the flux leaving one cell, and the flux entering the adjacent cell. The "work" term cannot be so exactly integrated, representing a source or sink of energy at the cell (what Lindemuth calls a "force" term, as discussed in section 3.1 and Appendix D), rather than a flux. To represent such a term with similar accuracy to the flux representations, an average of second-order spatially accurate differencings of the term at the front and back interfaces of the cell was implemented. These differencings are "direct", i.e., represent the term to be dif-

ferenced exactly as written, without any intermediate analytical manipulations; this results in difference equations very close to the original differential equations. Because the electron pressure used in the diamagnetic pressure term is explicit (the cross-derivative), the electron pressure used in the work term is also explicit, for consistency. As usual, the cross-derivative current term is also explicit, other quantities space- and time-centered (differencing appears in Appendix D).

When dense Z-pinch runs were attempted with the above coding, it was found that the adaptive timestep dropped an order of magnitude or more compared to runs without the "work" term, beginning several nanoseconds into the simulation, when the first Hall effects become noticeable. Investigation revealed timesteps were frequently dropping because the iterations of the implicit line solves were not converging. In some cases, one iteration would include the Hall and associated effects, but the resulting $p_e \bigtriangledown \cdot (-\vec{J}/n_e e)$ cooling would drop the temperature (and hence electron density, which is supplied by the SESAME ionization tables as a function of mass density and temperature) below the cutoff value for Hall effects; the next iteration, without these effects, might bring conditions back (e.g., by heat conduction into the cell) where Hall effects would be allowed. Hence the iterations would bounce back and forth between with Hall terms and without Hall terms, and fail to converge within the allowable limit (typically ten iterations, and requiring that the largest quantity on a line not change by more than a factor of 10^{-5} between iterations).

To counter this problem, a switch was installed which disabled computation of Hall and associated effects at a cell for all iterations following any iteration in which the conditions caused n_e to fall below cutoff. This improved performance (larger adaptive timesteps), but one would still run into points in dense Z-pinch

simulations where the timestep would become unacceptably small (still smaller than the Hall term alone would require). The intent of the "cutoff" density coding was to prevent unrealistic (and numerically disrupting) effects in regions of plasma (e.g. "vacuum" areas) which are not part of the main plasma column. This does prevent computation of such effects in large areas of plasma which do not meet the requirements for treatment as a collisional fluid (Appendix A), but there may still be some regions above cutoff which, because of the temperature dependence of collisionality, are not properly treated as a fluid. The model used in these simulations assumes collisionality. The inclusion of the "work" term at points where collisionality is not satisfied, in energy equations which use collisional quantities such as Braginskii heat conduction and electron-ion equilibration, is physically questionable and, numerically speaking, just asking for trouble.

Therefore, a second set of numerical switches was installed. The simple collisionality parameter $v_{th_i}\tau_{ii}/a$ (equation $A.1$), which is supposed to be much less than 1, is computed, using as the scale length a, the radius, for a given axial location, within which 90% of the total axial current is contained. If this parameter is greater than 0.1 in a cell, the diamagnetic pressure and "work" term there are not computed; switching off of the Hall term itself is optional (because the Hall term does not cause numerical problems, and is arguably still present in collisionless conditions). With this modification, the code would stably run dense Z-pinch problems with Hall, diamagnetic, and "work" terms, at comparable timesteps to those with the Hall term alone. This is the final implementation of diamagnetic pressure and "work" terms, which was used in the fiber Z-pinch runs discussed at the end of this chapter.

4.5 Electron Current Energy Convection: Donor-Cell

The convection of energy by current-carrying electrons, reflected in the $\nabla \cdot (\rho\epsilon_e\,(-\vec{J}/(n_e e))\,)$ term, is a nonlinear convection problem essentially similar to the Hall magnetic convection problem; the effective convection velocity, $-\vec{J}/(n_e e)$ (essentially the electron flow velocity relative to the bulk fluid), is the same. Hence a donor-cell treatment, analogous to the one derived for magnetic convection, is the obvious choice. This was implemented (differencing in Appendix D) and, indeed, ran stably with minimal complications. The above-noted switch disabling the term at cells in violation of the collisional model was also applied to this term, for similar reasons: applying this effect at such points to a collisional energy equation is physically and computationally of dubious merit. Whether or not this term would cause the timestep problems in such a case that the "work" term caused, has not yet been determined.

4.6 Hall MHD Results on Z-Pinches[84]

The full "Hall MHD" model equations used in the following simulations of the fiber Z-pinch experiments are (equations 2.2.1, 2.2.17, 2.2.24, and 2.2.13, with the additional details noted in section 2.4):

(4.6.1) $$\frac{\partial \rho}{\partial t} + \nabla \cdot (\rho \vec{v}) = 0$$

(4.6.2) $$\frac{\partial (\rho \vec{v})}{\partial t} + \nabla \cdot (\rho \vec{v}\vec{v}) + \nabla p - \vec{J} \times \vec{B} = 0$$

(4.6.3) $$\frac{\partial (\rho\epsilon)}{\partial t} + \nabla \cdot (\vec{v}\rho\epsilon) + \nabla \cdot \left(\left(\frac{-\vec{J}}{n_e e}\right)\rho\epsilon_e \right) + p\,\nabla \cdot \vec{v} + p_e\,\nabla \cdot \left(\frac{-\vec{J}}{n_e e}\right) +$$

$$-\nabla \cdot (\kappa_\perp \nabla_\perp T) - \eta J^2 + Q_{rad} = 0$$

$$\frac{\partial \vec{B}}{\partial t} + \nabla \times (\frac{1}{n_e e}(\vec{J} \times \vec{B} - \nabla p_e) + \eta \vec{J} - \vec{v} \times \vec{B}) = 0 \tag{4.6.4}$$

where ρ is mass density, $\vec{v}$ is velocity, $\vec{B}$ is magnetic field, $\vec{J}(= \nabla \times \vec{B}/\mu_0)$ is electrical current density, n_e is electron number density, ϵ_e is electron specific internal energy, ϵ is total specific internal energy, p_e is electron pressure, p is total pressure, T is temperature, Q_{rad} is radiative energy loss, η is electrical resistivity, and $\kappa_\perp$ is (perpendicular) thermal conductivity. In this one-temperature model, separate electron pressure, electron energy, and electron number density values (needed for the Hall and associated terms) are obtained by the use of SESAME tables giving average ionization fractions as functions of density and temperature, as explained in section 2.4. Details of numerical implementation are as described in this and the previous chapter; the spatial differencing used for the Hall and associated terms, and other details, are shown in Appendix D.

It was not possible to [illegible]ly as complete a set of simulations of the fiber Z-pinch with the Hall model as it was with the basic MHD model, described in Chapter 3. Early-appearing Hall-driven instability effects cause the adaptive timestep to be reduced by roughly an order of magnitude, causing runs which took a few Cray hours to become runs in the tens of Cray hours, a significant expense. Hall runs were limited to the 750-kA peak HDZP-II discharge, which was thoroughly examined with the basic MHD model in Chapter 3. However, it was possible to do 1-mm and 1-cm axial section simulations of HDZP-II with the complete "Hall MHD" model; the Hall term alone; the Hall and diamagnetic pressure terms; and the Hall, diamagnetic pressure, and "work" terms. In runs including the energy equation terms, some computed the Hall term regardless of whether the fluid approximation was violated (unlike the diamagnetic pressure

and energy equation terms, which are not computed at points in violation; see sections 4.4 and 4.5), while other runs limited all terms to regions where proper fluid conditions were satisfied. Runs without the energy equation terms computed the Hall and diamagnetic pressure effects regardless of the fluid parameter value (although the cutoff density still disabled these effects for large portions of non-fluid "vacuum" plasma). By doing 1-mm and 1-cm axial sections, one has roughly bracketed the important instability length scales in this experiment, as discussed in Chapter 3: the 1-cm section approaches the actual 5-cm length of the fiber (and the largest observed instability features), although development of instabilities is delayed by lack of axial resolution; and the 1-mm section resolves what appear to be the fastest-growing instabilities. "Set-up" details of the runs are essentially the same as given in Chapter 3 for basic MHD runs; all grids here were 96 (radial) by 31 (axial) zones.

Because some interesting boundary effects will be noted below, it has been delayed until this section to discuss some details of boundary conditions used in the Hall model implementation. At an electrically conducting boundary, $\vec{E}_{||} = 0$. Since it is $\vec{E}_{||}$ which gives rise to this boundary's contribution to the change in magnetic flux for the cell adjacent to the boundary (Faraday's Law), no contribution to magnetic field can be allowed from this boundary, including Hall or diamagnetic field flux. This is implemented in the code: no Hall or diamagnetic field convection is allowed across a conducting boundary.

However, in computing Hall flux adjacent to a conducting boundary, if the general center-differenced cross-derivative for $\vec{J}$ is used, one needs the value of $\vec{B}$ at the boundary. For the limited-geometry resistive MHD of the original MHRDR code, it can be shown that $\partial\vec{B}/\partial n = 0$ at a solid conducting boundary,

i.e., $\vec{B}$ at the boundary is the value at the point adjacent to it in the plasma: a mirror condition. If the Hall and diamagnetic pressure terms are included, however, one has a more complicated expression for $\vec{B}$ at the boundary, relating the cross-derivative at the boundary to a derivative of $\vec{B}$ parallel to the boundary. An attempt was made to incorporate this boundary condition into the code, but it proved numerically unstable. A major factor in this instability is the fact that MHRDR does not compute quantities at (or "infinitesimally close" to) boundaries, but only starting at the plasma half a cell into the system. Hence applying boundary conditions for the adjacent boundary to the line $\Delta x/2$ into the plasma, is intrinsically an $O(\Delta x)$ error, mixing (non-boundary) plasma relationships with the complicated relationship of the cross and parallel derivatives at the boundary. To avoid this problem, an alternate $O(\Delta x)$ approximation for the cross-derivative was used: the forward (or backward) difference between the value of $\vec{B}$ at the first line in the plasma, and the value on the next line in the plasma, in the direction away from the boundary. Like the first-order accurate donor-cell scheme used for Hall convection, this sacrifices second-order "accuracy" for numerical stability and more physically consistent properties.

It will be seen that results obtained with this method agree with independent theoretical and computational results; one can interpret this as an indication that the crucial boundary condition is accurately modeled here, that Hall flux is not permitted from a conducting boundary, while the condition parallel to the boundary has less importance. One detail which was noted, concerning the adjacent-flux cross-derivative $\vec{J}$, was that the implicit value of $\vec{B}$ for the line adjacent to the boundary (not the explicit value, as used in all the other cross-derivatives) provided much more stable results than the explicit value, perhaps

following fast-changing boundary phenomena better. Cross-derivatives involving pressure at the boundary employed the mirror condition, that the wall pushes back exactly as hard as the plasma pushes on the wall, without numerical difficulties.

An interesting feature of the Hall effect is its directional asymmetry: pure MHD modes develop without regard to "up" or "down" along the axis of current flow; this is not true for the Hall effect. An example of this is the twisting of the density and pressure (including magnetic pressure) contours for Rayleigh-Taylor modes shown by Huba, et al[66], when the Hall term is included. Hall magnetic field convection is strongly directional (see Fig. 8): the primary convection of field in the KMC magnetic penetration problem was up along the field gradient, then out in the direction of penetration, up the front, and then back at the top of the density ramp channel and out the top. This was clearly shown when boundary conditions at the top and bottom of the KMC problem were "closed", i.e., allowed no Hall convection through them (as is proper for a conducting boundary, such as the axial boundaries for the Z-pinch runs): the field at the bottom became depleted, and "piled up" at the top.

The first feature noted in Hall term dense Z-pinch runs (and runs including all the other terms) is such an asymmetry in the current flow pattern (sometimes these patterns are obscured by instability development). At the anode, lines of constant axial current appear to be pinched inward (toward the axis), while at the cathode, they spread outward (see Fig. 12a). This is not seen in MHD runs without the Hall term, which show a relatively constant current distribution from anode to cathode. This effect had been predicted on theoretical grounds by Haines[107] and recently displayed in Hall MHD computational work

by Vikhrev and Zabajdullin[108]. One can interpret this phenomenon in different ways: Vikhrev and Zabajdullin describe it as "enhanced magnetic field propagation along the anode," compared to the usual resistive MHD uniform inward diffusion of field. Taking the point of view, suggested by the Hall work described here, that the Hall effect gives a convection of magnetic field in the $-\vec{J}$ (current-carrying electron velocity) direction, one can interpret this as a convection of field away from the cathode, leading to "piling-up" at the anode. This was observed in the KMC Hall test problem, and if one plots Z-pinch field profiles as a function of radius near the cathode, and compares these to field profiles near the anode (Fig. 12b), the "pinched" current pattern does correspond to the depletion/"piling-up" interpretation. Vikhrev and Zabajdullin also note that this field build-up at the anode does not lead to compression of plasma at the anode (i.e., the field "slips" through plasma, violating the ideal MHD "field-frozen-to-plasma" effect); the Hall MHD results here agree with that result, showing no plasma compression at the anode.

Runs with the Hall and associated terms in general display new small-scale instability development early in the fiber Z-pinch discharge (Fig. 13) in the vicinity of the edge of the plasma corona; such effects were hinted in the first explicit Hall term runs, although it is difficult to distinguish physical from numerical instabilities in the brief explicit code results. This is in agreement with the recent Vlasov-fluid model result of Scheffel, Arber, and Coppins[28], predicting a destabilizing trend as r_{Li}/a (the order of these terms; section 2.3) is increased. The same basic explosive instability, and instability-driven expansion, seen in non-Hall MHD runs, is still seen to assert itself here, on top of and ultimately overriding the newly added effects. The timing of the explosive instability growth

and expansion is generally a few nanoseconds earlier when the Hall terms are included, perhaps due to a "head start" associated with the early-developing Hall modes. As noted in Chapter 3, the timing of this expansion is experimentally uncertain, but the earlier trend of the Hall runs is in the right direction; experimenters are hard-pressed to get a plasma image early enough in the high-current discharges to miss the explosive expansion. It would have been rather suprising to see a drastic stabilizing trend from the Hall runs, because the basic MHD simulations already show good agreement to the experimental data from the Los Alamos device HDZP-II; this is also the case for the Hall runs.

Allowing the Hall term to be computed regardless of the value of the fluid parameters in a cell (see sections 4.4 and 4.5) gave a somewhat faster ($\sim$ 2 nsec) instability development and explosive expansion, compared to runs in which all Hall-order effects were suppressed in cells outside the collisional regime. This is a difference in timing well below anything that has been measured experimentally, although again in the direction experimenters expect. Because the other effects are of the same order as the Hall term, but the model used here is inadequate to execute them in the collisionless regime, such a run could be considered somewhat physically inconsistent. On the other hand, the Hall term appears responsible for the main features distinguishing these runs from standard MHD runs (asymmetric current flow pattern, early appearance of instabilities), and it does continue to exist in the collisionless regime[52].

The electron current energy convection term did lead to a flow of energy in the direction of $-\vec{J}$ (current-carrying electron velocity), as shown in Fig. 14, quite analogous to the Hall-driven flow of magnetic field. Again, however, this did not substantially change the ultimate explosive plasma behavior.

The approach taken in these simulations has been to try to very closely model specific experiments: in this chapter, specifically the Los Alamos experiments, to which this author has had the greatest access, and in which the simulations (and corresponding experimental data) indicate that the collisional MHD model used stays valid for long enough in the discharge to largely determine the results. Other fiber-initiated Z-pinch experiments may substantially avoid this collisional MHD regime[22,54] (the "plasma-on-wire" technique discussed in the next chapter may be a means to do this). In that case these (collisional) "Hall MHD" results would not be expected to be valid, because there are other finite-Larmor-radius effects of potential importance in the "collisionless MHD" regime. This includes effects such as gyroviscous stress[52]; furthermore, certain features of the model used here, such as compressibility, should not be used in a collisionless MHD model [40]. It should be possible to adapt the present code to such a collisionless MHD model, but that is beyond the scope of the present work.

CHAPTER 5: TWO PROMISING RELATED FUSION CONCEPTS

5.1 Deuterium Shell and "Plasma-on-Wire" Implosions

Variations of the deuterium-fiber-initiated Z-pinch concept (in fiber thickness, current ramp, and "flash" plasma initiation, as discussed in Chapter 3) simulated to date have not shown any fundamental improvement over the basic HDZP-I/II-type experiments, in terms of avoiding instabilities and the explosive expansion which prevent fusion temperatures and densities from being reached. As has been mentioned before, such an expanded plasma might serve as a suitable "magnetized target" to fill a chamber, which would then be imploded to raise the target plasma to fusion conditions[91,92]. To evaluate such a "magnetized target fusion" (MTF) concept, including various means and geometries of implosion, plasma-wall interactions, and fusion processes, is beyond the scope of this thesis. However, the work reported here is a good starting point for modeling a fiber-Z-pinch-based MTF experiment.

The computational tool developed here may be useful in evaluating and optimizing some related experimental concepts, which vary more significantly from the original fiber-pinch approach. Two such concepts are the magnetic implosion of hollow, annular columns of deuterium, and the "plasma-on-wire" (POW) discharge through a low-density plasma surrounding a central fiber core. Both concepts have been the subject of some recent experimentation, with encouraging results. This author has therefore begun a computational exploration of these concepts.

One cannot assume that, because the model used here can be argued to be valid, and agrees with experimental results, in the fiber Z-pinch case, such will still be true for any proposed experiment. It will be seen, however, that these

related experiments do fall within similar regimes to those of the fiber Z-pinch, so similar modeling techniques should apply. As in the case of the fiber-pinch modeling, careful attention must be paid to the details of the experiments to be modeled.

5.2 Implosion of Hollow Deuterium Cylinders

Recent experiments at the SATURN high-current, fast-current-rise facility at Sandia National Laboratory have imploded hollow "gas-puff" deuterium columns with a peak current of 8 to 11 MA reached in approximately 40 nsec[109]. From a total deuterium mass of 1 mg, total neutron production has been $O(10^{12})$, with good evidence (better than 10% isotropy) that these are largely from thermal reactions, and not from a beam-target interaction. A slight enhancement of the neutron yield (up to 3×10^{12}) was observed when a central, CD_2 fiber was included.

Parks suggested a fusion scheme also involving an imploding deuterium shell[110], although in his concept the fusion conditions were reached by a central, HDZP-II-like fiber Z-pinch (on which the work presented here casts doubt), and the separately driven shell largely provided fuel for a propagating fusion burn. A hybrid of Parks' concept and the SATURN experiments is this: apply the SATURN current ramp to a thin, solid deuterium shell of radius 1 cm, surrounding a solid deuterium fiber; it is possible enough field/current will diffuse through the initially solid shell that the central fiber will form a fiber-initiated pinch, on which the outer D shell will implode.

Such a concept was simulated in one and two dimensions using the basic MHD model of Chapter 3, following the practices used here in fiber-pinch simulations. A 10 MA in 40 nsec current ramp provided the radial wall magnetic field

boundary condition; a 300-point stationary nonuniform radial grid was used, with the grid spacing varied to provide 2 μm resolution in the vicinity of the solid deuterium (at the center and at the shell). Apart from the half-solid density deuterium fiber ($30\mu m$ diameter) and shell ($10\mu m$ thick at 1 cm radius), and initial current-path coronas of 10^{-5} times solid density and temperature 2 eV, extending 25 μm from the surfaces of the solid, a room-temperature, $10^{-9}\times$ solid density "vacuum" filled the region between the shell and fiber, and the region outside the shell to 1.5 cm (see Fig. 15). Two-dimensional runs used 31 axial points covering a section 1 mm in length (the actual experimental chamber is 2 cm in length, but experience with dense Z-pinches suggested a 1 mm section would give the most appropriate instability resolution).

The dimensions of the shell described above were chosen so that the total mass of deuterium involved (for a 2-cm section) would be about 1 mg, approximately the same as used in the Sandia gas-puff implosions. Some current was observed to diffuse through to the fiber well in advance of the imploding shell material, leading to a weak fiber pinch (certainly not near the 1-MA, HDZP-II-idealized fusion source envisioned by Parks), but the bulk of the heating and neutron production came from the radial convergence of the shell material, which had come to resemble a $10^{-2}\times$ solid density, several mm-thick, 100-eV plasma annulus as it approached the center. Convergence produced temperatures of several keV in a column of several mm radius at $10^{-2}\times$ solid density for 10-20 nsec; this is enough to produce the observed $O(10^{12})$ D-D neutrons (Fig. 16). Conditions of $O(10^{21}$ cm$^{-3})$ at $\sim$ 5 keV are sustained for 10 nsec, resulting in an $n\tau$ of order 10^{13} cm^{-3}sec, close to the controlled fusion goal of 10^{14}. Some instability development was noticeable, particularly in the lower-density region

between the fiber and annulus. These instabilities appeared to be "swept-up" by the rapidly imploding plasma, and resulted in no appreciable reduction in neutron yield, as determined by comparing 1-d and 2-d runs. Some "spreading" of the plasma density (and corresponding spreading out in time of neutron production) did occur. An implosion from something on the order of radius 1 cm, to a plasma column of approximate radius a few mm, does not sound like a very impresssive convergence, but the temperatures and densities reached over a 10-20 nsec period result in rather good plasma conditions for fusion and neutron production. A variety of one- and two-dimensional runs were tried, varying the shell thickness from 1.2 to 25 μm, and including a 120-μm central fiber, a 30-μm fiber, or no fiber at all. It was found that the presence or absence of the fiber made very little difference to the neutron yield. The best neutron yield ($O(10^{13})$) was obtained with a 5 μm shell, or about 0.5 mg total deuterium.

Sandia National Laboratory has proposed to build an electrical pulsed power generator capable of driving up to 60 MA with an 80-100 nsec peak[111] (high explosive flux-compression current generators have been developed by the Russians capable of at least 30 MA, but only over μsec rise times; recently at Los Alamos, a high explosive current generator delivered 12 MA to a load in 400 nsec). A series of 1-d deuterium shell implosion simulations was done to examine what sort of performance could be expected, if the Sandia-proposed generator became available (or explosive generators can be adapted to faster rise times). These runs were set up similar to the above shell-implosion runs, except the current ramp was to 50 MA at 80 nsec. No central fiber was included, and shell thicknesses were 50 μm to 500 μm. D-D neutron yields were greater than 10^{16}, with the best 10^{17} from a 100-μm-thick shell (a single 2-d run has been taken to 51

nsec, yielding more than 10^{14} neutrons to that point). Peak magnetic fields were over 100 MG, high enough that fusion-produced alpha particles would be retarded from leaving the plasma, leading to additional heating and neutron yield. Because the 10-MA shell-initiated simulations did not show substantially different neutron production from the gas-puff initiated experiments, it is not clear whether or not starting with a solid shell in the 50-MA regime is critical to the results predicted by the simulation. Simulations of 10-MA and 50-MA annular gas-puff implosions are planned, to help answer this question.

D-D neutron yields of 10^{13} from the 10-MA existing generator at Sandia suggest the possibility of 10^{15}, if a mixture of deuterium and tritium is used. This would be a significant production of neutrons and fusion energy. Conditions reached in the 50-MA simulation runs, in which considerably higher numbers of neutrons are produced, may approach D-T ignition conditions, when the additional alpha-heating mentioned above (which the present code is not capable of computing) is included.

Similar plasma temperatures and densities exist in these simulations to those discussed in Appendix A, where the validity of the fluid model for the dense Z-pinch is established. The effective scale lengths in this case are larger, on the order of mm, which helps to satisfy the fluid conditions. In contrast to the fiber-initiated pinches, where instabilities lead to high-temperature, low-density regions of questionable fluid conditions, the highest temperatures for the implosion pinches are reached at the center, in high-density regions; thus the fluid model is valid longer in these simulations. However, temperatures above a few keV do still lead to breakdown of the collisional fluid model, as represented in equation $A.3$ of Appendix A. Because the radial scale lengths of these plasmas

are greater, and due to the larger fields, the Larmor radii are smaller, the Hall and associated terms are smaller and less significant than for the fiber pinch; this is fortunate, because the computation times for the 2-d basic MHD simulations of these implosions are already very large.

5.3 "Plasma-on-Wire" Implosions

A series of Z-pinch experiments[94] performed by Etlicher, Choi, Wessel, Chuvatin, and others (a French-British-American-Russian collaboration) have shown remarkable differences in the heating and apparent stability of discharges initiated on a wire surrounded by a low density "puff" plasma, compared to bare wire-initiated discharges. These experiments have involved a variety of materials, often with the wire material different from that of the gas puff, but sometimes with gas puff and wire all one material, such as aluminum. A Z-pinch initiated on a bare aluminum or other wire rapidly goes unstable ("exploding wire"), producing hot spots whose temperature can be inferred from the spectroscopic details of the material. "Plasma-on-wire" discharges, however, tend to show (in visible and X-ray radiation images) a very compact, uniform, straight line of very high temperature; often it is several keV, higher than even the hot spots of a corresponding exploding wire. This is suggestive of some stabilization mechanism allowing much more uniform heating than is generally seen in pure exploding wire discharges (or indeed, in the deuterium fiber discharges modeled here).

Having developed a tool to model deuterium fiber discharges, it should be useful as a first step in evaluating single-material wire and plasma-on-wire discharges. This will allow us to address the question of whether or not "plasma-on-wire" might be helpful in the stabilization of deuterium pinches. In general, radiation is a complicating factor for plasma discharges of materials heavier than

hydrogen, particularly if the plasma becomes optically thick. In that case, one must track the radiative energy transport from place to place; it has been fortunate that the deuterium-fiber-initiated plasmas modeled here have been optically thin in the important frequency range ($\omega_{rad} > \omega_{pe}$), so that radiation has only produced an energy loss term. For some plasma-on-wire discharges, the optically thin assumption may still be good; even if not, 2-d MHD modeling may still offer insights into the important physics.

Details of an all-aluminum plasma-on-wire discharge were obtained from Etlicher[112], and the problem was run using the 1- and 2-d basic MHD model of Chapter 3. The current ramp went in two stages to a 250-kA peak at 70 nsec (see Fig. 17), applied to a 30-μm-diameter aluminum wire with and without a 10^{17} cm^{-3}, 0.5 eV aluminum puff plasma extending out to a radius of 2.5 mm. A fixed 96-point radial grid extending to 4 mm was used, with a "vacuum" of $10^{-9}\times$ solid density at .025 eV; 2-d runs were done for a 1-mm , 31-point axial section. Of course, appropriate SESAME tables for aluminum were substituted for the deuterium tables. The bare wire discharge displayed significant instability development by the 70-nsec current peak, with formation of hot spots (Fig. 18). At this point the plasma-on-wire discharge appeared much more uniform, with a sudden jump to keV temperatures at the surface of the wire (which has carried very little current until then) when the low-density puff plasma converges at the wire (Fig. 19). This might represent a means of jumping a micron-size wire or fiber to high current and temperature almost instantaneously; it appeared desirable to do this for deuterium discharges, to avoid the low-density unstable corona (which motivated the flash-ionization simulations discussed in section 3.2).

Whether the sudden, uniform jump to high temperatures, at the time of current peak/puff convergence, causes a strong, uniform diagnostic image which masks later instability development (analogously to the early visible and shadowgram images of deuterium fiber Z-pinches), or actually brings the wire to a high-density, high-temperature (collisionless MHD?) stable regime, is a question to be answered by future computation and experiment. The 2-d POW simulations done to date run into timestep trouble at the point of current peak/puff convergence on the wire. This may be due to so much heating happening in such a small region, at the surface of the wire, and might be remedied by finer spatial resolution there.

A small number of 1-d, and one 2-d, simulations of plasma-on-wire discharges with deuterium puffs and wires were run, using the same current ramp and other details as used in the above discussed aluminum POW simulations. The 1-d runs showed a notable difference from aluminum POW runs: when the aluminum puff converges on the wire, the current is brought down to the wire and stays there (Fig. 20a), while for the deuterium case, the puff converges on the fiber, but then bounces back to near its original radius (Fig. 20b). The 2-d deuterium run showed considerably greater instability development throughout the puff plasma, than seen in aluminum runs. Several factors come to mind to explain these differences. One is the relative differences in resistivities: the aluminum puff plasma and the aluminum wire are both conductors, so that the current carried by the puff is readily accepted by the wire at convergence; while the deuterium fiber (to the extent it remains cold, which it does until near the the 70-nsec current peak) is initially an insulator, less able to accept current from the puff. A second factor is the ability of the aluminum wire to accept a

large amount of energy from the ~100-eV puff plasma and re-radiate it as line radiation, while in this range deuterium is not nearly as strong a radiator. Another factor is the relative masses of the two materials: the deuterium plasma is much lighter, so an equal amount of energy can push it around (i.e., collapse, re-expand it, or develop instabilities) much more readily. The current ramp and other details used in these simulations were experimentally optimized for the aluminum POW system, so it is probable that different values would be optimum for deuterium.

It is likely to take considerably more computational and experimental research to determine if POW techniques can lead to deuterium discharges with the desired stability. The simulations done to date do support the view that the POW technique can produce greater heating levels and uniformity in higher-Z material discharges, such as aluminum, than can be produced with traditional Z-pinch methods. Hence this technique may lead to a useful flash radiation source for industrial applications.

CHAPTER 6: CONCLUDING REMARKS

6.1 Summary

In this thesis, a very detailed computational model of a class of controlled fusion experiments, the deuterium-fiber-initiated Z-pinch, has been constructed (the primary examples modeled here of such experiments are the "high-density Z-pinches" HDZP-I and -II, constructed by J. Hammel, et al[3,4,14]). It has been shown that the collisional magnetohydrodynamic equations are valid for substantial portions of such experiments. A two-dimensional magnetohydrodynamics computer code has been adapted to simulate these experiments in a very direct and detailed fashion, following the development of the fiber from frozen solid to high-temperature plasma. In this way, one obtains a direct prediction of the details and outcome of an experiment, which can then be compared to real data. To facilitate this comparison, diagnostic images of the plasma, such as shadowgrams and interferograms, have been generated from simulation results.

A major deficiency in applying the standard magnetohydrodynamic model to such Z-pinches has been identified: the assumption, that ion Larmor radii are much less than relevant plasma scale lengths, is not satisfied. The terms which have been ordered out of the model based on this assumption, in the collisional regime, are the Hall and diamagnetic pressure terms in the magnetic field evolution equation, and electron pressure "work" and electron current energy convection terms in the energy equation(s). These terms have been added to the computational model (which this author now refers to as "Hall MHD"), and demonstrated to give results which are consistent with known theoretical and computational predictions.

Both the standard magnetohydrodynamic model, and the enhanced "Hall

MHD" model, predict that the deuterium-fiber-initiated experiments modeled here undergo explosive instability-driven expansion shortly after the fibers have become fully ionized. Shadowgrams and interferograms generated from simulation results show good agreement with experimental data, supporting this prediction. The "Hall MHD" model predicts slightly faster instability development and expansion, which is in agreement with experimenters' qualitative observations, but beyond confirmation with present quantitative experimental data. Simulations of variations to present fiber-initiated experiments in fiber thickness, current ramp, and plasma initiation techniques have not shown any exceptions to the instability/expansion problem seen. A fiber-initiated Z-pinch might serve as a suitable target plasma for a "magnetized target fusion" implosion, but this requires a secondary plasma compression scheme to reach fusion conditions.

The computational techniques developed here have proven useful in beginning the evaluation of two related fusion concepts, which involve similar plasma scales, conditions, and geometries. Simulations of the implosion of hollow deuterium shells, with fast-rising (O(100 nsec)) 10- to 50-MA current ramps, indicate plasma conditions, which would produce significant amounts of fusion energy and neutrons, may be obtained. Simulations of "plasma-on-wire" discharges, in which a low-density Z-pinch plasma implodes on a central fiber or wire, suggest that such techniques may produce hotter and more compact pinches than traditional Z-pinch techniques.

6.2 Deuterium-Fiber Pinches: Future Work

Although it is argued that the fundamental details and results of the experiments modeled here, primarily the Los Alamos HDZP-I and -II devices, have

been reasonably correctly simulated, and the variations examined did not show substantial ultimate differences in results, one cannot claim that these results hold for all fiber-initiated Z-pinches. The philosophy behind the simulations done here is that details are important, and though an attempt has been made to include all the details expected to be relevant, this is obviously limited by the knowledge of the modeler. Furthermore, the details of the experiments included here are subject to endless variation by other experimenters; as well, the details of the computational model are subject to debate. It would be very desirable to run a series of controlled experimental variations on one machine, well diagnosed, and compare these to a corresponding series of simulations. This may be possible, in collaboration with the fiber Z-pinch group led by M. Haines at Imperial College.

A major change from the type of experiment modeled here, which has been shown to exist for substantial times in the collisional plasma fluid regime, would be an experiment which operated primarily in the collisionless, or "collisionless MHD", regime. At first glance, it might appear a fiber-initiated pinch would have to go through the collisional regime, with its instability hazards so repeatedly illustrated here, to get to the collisionless regime, in which stabilizing conditions might prevail. But techniques, such as the "plasma-on-wire" discussed in Chapter 5, show the possibility of producing very sudden changes in temperature in a material; even a very dense material can become a collisionless plasma, if its temperature is raised high enough. To adapt the present code to give consistent results in the "collisionless MHD" regime, or even to follow collisionality and adapt "on-the-fly" from collisional to collisionless fluid models, should be possible. This could give very useful results in systems, such as the dense Z-pinch,

which can spend time in both regimes.

It has been argued that experimental evidence supports the geometric limitations of the model used here ($\vec{B} \perp$ plane of computation; variation of quantities only as functions of r and z). The agreement with experiment, of the results of simulation with those limitations, supports this argument. The absence of the ideally predicted m=1 (non-azimuthally-symmetric) modes cannot be explained by such a model, nor can it deal with the experimental evidence (Fig. 2a) of such asymmetry, at late times in the discharge. Because including the many important details of the experiments involves such computational demands, on even the 2-d code employed here, one imagines a 3-d fluid code would need to be considerably more efficient, but equally robust, to tackle these issues. A shorter-term solution would be to take plasma profiles generated by the 2-d code at intervals in the discharge, and using these as initial conditions, run a 3-d code for short times, e.g. one nanosecond, to get some idea of m=1 stability at those intervals. At later points, when the fluid model is breaking down, one could do the same thing with 2-d or 3-d particle or hybrid codes, for insight into collisionless behavior. Continuing advances in the power of computers should make it possible to handle the full 3-d problem, not too many years into the future.

This author would like to make some shorter-term enhancements to the computational model. The thermoelectric Nernst and Ettinghausen effects have been mentioned as of potential importance when electron and ion temperatures become decoupled, which can occur, for example, in the case of instability ion heating. Enabling the code to run in two-temperature mode with SESAME equations of state, rather than the ideal gas model which had to be used to date, would be desirable. This would also open the possibility of doing two-temperature runs

with the full "Hall MHD" model, although unless code efficiency is substantially improved, this may be just too costly in computer time ("Hall MHD" runs with one temperature are already very expensive, in the tens of Cray hours). Support for some of this work appears available, but the opportunity to pursue major projects such as "collisionless MHD" is unclear at this time.

6.3 Other Hall MHD Applications

The "Hall MHD" computational model constructed in this work may prove useful in other applications. One application, made obvious by the KMC magnetic penetration problem used to "benchmark" the code, is modeling of plasma opening switches. Because this code has been developed to model specific experiments by including important details, such as "cold-start" initial conditions, etc., it may be possible to model a given opening switch experiment more closely than with previous Hall codes. If an experimental plasma spends significant time in the collisional regime (like the Z-pinches modeled here), the inclusion in the present code of the diamagnetic pressure and associated terms may bring new results; this author is not aware of any other "Hall MHD" computations which include these additional terms.

Another active Hall MHD research area is magnetospheric and other space plasmas. However, such plasmas are generally collisionless. While this code, including the Hall term, will run in the "collisionless MHD" regime, the consistency of the results has not been carefully examined, as discussed several times in this paper. Hence adaptation of the code for the collisionless regime, which above was noted as desirable for evaluation of some variations of fiber Z-pinch experiments, could also be useful toward some space plasma applications.

6.4 Potential of Shell and "Plasma-On-Wire" Implosions

The potential of hollow deuterium shell and "plasma-on-wire"-type Z-pinch implosions, as relatively inexpensive fusion concepts in the original spirit of the fiber Z-pinch, appears high. These are both being pursued actively by small research groups, who have expressed enthusiasm to this author about collaboration. A third concept, which has been mentioned briefly in this paper, is a fiber-Z-pinch-target "magnetized target fusion" experiment. There are many unanswered and critical questions regarding all these approaches, but these questions can be answered at modest cost (without investment of billions of dollars). The achievement of controlled fusion in one of these inexpensive ways would not immediately translate into cheap, clean, and safe energy, but it would be a very significant step toward such a goal. These methods may also lead to a useful flash X-ray source. Perhaps a completely "pure" scientist would not be concerned with such considerations, but this author has always intended to do science which can be useful to humanity.

6.5 Acknowledgments

There are many, many people who have provided assistance, advice, and encouragement to the author of this dissertation. To them all, I express my gratitude.

The bulk of my college education has been at numerous campuses of the University of California, primarily Santa Cruz, Santa Barbara, and Los Angeles. I have received generous support, financial and otherwise, at these institutions; innumerable faculty, staff, and students have contributed to my education there. Most recently, in my five years as a graduate student in the UCLA Department of Physics, I have been greatly supported by many members of that department.

A large part of my research training and thesis research has been at another institution operated by the University of California: Los Alamos National Laboratory. First visiting there in the Summer of 1986 as a Magnetic Fusion Energy Technology Fellow, from the start I was enthusiastically welcomed by staff and management into their research programs. Since 1991, I have been financially supported full-time by the Lab in completing my thesis research. I hope that I will be able to repay their investment in me, by contributing to the success of future research programs there.

A number of individuals deserve special mention. The late Jay Hammel, to whom this thesis is dedicated, welcomed me into the field of dense Z-pinches; it has been a pleasure to work with him and his fine experimental research group. Rick Nebel was my first research mentor at the Lab, and gave me a great start in the computational plasma physics business. Irv Lindemuth has been my closest collaborator and supervisor on this thesis research. He has been generous with his time and energy in my behalf, and I look forward to continuing our collaboration. John Dawson, my thesis advisor at UCLA, has been a continuing source of new ideas, valid criticisms, and frequent encouragement; all graduate students should be so lucky as to have an advisor like John. I have been fortunate to meet many of the scientists cited in the References of this thesis, and discussions with them have been very productive; in particular I should mention Malcolm Haines, with whose enthusiastic dense Z-pinch research group I hope to continue collaboration.

It is my hope that by doing honest, solid, and useful scientific research, I shall be able to repay the investment that all these people have made in helping me to become a scientist.

All previously published material which has been reproduced here (from

Sheehey, et al, in References 82-84, and Lindemuth, et al, in References 38, 91, etc.) has been prepared by U.S. government employees as part of their official duties. Therefore it is not eligible for U.S. copyright; nor is this dissertation to be copyrighted, for the same reason.

APPENDIX A: VALIDITY OF FLUID MODEL

A common criterion for the validity of MHD fluid theory[40] is that the ion-ion collision time be much shorter than the ion thermal transit time:

$$\frac{\tau_{ii}}{\tau_{th_i}} = \frac{v_{th_i}\tau_{ii}}{a} \ll 1 \tag{A.1}$$

where a is an appropriate scale length of the system, here the effective radius of the plasma column. That the mean free path of a particle be much shorter than the scale length a will also result in the above restriction. For a two-fluid model, this same criterion holds for the electron fluid, because the $(m_i/m_e)^{\frac{1}{2}}$ factor needed to obtain v_{th_e} from v_{th_i} is cancelled by the $(m_e/m_i)^{\frac{1}{2}}$ factor to obtain τ_{ee} from τ_{ii}; hence $v_{th_e}\tau_{ee}/a$ is also much less than 1. What these criteria amount to, is that particles in the plasma must experience sufficient collisions, as they traverse the system, that their distribution functions will be nearly Maxwellian; then, by taking moments of the kinetic equation, one obtains (as did Braginskii[31], et al[40,43]) a set of equations for the familiar fluid quantities density, velocity, etc.

More strictly, if ion-electron energy equilibration is to hold, one must have:

$$\frac{\left(\frac{m_i}{m_e}\right)^{\frac{1}{2}} v_{th_i}\tau_{ii}}{a} \ll 1. \tag{A.2}$$

For a (single-temperature, $T_e = T_i$) deuterium plasma, this requirement can be written in terms of density and temperature as

$$\frac{2.2 \times 10^{14} {T_{eV}}^2}{(n_{cm^{-3}} a_{cm})} \ll 1 \tag{A.3}$$

where T_{eV} is temperature in eV, $n_{cm^{-3}}$ is (number) density in cm^{-3}, and a_{cm} is in centimeters.

A 100 eV plasma of dimensions similar to the fibers used in these experiments (radius 15 to 60 μm, solid density $\sim 5\times10^{22}\mathrm{cm}^{-3}$) meets this requirement. The important coronal plasma generated as the fiber ablates, in which the first instability development seen in the simulations occurs, may have densities several orders of magnitude below solid; however, its temperature is often lower, and it exists at radii of several hundred microns to several millimeters. Hence the factors compensate for each other, and the fluid parameter generally remains in the required range.

Because the actual plasmas created in the experiments heat and expand nonuniformly, the relevant scale length to use is subject to question. From the computed density and temperature profiles, plots were made of the fluid parameter (A.1), using as the scale length a, the radius, for a given axial location, within which 90% of the total axial current was contained. For the most part, these plots showed the plasma column remained within the fluid regime until very deep m=0 instability development, with accompanying high-temperature, low-density regions, occurred.

A cutoff density, below which ohmic heating (and later, Hall effects) was turned off, was employed in the calculations to prevent unrealistic heating (and exagerrated Hall effects) in low density, non-classical-fluid "vacuum" regions. Both fixed cutoff densities, and cutoff densities which were varied as the plasma developed so that 99% of the mass of the plasma remained above cutoff, were tried, without significant differences in the results.

The strict single-temperature, single-fluid criterion above may be violated as the plasma heats and expands, as noted in Chapter 1, even while the ion and electron fluid criteria are still satisfied. This motivated the two-temperature

MHD work reported in Chapter 3.

Ideal MHD fluid theory orders out the Hall ($\vec{J}\times\vec{B}$) and diamagnetic pressure terms in Ohm's Law, on the basis of small ratio of Larmor radius to plasma scale length[40](this is discussed further in section 2.3 and Appendix C). That this ratio may not be small in a Z-pinch, with its field null on axis, is well known[19,41](also see section 2.5). Plots of this parameter from the MHD simulations (Ch. 3) showed this as well, motivating the implementation of Hall MHD in the code (Ch. 4).

APPENDIX B: IMAGING OF THE PLASMA

The bending of light rays by density gradients in a plasma allows imaging of the plasma with a number of techniques known as Schlieren methods or shadowgraphy (Los Alamos experimenters refer to their images as "shadowgrams")[113]. In the Los Alamos scheme, a 530 nm laser shines through an area of plasma (typically 1 cm^2), on which an imaging lens is focussed. Rays which undergo large deflection, due to a high density gradient, miss the lens, leaving a dark area (shadow) on the image collected (photographically or electronically).

When higher-current experiments appeared to lack steep enough density gradients to produce good shadowgrams, interferometric imaging was employed. The phase shift of the beam passing through the refractive plasma, relative to a vacuum reference beam, is used to generate interference fringes, which map the density of the plasma[113]. With these methods, the laser can be "flashed" for extremely short times, so that it has been possible to generate highly time-resolved (better than 0.2 nsec) images of the plasma.

To generate comparable diagnostic images from simulation density profile results, one solves the Euler-Lagrange equation[114], which describes the path of a light ray travelling through a medium of varying index of refraction μ:

$$\frac{d}{ds}\left(\mu\frac{d\vec{R}}{ds}\right) = \nabla\mu \tag{B.1}$$

where $\vec{R}$ is the position of the ray.

This may be expressed as six first-order O.D.E.'s:

$$\frac{df_x}{ds} = \frac{d\mu}{dx} \tag{B.2}$$

$$\frac{dx}{ds} = \frac{f_x}{\mu}$$

(similarly for y and z).

A seventh term may be added to this to compute the phase (shift) of the wave ϕ travelling through the refractive medium:

$$\frac{d\phi}{ds} = -\frac{\omega\mu}{c} \tag{B.3}$$

where ω is the angular frequency of the wave.

Refractivity of a fully ionized plasma is given by:

$$\mu = \left(1 - \frac{{\omega_{pe}}^2}{\omega^2}\right)^{\frac{1}{2}} \tag{B.4}$$

where ${\omega_{pe}}^2 = e^2 n_e / \epsilon_0 m_e$.

However, for significant parts of the discharge, there may remain solid, non-ionized material which also has refractive qualities (in fact, of converging effect, as opposed to the diverging effect of plasma refractivity). An empirical equation for the refractivity of liquid deuterium, believed applicable for solid of similar densities, is used[115]. A grid of light rays is then traced through the computed density distribution (n_e for plasma refractivity, neutral density for solid refractivity) to generate our predicted shadowgram/interferogram, using a packaged O.D.E. solver, LSODE[116].

Test cases of this ray-tracing algorithm on deeply m=0 modulated Gaussian radial plasma density distributions, pointed out something critically important in the interpretation of experimental shadowgrams: geometric factors (imaging lens size and distance from the plasma) may cause the shadowgram image to differ drastically in size and modulation from the actual plasma.

APPENDIX C: PHYSICS OF HALL AND ASSOCIATED TERMS

In examining the physics of the Hall and associated terms, it is useful to look at some key steps in the derivation of single fluid MHD equations from Braginskii's two-fluid transport equations, as done in Chapter 2. A first important step is the dropping of the electron inertia term (2.2.2) from the electron momentum equation (2.1.3, 2.2.3, 2.2.8). This has the effect of saying that, on the time and length scales of the model, all forces on the electron fluid–electrical ($\vec{E}$), magnetic ($\vec{v}_e \times \vec{B}$), (electron) pressure ($\nabla p_e/(n_e e)$), and those due to collisions with ions (resistive, $\eta\vec{J}$)–are in balance, that is, sum to zero. Solving this equation for $\vec{E}$ gives an "Ohm's Law:"

$$\vec{E} = \frac{1}{n_e e}(-\nabla p_e) + \eta\vec{J} - \vec{v}_e \times \vec{B}. \tag{C.1}$$

One can eliminate $\vec{E}$ from this equation by application of Faraday's Law, $\partial\vec{B}/\partial t = -\nabla \times \vec{E}$ (note also that in this model $\vec{J} = (\nabla \times \vec{B})/\mu_0$):

$$\frac{\partial \vec{B}}{\partial t} = -\nabla \times \vec{E} = -\nabla \times (\frac{1}{n_e e}(-\nabla p_e) + \eta\vec{J} - \vec{v}_e \times \vec{B}). \tag{C.2}$$

This equation gives the time evolution of magnetic field as a function of magnetic field and electron pressure, density, and velocity (where plasma resistivity η is a function of these four quantities). It is limiting forms of this equation which determine the magnetic field behavior in the various MHD models discussed here.

Jumping first to the "Ideal MHD" model (some assumptions of which shall be more carefully discussed below), in which the $\nabla p_e/(n_e e)$ and $\eta\vec{J}$ terms are negligible, and the dominant part of electron velocity in $\vec{v}_e \times \vec{B}$ is given by simple plasma (center-of-mass) velocity $\vec{v}$, one has:

$$\frac{\partial \vec{B}}{\partial t} = \nabla \times (\vec{v} \times \vec{B}). \tag{C.3}$$

This equation leads to the interesting result[117,118] that magnetic flux through any surface area moving with the (Ideal MHD) plasma is constant; in effect, plasma is "frozen to the field lines," and magnetic field is convected with plasma velocity $\vec{v}$.

If one maintains the more exact $\vec{v}_e \times \vec{B}$ expression (and then uses for $\vec{v}_e$ equation 2.2.9, $\vec{v}_e = \vec{v} - (\vec{J}/(n_e e))$),

$$(C.4) \qquad \frac{\partial \vec{B}}{\partial t} = \nabla \times (\vec{v}_e \times \vec{B}) = \nabla \times (\frac{-1}{n_e e}(\vec{J} \times \vec{B})) + \nabla \times (\vec{v} \times \vec{B}).$$

This is the field equation commonly used in a "Hall MHD" model (although in this paper, additional terms of similar order are retained). It can be seen that almost the same "frozen to the field lines" result can still be applied, except that the field is now frozen to the electron fluid, and convected with electron velocity $\vec{v}_e$. This has been noted by Coppins et al[19], and is a major reason why the Russian literature often uses the term "electron magnetohydrodynamics"[119] in reference to Hall MHD. In this light, the Hall term, $\vec{J} \times \vec{B}/(n_e e)$, is seen as a correction to the Ideal MHD assumption that electrons (and field) are convected with center-of-mass velocity $\vec{v}$. The odd result that convection of $\vec{B}$ in one direction is driven by its derivative in a perpendicular direction, arises from the Hall term's cross-product of $\vec{J}$ (which contains the cross-derivative of $\vec{B}$, since $\vec{J} = (\nabla \times \vec{B})/\mu_0$) with $\vec{B}$, to which the Faraday's Law curl operation is then applied.

If the Hall term is an important correction to the field equation, one expects that the $\nabla p_e/(n_e e)$ term may also be important; these terms are of similar order, as noted in section 2.3. The $\nabla p_e/(n_e e)$ term leads to an effective current corresponding to a magnetic field tending to reduce the existing field; hence it

is called the diamagnetic pressure term. It is relatively easy to see the reason for this diamagnetic current in the case of an isothermal plasma, where an electron pressure gradient corresponds to an electron density gradient $kT_e \nabla n_e$ [120]. Through any fixed volume element, Larmor gyration of particles around the field lines will lead to a fluid drift perpendicular to $\vec{B}$ and ∇n_e. This is because more particles from the high-density side will gyrate through the element, than corresponding particles on the opposite side of their orbits (moving in the opposite direction) from the low-density side.

Thus the Hall and diamagnetic pressure terms can be seen as corrections to the motion of the electron fluid, which ultimately determines the evolution of the magnetic field (equation C.2). The electron energy convection term (see section 4.5) and the electron pressure "work" term (section 4.4) in the energy equation, which are included here in the complete "Hall MHD" model, also arise from this same attention to the details of electron fluid motion. The electron energy convection term comes directly from the substitution of $\vec{v} - (\vec{J}/(n_e e))$ for $\vec{v}_e$ in the energy equation. So does the "work" term, which in section 2.3 has been shown to be vital to total energy conservation, when the diamagnetic pressure term is included in the magnetic field equation.

These corrections can be dropped, as argued in section 2.3, when ion Larmor radius is small compared to plasma scale length a. Specifically, this is to say that the magnitude of the field convection term $\vec{v} \times \vec{B}$ will be much greater than that of $\vec{J} \times \vec{B}/(n_e e)$, or the similarly ordered $\nabla p_e/(n_e e)$ term, when $r_{Li}/a \ll 1$. Although the algebra relating the ratios of the correction terms to $|\vec{v} \times \vec{B}|$, and the ratio r_{Li}/a, of section 2.3 is relatively straightforward, it is somewhat difficult to paint a simple physical picture why this is so. The correction terms can

be regarded as creating additional electric fields ("Ohm's Law" equation C.1) leading to $\vec{E} \times \vec{B}$ drifts, which occur in fluid as well as particle models. The magnitude of an $\vec{E} \times \vec{B}$ drift $v_D = E/B$ [121]. Such drifts are the result of Larmor gyration, but they are not directly proportional to Larmor radius; however, like Larmor radius, they are inversely proportional to B. The drift due to one of these correction terms' electric field will be $v_D = (\nabla p_e/(n_e e))/B$. If such a drift velocity is compared to a characteristic center-of-mass convection velocity (which would appear in the $\vec{v} \times \vec{B}$ term), such as the ion thermal speed v_{th_i}, the ion Larmor radius ordering emerges.

APPENDIX D: SOME DETAILS OF NUMERICS

The component forms, and the integrated spatially differenced fluxes/forces, representing the four "Hall and associated" terms added to the code in Chapter 4, are as follows. These terms are incorporated into the numerical algorithm described in Reference 38, five pages of which are reproduced following this material. Reference 38 describes the code "ANIMAL", which is the predecessor of the MHRDR code developed here; the details reproduced are essentially identical for the two codes.

Hall term :

$$\frac{1}{e\mu_0}\frac{\partial}{\partial\xi_1}\{\frac{B_2}{h_2 n_e}\frac{\partial}{\partial\xi_3}(h_2 B_2)\}$$

$$f_{Hall} = \frac{m_i}{2e\mu_0}\frac{B_{2_k}^{D.C.}(\overline{h_2}_{k+1}\overline{B_2}_{k+1} + \delta(h_2)_{k+1}\delta(B_2)_{k+1} + (\overline{\rho}_k\overline{h_2}_k\overline{zb}_k + \overline{zb}_k\delta(\rho)_k\delta(h_2)_k + -\overline{h_2}_{k-1}\overline{B_2}_{k-1} - \delta(h_2)_{k-1}\delta(B_2)_{k-1})}{+\overline{\rho}_k\delta(h_2)_k\delta(zb)_k + \overline{h_2}_k\delta(\rho)_k\delta(zb)_k)}$$

Diamagnetic pressure term :

$$\frac{1}{e}\frac{\partial}{\partial\xi_1}\{\frac{1}{n_e}\frac{\partial p_e}{\partial\xi_3}\}$$

$$f_{dia.pres.} = \frac{m_i}{2e}\frac{(\overline{p}_{k+1}(\frac{\overline{zb}_{k+1}}{1+\overline{zb}_{k+1}}) - \overline{p}_{k-1}(\frac{\overline{zb}_{k-1}}{1+\overline{zb}_{k-1}}))}{(\overline{p}_k\overline{zb}_k + \delta(\rho)_k\delta(zb)_k)}$$

Electron pressure "work" term :

$$\frac{p_e}{e\mu_0}\frac{\partial}{\partial\xi_1}\{\frac{1}{n_e}\frac{\partial}{\partial\xi_3}(h_2 B_2)\}$$

$$f_{"work"} = \frac{m_i}{4e\mu_0}\overline{\rho}_k\left(\frac{\overline{zb}_k}{1+\overline{zb}_k}\right)\left\{\frac{(h_{2\,j+1,k+1}B_{2\,j+1,k+1} - h_{2\,j+1,k-1}B_{2\,j+1,k-1})}{\rho_{j+1,k}zb_{j+1,k}} + \right.$$

$$\left. - \frac{(h_{2\,j,k+1}B_{2\,j,k+1} - h_{2\,j,k-1}B_{2\,j,k-1})}{\rho_{j,k}zb_{j,k}}\right\}$$

Electron energy convection term : $\frac{1}{e\mu_0}\frac{\partial}{\partial\xi_1}\left\{\frac{\rho\epsilon_e}{n_e}\frac{\partial}{\partial\xi_3}(h_2B_2)\right\}$

$$f_{e.conv.} = \frac{m_i}{2e\mu_0}\rho_k^{D.C.}\epsilon_k^{D.C.}\left(\frac{zb_k^{D.C.}}{1+zb_k^{D.C.}}\right)\frac{(\overline{h_2}_{k+1}\overline{B_2}_{k+1} + \delta(h_2)_{k+1}\delta(B_2)_{k+1} + }{(\overline{\rho}_k\overline{zb}_k + \delta(\rho)_k\delta(zb)_k)}$$

$$-\overline{h_2}_{k-1}\overline{B_2}_{k-1} - \delta(h_2)_{k-1}\delta(B_2)_{k-1})$$

where $\overline{Q_k} = (Q_{j+1,k} + Q_{j,k})/2$, $\delta(Q)_k = (Q_{j+1,k} - Q_{j,k})/2$, and $Q_k^{D.C.}$ is the appropriately selected donor-cell quantity $Q_{j,k}$ or $Q_{j+1,k}$, depending on the direction of $\vec{v}_{convective} = -\vec{J}/n_e e$. The generalized coordinate ξ_1, in the Z-pinch work done here, corresponds to the radial (r) direction (for which j is the index), and ξ_3 to the axial (z) direction (for which k is the index); the second coordinate ξ_2 is the azimuthal (θ) direction, for which the scale factor h_2 is r. The above formulas represent fluxes in the ξ_1 (r) direction; fluxes in the ξ_3 (z) direction can be obtained by replacing ξ_1 with ξ_3 (indices j with k) and multiplying by -1.

An MHD model based on local thermodynamic equilibrium is incorporated into ANIMAL. The basic model equations are

$$\frac{\partial \rho}{\partial t} + \nabla \cdot (\rho \bar{v}) = 0, \tag{1}$$

$$\frac{\partial (\rho \bar{v})}{\partial t} + \nabla \cdot (\rho \bar{v}\, \bar{v}) + \nabla p + \frac{1}{\mu_0} \bar{B} \times (\nabla \times \bar{B}) = 0, \tag{2}$$

$$\frac{\partial (\rho \epsilon)}{\partial t} + \nabla \cdot (\rho \bar{v} \epsilon) + p \nabla \cdot \bar{v} - \nabla \cdot \left[K \nabla T + \frac{T \bar{\beta}}{\mu_0} \times (\nabla \times \bar{B}) \right]$$

$$- (\nabla \times \bar{B}) \left[\frac{\eta}{\mu_0^2} (\nabla \times \bar{B}) - \frac{\bar{\beta}}{\mu_0} \times \nabla T \right] + \dot{\epsilon}_{RAD} = 0, \tag{3}$$

and

$$\frac{\partial \bar{B}}{\partial t} - \nabla \times (\bar{v} \times \bar{B}) + \nabla \times \left[\frac{\eta}{\mu_0} (\nabla \times \bar{B}) - \bar{\beta} \times \nabla T \right] = 0. \tag{4}$$

In Eqs. (1) to (4), ρ is the density, $\bar{v}$ is the fluid velocity, p the pressure, $\bar{B}$ the magnetic field, ϵ the specific internal energy of the fluid, K the thermal conductivity, T the temperature in joules, η the electrical resistivity, $\dot{\epsilon}_{RAD}$ a radiative energy loss, and μ_0 the free-space permeability; mks units are used throughout. Equation (1) is the continuity equation. Equation (2) is the equation of motion; the fourth term is the Lorentz force, $\bar{J} \times \bar{B}$, where the current density $\bar{J}$ has been eliminated through the use of Ampere's law with the usual neglect of displacement current. Equation (3) is the internal energy equation; the fourth term is the divergence of the heat-flow vector and the first part of the next-to-last term represents ohmic heating, ηJ^2. Equation (4) is Faraday's law, based on a simple Ohm's law, $\bar{E} = -\bar{v} \times \bar{B} + \eta \bar{J} - \bar{\beta} \times \nabla T$, where the vector $\bar{\beta}$ is the "transverse" thermoelectric coefficient multiplied by a unit vector in the $\bar{B}$ direction.

For implementation into ANIMAL, the vector-model Eqs. (1) to (4) must be written out into component form. The geometric versatility of ANIMAL is attained by writing the component equations in their general orthogonal, curvilinear coordinate form and making a coordinate transformation from the usual (x_1, x_3, t) two-dimensional coordinate system to a "fixed" coordinate system (ξ_1, ξ_3, t). It is required that the transformation must satisfy $\frac{\partial x_1}{\partial \xi_3} = \frac{\partial x_3}{\partial \xi_1} = 0$. Ignoring the azimuthal component of Eq. (4), the component forms of Eqs. (1) to (4) then become

$$\frac{\partial}{\partial t} (h_1 h_2 h_3 x_{11} x_{33} \rho) + \frac{\partial}{\partial \xi_1} \left(x_{33} h_2 h_3 \rho \left[v_1 - v_1^G \right] \right) + \frac{\partial}{\partial \xi_3} \left(x_{11} h_1 h_2 \rho \left[v_3 - v_3^G \right] \right) = 0, \tag{5}$$

$$\frac{\partial}{\partial t} (h_1 h_2 h_3 x_{11} x_{33} \rho v_1) + \frac{\partial}{\partial \xi_1} \left(x_{33} h_2 h_3 \rho v_1 \left[v_1 - v_1^G \right] \right)$$

$$+ \frac{\partial}{\partial \xi_3} \left(x_{11} h_1 h_2 \rho v_1 \left[v_3 - v_3^G \right] \right) + h_2 \rho v_3 (v_1 h_{13} x_{11} - v_3 h_{31} x_{33})$$

$$+ h_2 h_3 x_{33} \frac{\partial p}{\partial \xi_1} + \frac{1}{\mu_0} h_3 x_{33} B_2 \frac{\partial}{\partial \xi_1} (h_2 B_2) = 0, \tag{6}$$

$$\frac{\partial}{\partial t}\left(h_1 h_2 h_3 x_{11} x_{33}\,\rho v_3\right)+\frac{\partial}{\partial \xi_1}\left(x_{33} h_2 h_3\,\rho v_3\left[v_1-v_1^G\right]\right)$$
$$+\frac{\partial}{\partial \xi_3}\left(x_{11} h_1 h_2\,\rho v_3\left[v_3-v_3^G\right]\right)+h_2\,\rho v_1\left(v_3 h_{31} x_{33}-v_1 h_{13} x_{11}\right)$$
$$+h_1 h_2 x_{11}\frac{\partial p}{\partial \xi_3}+\frac{1}{\mu_0}\,h_1 x_{11} B_2\,\frac{\partial}{\partial \xi_3}\left(h_2 B_2\right)=0, \tag{7}$$

$$\frac{\partial}{\partial t}\left(h_1 h_2 h_3 x_{11} x_{33}\,\rho\epsilon\right)+\frac{\partial}{\partial \xi_1}\left(x_{33} h_2 h_3\,\rho\epsilon\left[v_1-v_1^G\right]\right)$$
$$+\frac{\partial}{\partial \xi_3}\left(x_{11} h_1 h_2\,\rho\epsilon\left[v_3-v_3^G\right]\right)+p\,\frac{\partial}{\partial \xi_1}\left(h_2 h_3 x_{33} v_1\right)$$
$$+p\,\frac{\partial}{\partial \xi_3}\left(h_1 h_2 x_{11} v_3\right)-\frac{\partial}{\partial \xi_1}\left[\frac{h_2 h_3 x_{33}}{h_1 x_{11}}\left(K\,\frac{\partial T}{\partial \xi_1}+\frac{\beta T|B_2|}{\mu_0 h_2 B_2}\,\frac{\partial}{\partial \xi_1}\left[h_2 B_2\right]\right)\right]$$
$$-\frac{\partial}{\partial \xi_3}\left[\frac{h_1 h_2 x_{11}}{h_3 x_{33}}\left(K\,\frac{\partial T}{\partial \xi_3}+\frac{\beta T|B_2|}{\mu_0 h_2 B_2}\,\frac{\partial}{\partial \xi_3}\left[h_2 B_2\right]\right)\right]$$
$$-\frac{h_3 x_{33}}{h_1 h_2 x_{11}\mu_0}\,\frac{\partial}{\partial \xi_1}\left(h_2 B_2\right)\left[\frac{\eta}{\mu_0}\,\frac{\partial}{\partial \xi_1}\left(h_2 B_2\right)+\frac{h_2\beta|B_2|}{B_2}\,\frac{\partial T}{\partial \xi_1}\right]$$
$$-\frac{h_1 x_{11}}{h_3 h_2 x_{33}\mu_0}\,\frac{\partial}{\partial \xi_3}\left(h_2 B_2\right)\left[\frac{\eta}{\mu_0}\,\frac{\partial}{\partial \xi_3}\left(h_2 B_2\right)+\frac{h_2\beta|B_2|}{B_2}\,\frac{\partial T}{\partial \xi_3}\right]$$
$$+\dot{\epsilon}_{RAD}=0, \tag{8}$$

and

$$\frac{\partial}{\partial t}\left(h_1 h_3 x_{11} x_{33} B_2\right)+\frac{\partial}{\partial \xi_1}\left[h_3 x_{33} B_2\left(v_1-v_1^G\right)\right]+\frac{\partial}{\partial \xi_3}\left[h_1 x_{11} B_2\left(v_3-v_3^G\right)\right]$$
$$-\frac{\partial}{\partial \xi_3}\left[\frac{h_1 x_{11}}{h_3 x_{33}}\left(\frac{\eta}{\mu_0 h_2}\,\frac{\partial}{\partial \xi_3}\left(h_2 B_2\right)+\beta\,\frac{|B_2|}{B_2}\,\frac{\partial T}{\partial \xi_3}\right)\right]$$
$$-\frac{\partial}{\partial \xi_1}\left[\frac{h_3 x_{33}}{h_1 x_{11}}\left(\frac{\eta}{\mu_0 h_2}\,\frac{\partial}{\partial \xi_1}\left(h_2 B_2\right)+\beta\,\frac{|B_2|}{B_2}\,\frac{\partial T}{\partial \xi_1}\right)\right]=0. \tag{9}$$

In Eqs. (5) to (9), the definitions $x_{11}=\frac{\partial x_1}{\partial \xi_1}$, $x_{33}=\frac{\partial x_3}{\partial \xi_3}$, $h_{13}=\frac{\partial h_1}{\partial \xi_3}$, $h_{31}=\frac{\partial h_3}{\partial \xi_1}$, $v_1^G=h_1\frac{\partial x_1}{\partial t}$, and $v_3^G=h_3\frac{\partial x_3}{\partial t}$ have been introduced for convenience. The notations v_1 and v_3 refer to the velocity components in the ξ_1 and ξ_3 direction, respectively, and B_2 is the component of magnetic field normal to the ξ_1–ξ_3 plane.

The component Eqs. (5) to (9) are written essentially in the form in which they are differenced. It is very important to note that only first and second spatial derivatives of the dependent variables ρ, v_1, v_3, ϵ, and B_2 are present and that mixed derivatives of the form $\frac{\partial^2}{\partial \xi_1 \partial \xi_3}$ do not appear. Any additional Braginskii[24] physics effects not included in Eqs. (1) to (4) generally involve the mixed second derivative.

The component Eqs. (5) to (9) can be written in the form

$$\frac{\partial \bar{T}(\bar{U})}{\partial T} + \bar{X}\left(\bar{U}, \frac{\partial}{\partial \xi_1}\right) + \bar{Y}\left(\bar{U}, \frac{\partial}{\partial \xi_3}\right) = 0, \tag{17}$$

where $\bar{X}$, $\bar{Y}$, $\bar{T}$, and $\bar{U}$ are five component vectors, and

$$\bar{U} = (\rho, v_1, v_3, \epsilon, B_2). \tag{18}$$

Only derivatives with respect to one orthogonal coordinate ξ_1 appear in $\bar{X}$ and only derivatives with respect to the second coordinate ξ_3 appear in $\bar{Y}$. The two alternately used finite-difference equations in ANIMAL can be considered to have the form

$$\frac{\bar{T}\left(\bar{U}^{n+1}_{j,k}\right) - \bar{T}\left(\bar{U}^{n}_{j,k}\right)}{t^{n+1} - t^{n}} + \tilde{\bar{X}}\left[\left(\bar{U}^{n+1}_{j-1,k}\right), \left(\bar{U}^{n+1}_{j,k}\right), \left(\bar{U}^{n+1}_{j+1,k}\right)\right] + \tilde{\bar{Y}}\left[\left(\bar{U}^{n}_{j,k-1}\right), \left(\bar{U}^{n}_{j,k}\right), \left(\bar{U}^{n}_{j,k+1}\right)\right] = 0 \tag{19}$$

$$\frac{\bar{T}\left(\bar{U}^{n+2}_{j,k}\right) - T\left(\bar{U}^{n+1}_{j,k}\right)}{t^{n+2} - t^{n+1}} + \tilde{\bar{X}}\left[\left(\bar{U}^{n+1}_{j-1,k}\right), \left(\bar{U}^{n+1}_{j,k}\right), \left(\bar{U}^{n+1}_{j+1,k}\right)\right] + \tilde{\bar{Y}}\left[\left(\bar{U}^{n+2}_{j,k-1}\right), \left(\bar{U}^{n+2}_{j,k}\right), \left(\bar{U}^{n+2}_{j,k+1}\right)\right] = 0 \quad , \tag{20}$$

where $\bar{U}^{n}_{j,k}$ designates values at time t^n and spatial coordinates $(\xi_1)_j$, $(\xi_3)_k$. In Eqs. (19) and (20), $\tilde{\bar{X}}$ and $\tilde{\bar{Y}}$ are spatial finite-difference approximations to $\bar{X}$ and $\bar{Y}$, respectively. Equations (19) and (20) show the standard ADI coupling between unknown quantities. In Eq. (19), which is used to advance the calculations from t^n to t^{n+1}, the unknowns are the values $\bar{U}^{n+1}_{j,k}$ along a line of constant k; the quantities at $k+1$ and $k-1$ are known quantities since they have the superscript n. In Eq. (20), which is used to advance the calculations from t^{n+1} to t^{n+2}, the unknowns are the values $U^{n+2}_{j,k}$ along a line of constant j; the quantities at $j+1$ and $j-1$ are known quantities since they have the superscript $n+1$. Equations (19) and (20) are in general nonlinear functions of the unknown quantities and therefore cannot be solved directly. To solve Eqs. (19) and (20), ANIMAL uses essentially a Newton-Raphson method as given by Pennington,[28] among others. Application of the Newton-Raphson method to Eq. (19) gives an equation of the form

$$(\bar{\bar{A}}_1)^{n+1,\ell}_{j,k} \cdot \bar{U}^{n+1,\ell+1}_{j,k} + (\bar{\bar{B}}_1)^{n+1,\ell}_{j,k} \cdot \bar{U}^{n+1,\ell+1}_{j+1,k} + (\bar{\bar{C}}_1)^{n+1,\ell}_{j,k} \cdot \bar{U}^{n+1,\ell+1}_{j-1,k} = (\bar{V}_1)^{n+1,\ell}_{j,k}, \tag{21}$$

where the additional superscripts ℓ and $\ell+1$ indicate the iteration number and where $\bar{\bar{A}}$, $\bar{\bar{B}}$, and $\bar{\bar{C}}$ are matrices.

The calculations reported by Lindemuth and Killeen[17] can be considered as using Eq. (21) for $\ell = 0$ only. As shown by Lindemuth and Killeen, Eq. (21) for $\ell = 0$ gives an approximation formally second-order accurate with respect to the timestep $\Delta t = t^{n+1} - t^n$. Repeated application of Eq. (21) until convergence is achieved does not increase the formal accuracy of the solution, and Eqs. (19) and (20) are, when used together, still of second-order accuracy with respect to the timestep. However, the basic reason for the success of ADI is that the errors introduced on one timestep are cancelled on the following timestep. This apparently requires the two approximations to the $\bar{X}$ of Eq. (17) to have the same values, as indicated in Eqs. (19) and (20). If Eq. (21) is not iterated to some sort of convergence, the net effect is to use a somewhat different value for $\bar{X}$ in (20) than is used in (19). Experience during the code development process has shown that failure to iterate introduces unwanted, nonphysical effects that affect the calculations unless the timestep is reduced considerably.

Note that Eq. (19) or (20), considered alone, is an approximation to the complete physical system, Eq. (17). ANIMAL, as its predecessor,[17] does not use fractional timestep or splitting procedures, whereby one physical process—or one dimension—is treated as if the others were not present. Experience during code development has shown instances where the coupling between physical processes or dimensions was sufficiently strong that a fractional timestep method would have required a considerably reduced timestep to maintain accuracy. For example, situations have been observed where the energy increase due to Ohmic heating was balanced by the heat loss due to thermal conduction, so that no net change occurred, and yet either process by itself would have led to a drastic change in the net energy.

Equation (21) is appropriate only when $1 < j < J$ and $1 < k < K$. ANIMAL casts boundary conditions in the form

$$\bar{U}_{1,k}^{n+1,\ell+1} = (\bar{\bar{E}}_1)_{1,k}^{n+1,\ell} \cdot \bar{U}_{2,k}^{n+1,\ell+1} + (\bar{\bar{H}}_1)_{1,k}^{n+1,\ell} \cdot \bar{U}_{3,k}^{n+1,\ell+1} + (\bar{F}_1)_{1,k}^{n+1,\ell} \quad , \tag{22}$$

$$\bar{U}_{J,k}^{n+1,\ell+1} = (\bar{\bar{E}}_1)_{J,k}^{n+1,\ell} \cdot \bar{U}_{J-1,k}^{n+1,\ell+1} + (\bar{\bar{H}}_1)_{J,k}^{n+1,\ell} \cdot \bar{U}_{J-2,k}^{n+1,\ell+1} + (\bar{F}_1)_{J,k}^{n+1,\ell} \, , \tag{23}$$

$$\bar{U}_{j,1}^{n+1,\ell+1} = (\bar{\bar{E}}_3)_{j,1}^{n+1,\ell} \cdot \bar{U}_{j,2}^{n+1,\ell+1} + (\bar{\bar{H}}_3)_{j,1}^{n+1,\ell} \cdot \bar{U}_{j,3}^{n+1,\ell+1} + (\bar{F}_3)_{j,1}^{n+1,\ell} \, , \tag{24}$$

and

$$\bar{U}_{j,K}^{n+1,\ell+1} = (\bar{\bar{E}}_3)_{j,K}^{n+1,\ell} \cdot \bar{U}_{j,K-1}^{n+1,\ell+1} + (\bar{\bar{H}}_3)_{j,K}^{n+1,\ell} \cdot \bar{U}_{j,K-2}^{n+1,\ell+1} + (\bar{F}_3)_{j,K}^{n+1,\ell} \, . \tag{25}$$

Equations (21) to (23) form a set of linear, simultaneous, "tridiagonal" algebraic equations in the unknown quantities $\bar{U}_{j,k}^{n+1,\ell+1}$ for $1 \leq j \leq J$ along a line of constant k, $1 < k < K$. The method of solution involves calculating $\bar{E}$'s and $\bar{F}$'s such that

$$\bar{U}_{j,k}^{n+1,\ell+1} = \bar{\bar{E}}_{j,k}^{n+1,\ell} \cdot \bar{U}_{j+1,k}^{n+1,\ell+1} + \bar{F}_{j,k}^{n+1,\ell} \, . \tag{26}$$

Substitution of Eq. (26) into Eq. (21) leads to the result that

$$\bar{\bar{E}}_{2,k}^{n+1,\ell} = -\left[(\bar{\bar{A}}_1)_{2,k}^{n+1,\ell} + (\bar{\bar{C}}_1)_{2,k}^{n+1,\ell} \cdot (\bar{\bar{E}}_1)_{1,k}^{n+1,\ell} \right]^{-1} \cdot \left[(\bar{\bar{B}}_1)_{2,k}^{n+1,\ell} + (\bar{\bar{C}}_1)_{2,k}^{n+1,\ell} \cdot (\bar{\bar{H}}_1)_{1,k}^{n+1,\ell} \right] , \tag{27}$$

$$\bar{F}_{2,k}^{n+1,\ell} = \left[(\bar{\bar{A}}_1)_{2,k}^{n+1,\ell} + (\bar{\bar{C}}_1)_{2,k}^{n+1,\ell} \cdot (\bar{\bar{E}}_1)_{1,k}^{n+1,\ell} \right]^{-1} \cdot \left[(\bar{V}_1)_{2,k}^{n+1,\ell} - (\bar{\bar{C}}_1)_{2,k}^{n+1,\ell} \cdot (\bar{F}_1)_{1,k}^{n+1,\ell} \right] , \tag{28}$$

$$\bar{\bar{E}}_{j,k}^{n+1,\ell} = -\left[(\bar{\bar{A}}_1)_{j,k}^{n+1,\ell} + (\bar{\bar{C}}_1)_{j,k}^{n+1,\ell} \cdot \bar{\bar{E}}_{j-1,k}^{n+1,\ell} \right]^{-1} \cdot (\bar{\bar{B}})_{j,k}^{n+1,\ell} \, , \quad 2 < j < J \, , \tag{29}$$

and

$$\bar{F}_{j,k}^{n+1,\ell} = \left[(\bar{\bar{A}}_1)_{j,k}^{n+1,\ell} + (\bar{\bar{C}}_1)_{j,k}^{n+1,\ell} \cdot \bar{\bar{E}}_{j-1,k}^{n+1,\ell} \right]^{-1} \cdot \left[(\bar{V}_1)_{j,k}^{n+1,\ell} - (\bar{\bar{C}}_1)_{j,k}^{n+1,\ell} \cdot \bar{F}_{j-1,k}^{n+1,\ell} \right] , \quad 2 < j < J \, . \tag{30}$$

Using Eqs. (29) and (30) for J−1 and J−2 in Eq. (26) and substituting into Eq. (23) leads to

$$\bar{U}_{J,k}^{n+1,\ell+1} = \left\{ \bar{\bar{I}} - \left[(\bar{\bar{E}}_1)_{J,k}^{n+1,\ell} + (\bar{\bar{H}}_1)_{J,k}^{n+1,\ell} \cdot \bar{\bar{E}}_{J-2,k}^{n+1,\ell} \right] \cdot \bar{\bar{E}}_{J-1,k}^{n+1,\ell} \right\}^{-1} \cdot$$

$$\left\{ (\bar{F}_1)_{J,k}^{n+1,\ell} + \left[(\bar{\bar{H}}_1)_{J,k}^{n+1,\ell} \cdot \bar{\bar{E}}_{J-2,k}^{n+1,\ell} + (\bar{E}_1)_{J,k}^{n+1,\ell} \right] \cdot \bar{F}_{J-1,k}^{n+1,\ell} \right.$$

$$\left. + (\bar{\bar{H}}_1)_{j,k}^{n+1,\ell} \cdot \bar{F}_{J-2,k}^{n+1,\ell} \right\} . \qquad (31)$$

Thus the solution procedure along a line of constant k is to set and store the boundary condition Eq. (22), calculate $\bar{\bar{A}}$, $\bar{\bar{B}}$, $\bar{\bar{C}}$, and $\bar{V}$ of Eq. (21) for j = 2, calculate and store $\bar{\bar{E}}_2$ and $\bar{F}_2$ from Eqs. (27) and (28), repetitively calculate $\bar{\bar{A}}$, $\bar{\bar{B}}$, $\bar{\bar{C}}$, and $\bar{V}$ of Eq. (21), and calculate and store the $\bar{\bar{E}}$'s and $\bar{F}$'s of Eqs. (29) and (30) for $2 < j < J$. $\bar{U}_j$ is then calculated from Eq. (31) and all other $\bar{U}_j$'s are calculated in decreasing order of j from Eq. (26). Note that it is not necessary to store $\bar{\bar{A}}$, $\bar{\bar{B}}$, $\bar{\bar{C}}$, and $\bar{V}$ for each j as long as the boundary conditions have the form given in Eqs. (22) and (23). Also, note that each k line is computed independently.

Equations (21) to (31), as a method of solving Eq. (19), give the basic ANIMAL algorithm for advancing the calculations from time t^n to t^{n+1}. The algorithm begins by setting $\bar{U}_{j,k}^{n+1,0} = \bar{U}_{j,k}^{n}$. Then for k = 2 (or K−1) Eqs. (21) to (31) are applied repetitively until $\left| \left(\bar{U}_{j,k}^{n+1,\ell+1} - \bar{U}_{j,k}^{n+1,\ell} \right) / \bar{U}_{j,k}^{n+1,\ell} \right| < \delta$, where δ is typically 5×10^{-4}. Then each successive k is advanced similarly. When all k such that $2 \leq k \leq K-1$ have been advanced, the boundary conditions Eqs. (24) and (25) are used to set values at k = 1 and k = K.

To advance the calculation from time t^{n+1} to t^{n+2}, the Newton-Raphson method is applied to Eq. (20). Boundary conditions have the same form as in Eqs. (22) to (24), with the superscript n+1 replaced by n+2. The equations corresponding to Eqs. (21) and (26) are

$$(\bar{\bar{A}}_3)_{j,k}^{n+2,\ell} \cdot \bar{U}_{j,k}^{n+2,\ell+1} + (\bar{\bar{B}}_3)_{j,k}^{n+2,\ell} \cdot \bar{U}_{j,k+1}^{n+2,\ell+1} + (\bar{\bar{C}}_3)_{j,k}^{n+2,\ell} \cdot \bar{U}_{j,k-1}^{n+2,\ell+1} = (\bar{V}_3)_{j,k}^{n+2,\ell} \qquad (32)$$

and

$$\bar{U}_{j,k}^{n+2,\ell+1} = \bar{\bar{E}}_{j,k}^{n+2,\ell} \cdot \bar{U}_{j,k+1}^{n+2,\ell+1} + \bar{F}_{j,k}^{n+2,\ell} , \qquad (33)$$

respectively. The derivation of expressions for $\bar{\bar{E}}_{j,2}^{n+2,\ell}$, $\bar{F}_{j,2}^{n+2,\ell}$, $\bar{\bar{E}}_{j,k}^{n+2,\ell}$, $F_{j,k}^{n+2,\ell}$, $\bar{U}_{j,K}^{n+2,\ell}$ corresponding to Eqs. (27) to (31) is straightforward. Thus, the algorithms for solving both Eqs. (19) and (20) are identical except for the method of establishing the coefficients $\bar{\bar{E}}$, $\bar{\bar{H}}$, and $\bar{F}$ of Eqs. (22) to (25) and the coefficients $\bar{\bar{A}}$, $\bar{\bar{B}}$, $\bar{\bar{C}}$, and $\bar{V}$ of Eqs. (21) and (32). (Rigorously speaking, $\bar{F}$ and $\bar{V}$ are not "coefficients.") The only other difference in the two algorithms is where the computed results, Eqs. (26) and (33), are stored. The similarity in the two algorithms is used to minimize the coding in ANIMAL.

As formulated by Eqs. (19) to (33), ANIMAL's basic algorithm is quite general and need not be restricted to a five-component solution vector $\bar{U}$ as indicated in Eq. (18). ANIMAL is in fact set up to calculate subsets of the model equations. The following subsets can be selected in addition to Eq. (18):

(1) $\bar{U} = (\rho, \epsilon, B)$ in one-dimension, i.e., one-dimensional diffusive transport.
(2) $\bar{U} = (\rho, \epsilon, B)$ in two dimensions.
(3) $U = (\rho, v_1, \epsilon)$, i.e., one-dimensional hydrodynamics.
(4) $\bar{U} = (\rho, v_1, v_3, \epsilon)$, i.e., two-dimensional hydrodynamics.
(5) $\bar{U} = (\rho, v_1, \epsilon, B_2)$, i.e., one-dimensional MHD.

For Eq. (18) and each of the subsets a variety of physics options are available; e.g., $\bar{U} = (\rho, v_1, \epsilon)$ can be ideal one-dimensional hydrodynamics if the thermal conductivity and radiation are set to zero. In addition, because of the generality, the ANIMAL algorithm is set up to handle as many as ten variables in anticipation of the addition of more dependent variables. For example, most of the structure to handle additional magnetic field components B_1 and B_3 is already in the code (ANIMAL's predecessor[17] did in fact calculate B_1 and B_3); what is missing is merely coding to determine the appropriate coefficients, and this would be a relatively minor fraction of the entire coding.

It is important to note that for the one-dimensional subsets, $\tilde{Y}$ of Eqs. (19) and (20) are identically zero. Hence, in one-dimensional calculations, ANIMAL uses a fully *implicit* method [Eq. (19)] to advance from t^n to t^{n+1} and then ANIMAL uses a fully *explicit* method [Eq. (20)] to advance from t^{n+1} to t^{n+2}. By combining Eqs. (19) and (20), one can see that the one-dimensional difference equations relating U^{n+2} to U^n, for n even, appear to be Crank-Nicholson,[2] whereas those relating U^{n+3} to U^{n+1} appear to be "leapfrog."[2]

FIGURES:

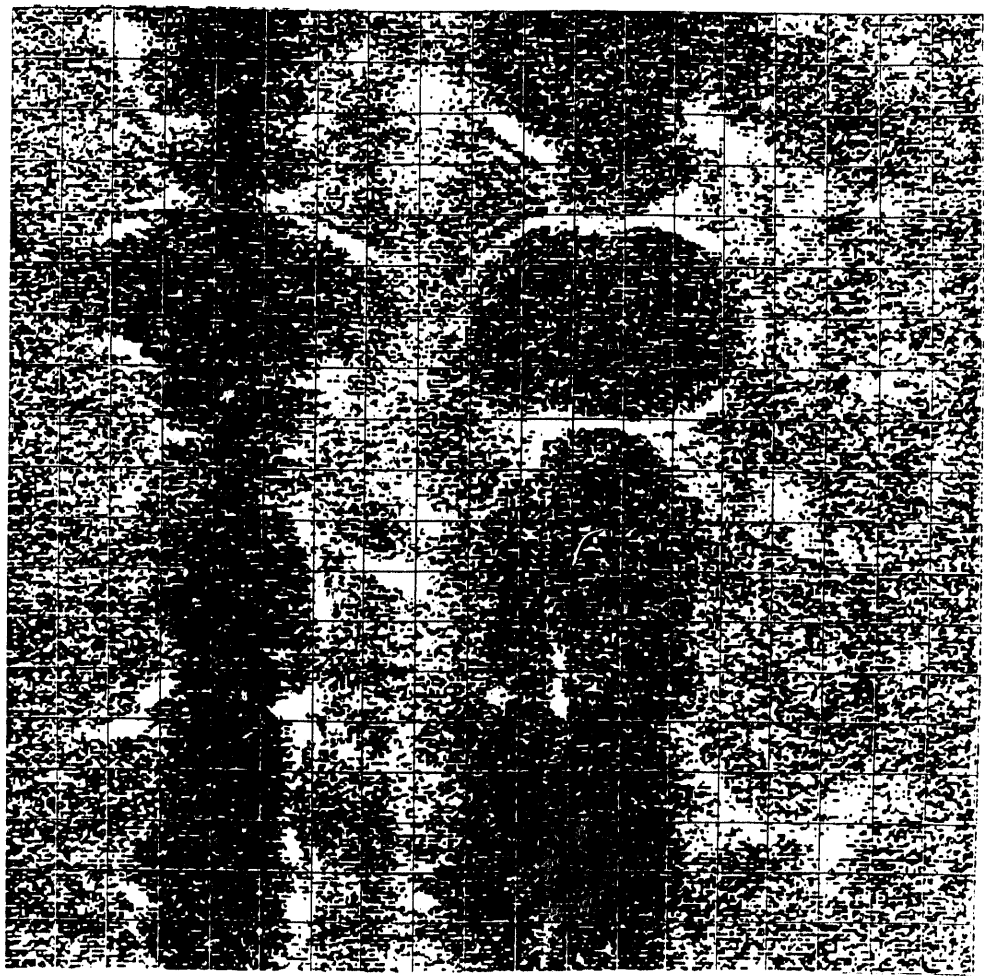

Figs. 1(a-d): Shadowgrams and simulation results, HDZP-I (early): (1a) Experimental shadowgrams, HDZP-I, shot 3863: left-hand image, ~30 nsec (~50 kA); right-hand image, ~40 nsec (~65 kA); each grid block is 0.1 mm square.

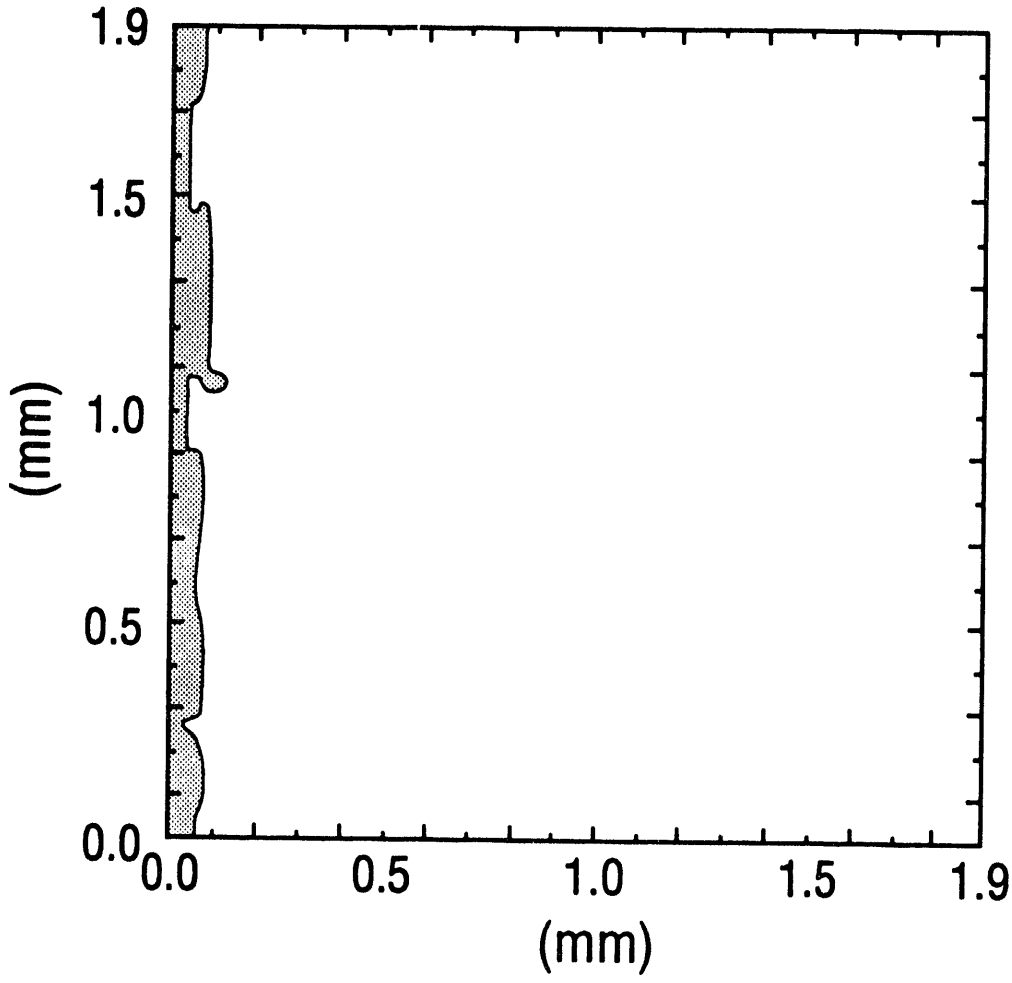

Fig. 1b: Simulation shadowgram from section of same size as 1a, HDZP-I, 30 nsec (50 kA).

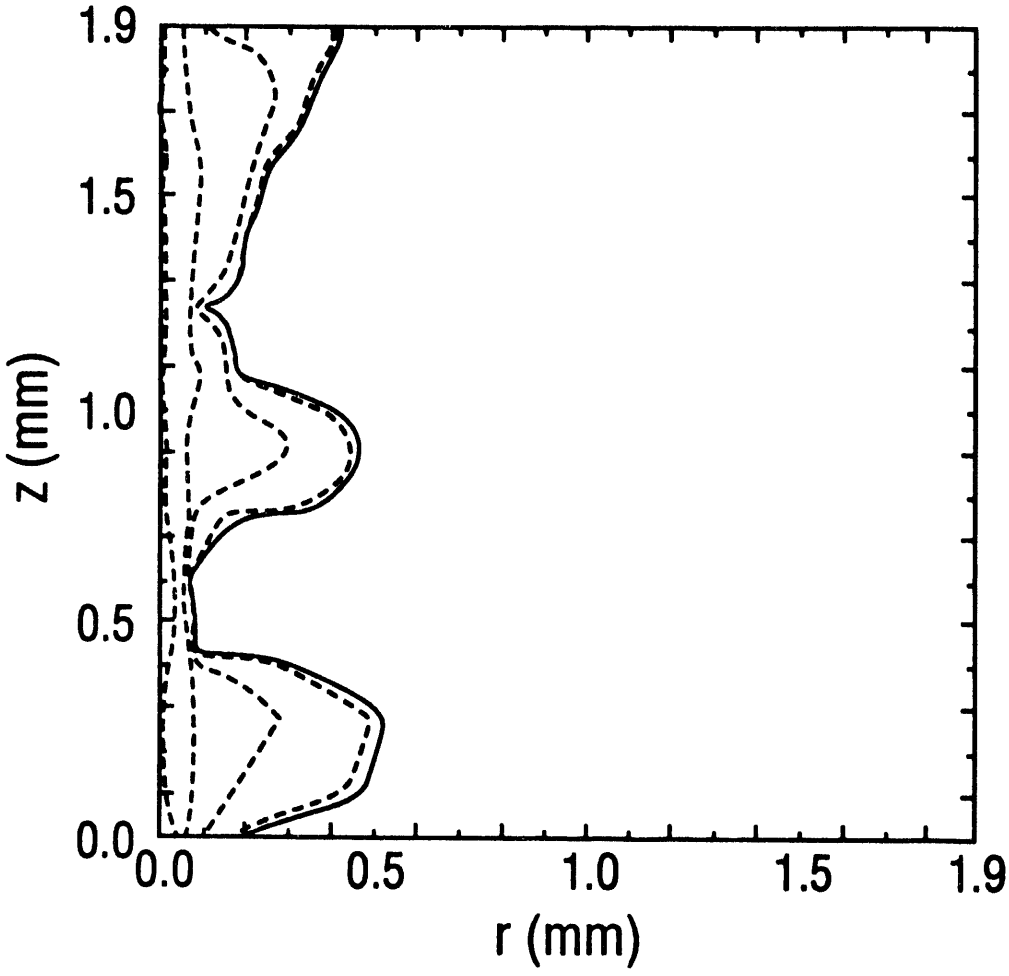

Fig. 1c: Corresponding simulation density contours, 30 nsec (50 kA); right-most solid contour (0.01 kg/m^3) contains 95% of the total mass; dotted contours, from right: 0.012, 0.036, 0.23, 1.3 kg/m^3.

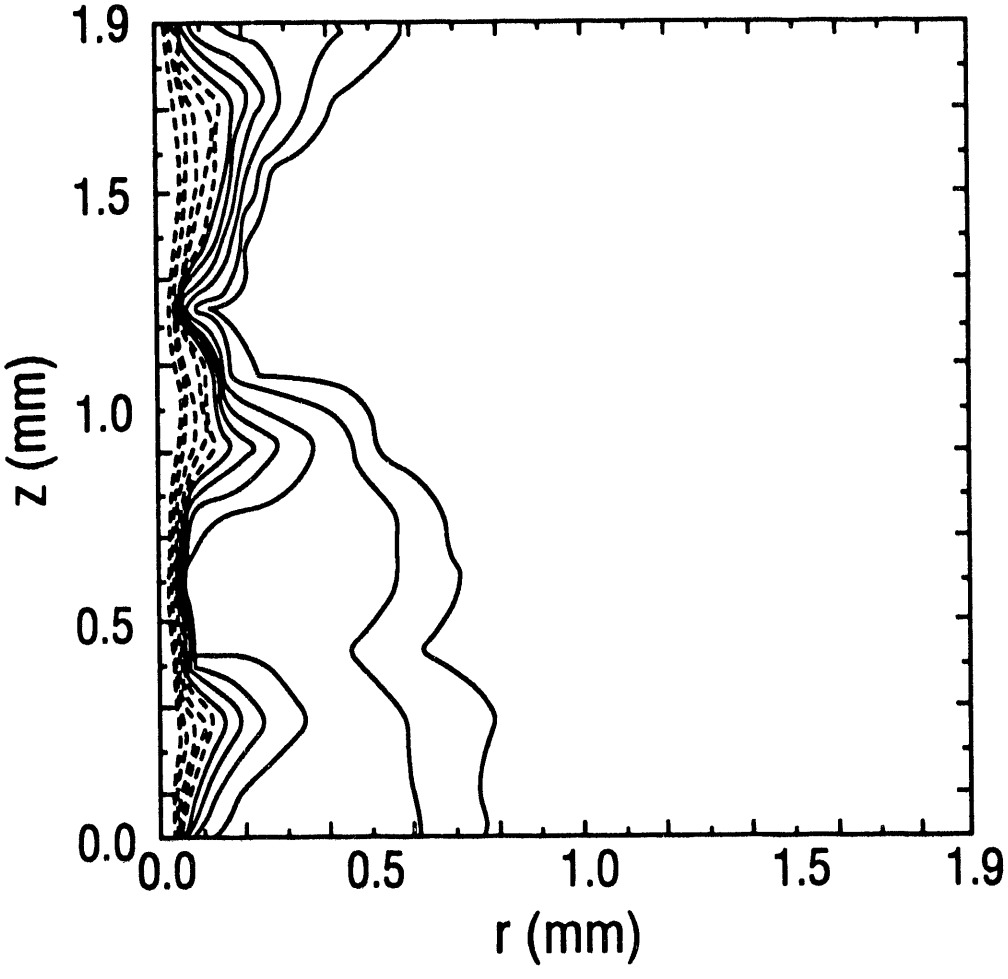

Fig. 1d: Simulation axial current contours, 30 nsec (50 kA); right-most solid contour (48 kA) contains 95% of the total axial current; right-most dotted contour: 20 kA.

Figs. 2(a-b): Shadowgrams, HDZP-I (late): (2a) Experimental shadowgrams, HDZP-I, shots 3876,7: left-hand image (3876), ~65 nsec (~120 kA); right-hand image (7), ~80 nsec (~150 kA); each grid block is 0.1 mm square.

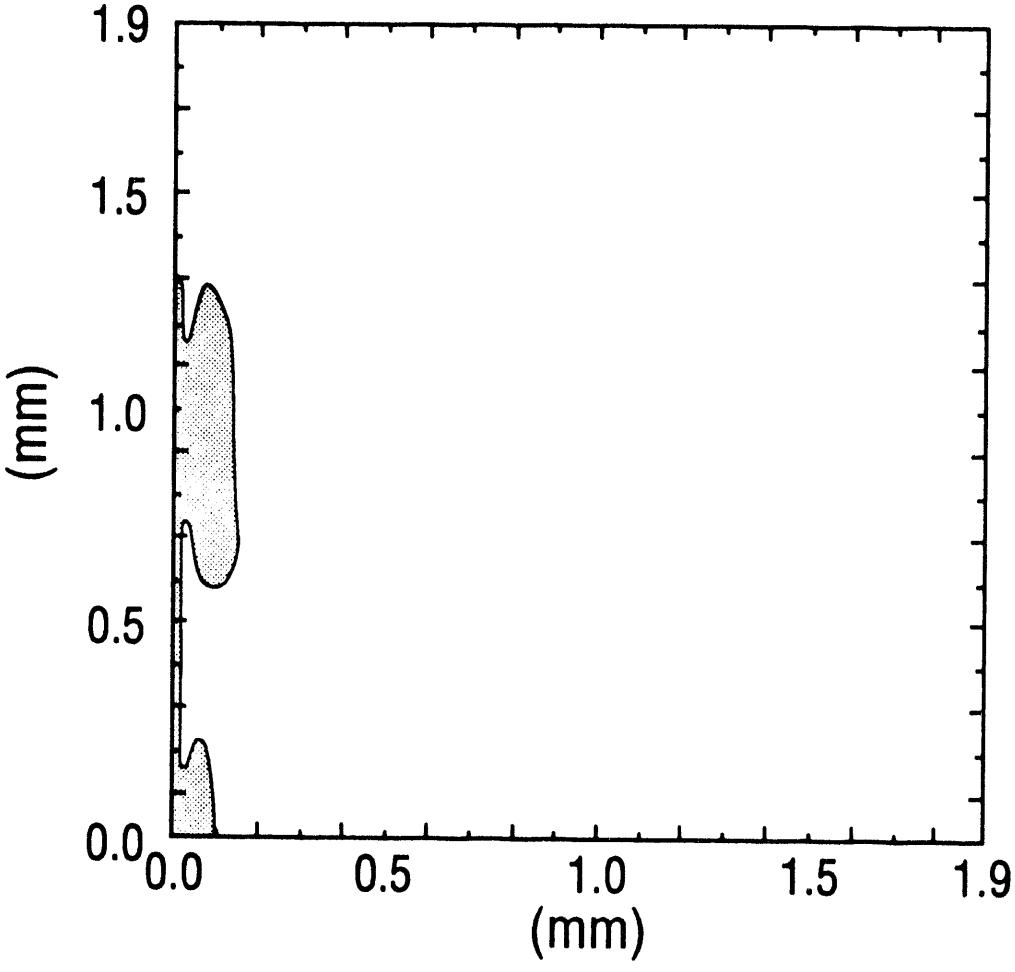

Fig. 2b: Simulation shadowgram, HDZP-I, 65 nsec (120 kA).

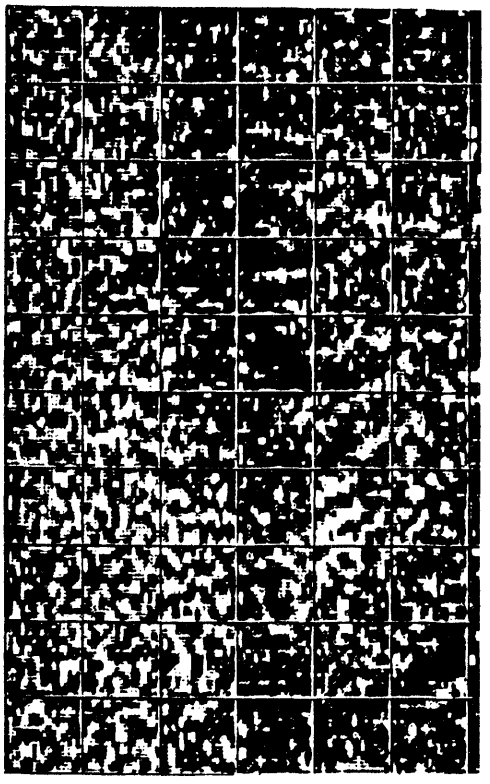

Figs. 3(a-b): Shadowgrams, HDZP-II: (3a) Experimental shadowgram, HDZP-II, shot 194, ~5 nsec (~50 kA); each grid block is 0.25 mm square.

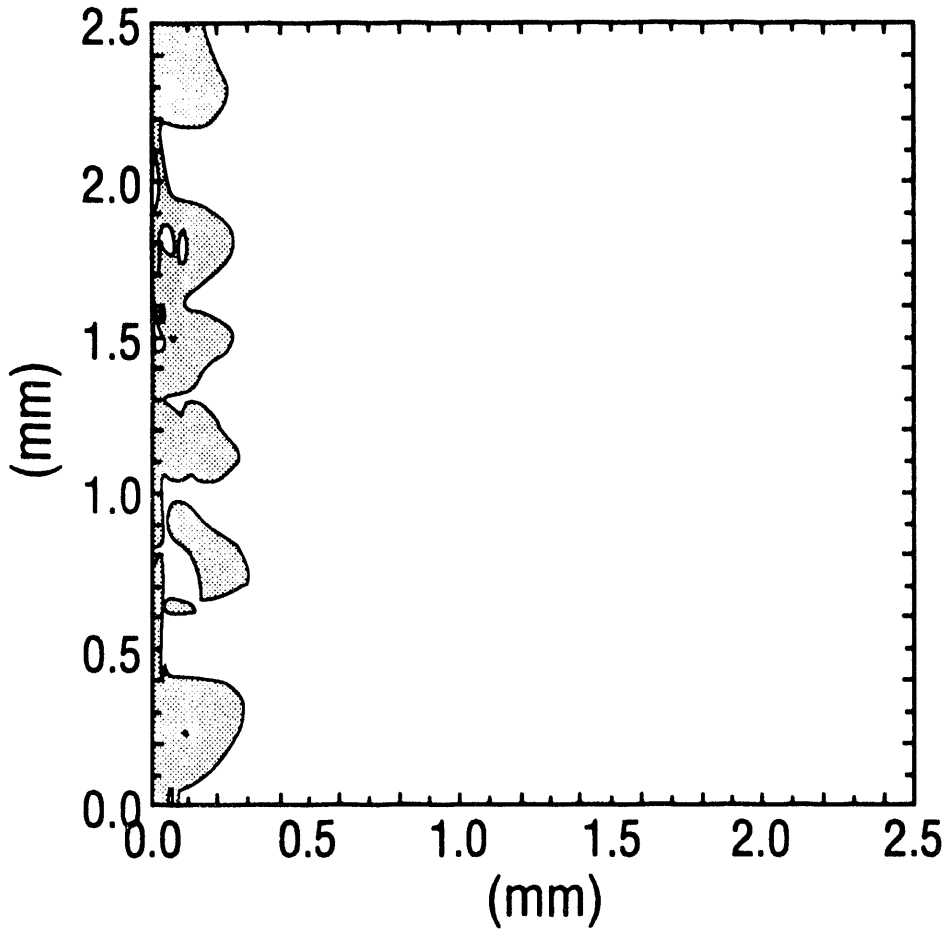

Fig. 3b: Simulation shadowgram, HDZP-II, 12 nsec (160 kA in 1.2 MA ramp).

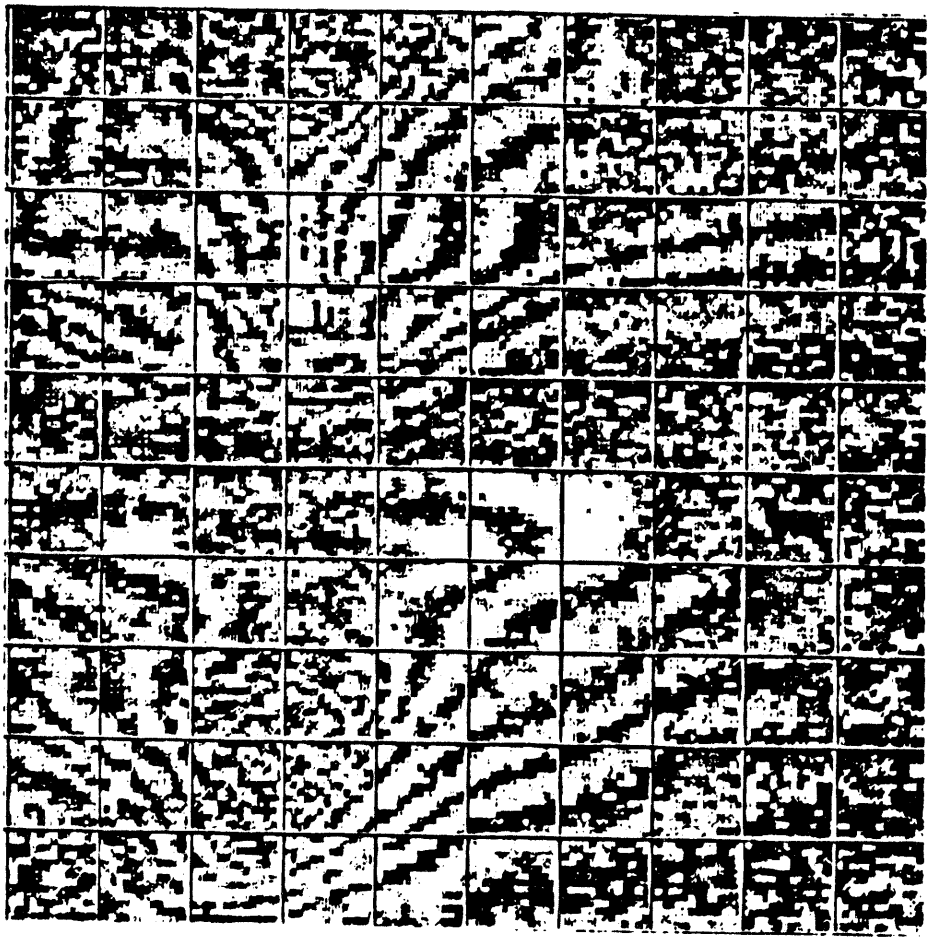

Figs. 4(a-e): Interferograms and simulation results, HDZP-I and -II: (4a) Experimental interferogram, HDZP-II, shot 205, ~20 nsec (~200 kA); each grid block is 0.25 mm square.

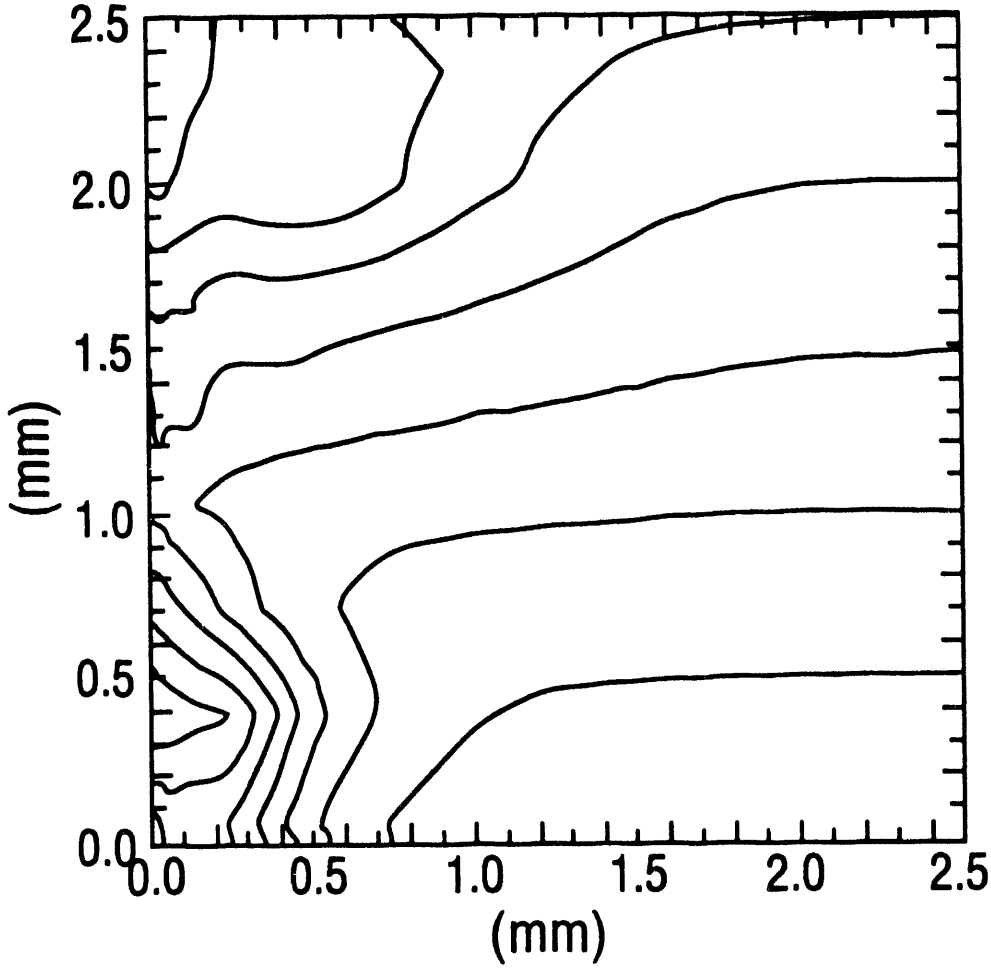

Fig. 4b: Simulation interferogram, HDZP-II, 32 nsec (230 kA).

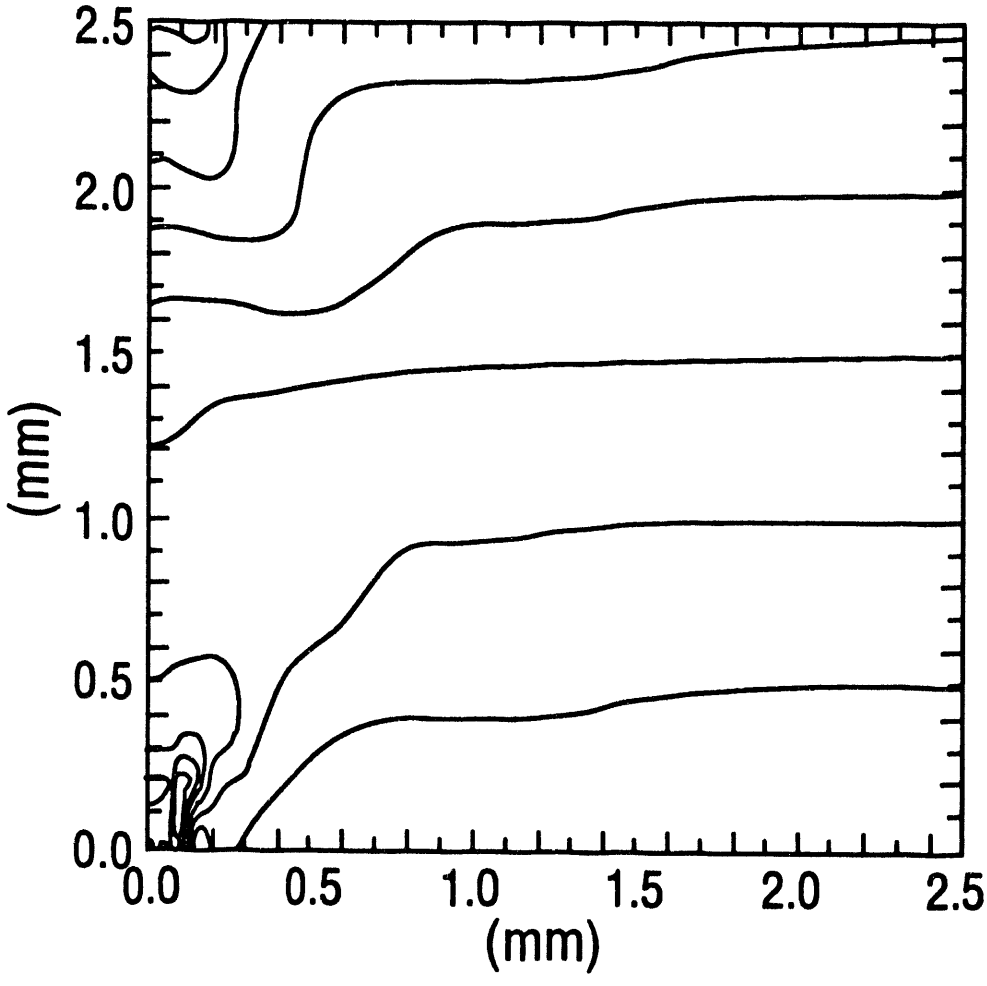

Fig. 4c: Simulation interferogram, HDZP-I, 50 nsec (85 kA).

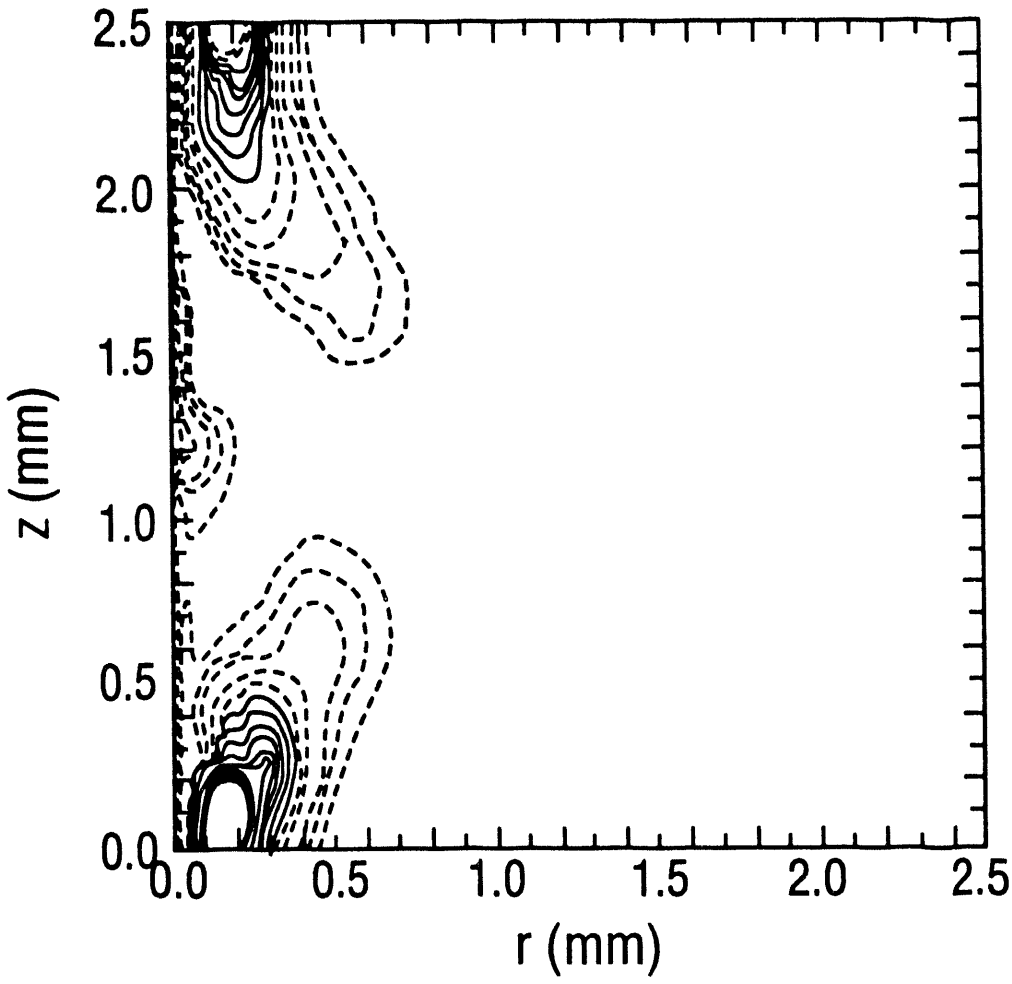

Fig. 4d: Corresponding simulation density contours, HDZP-I, 50 nsec (85 kA); right-most dotted contour: 0.007 kg/m^3; right-most solid contour: 0.033 kg/m^3.

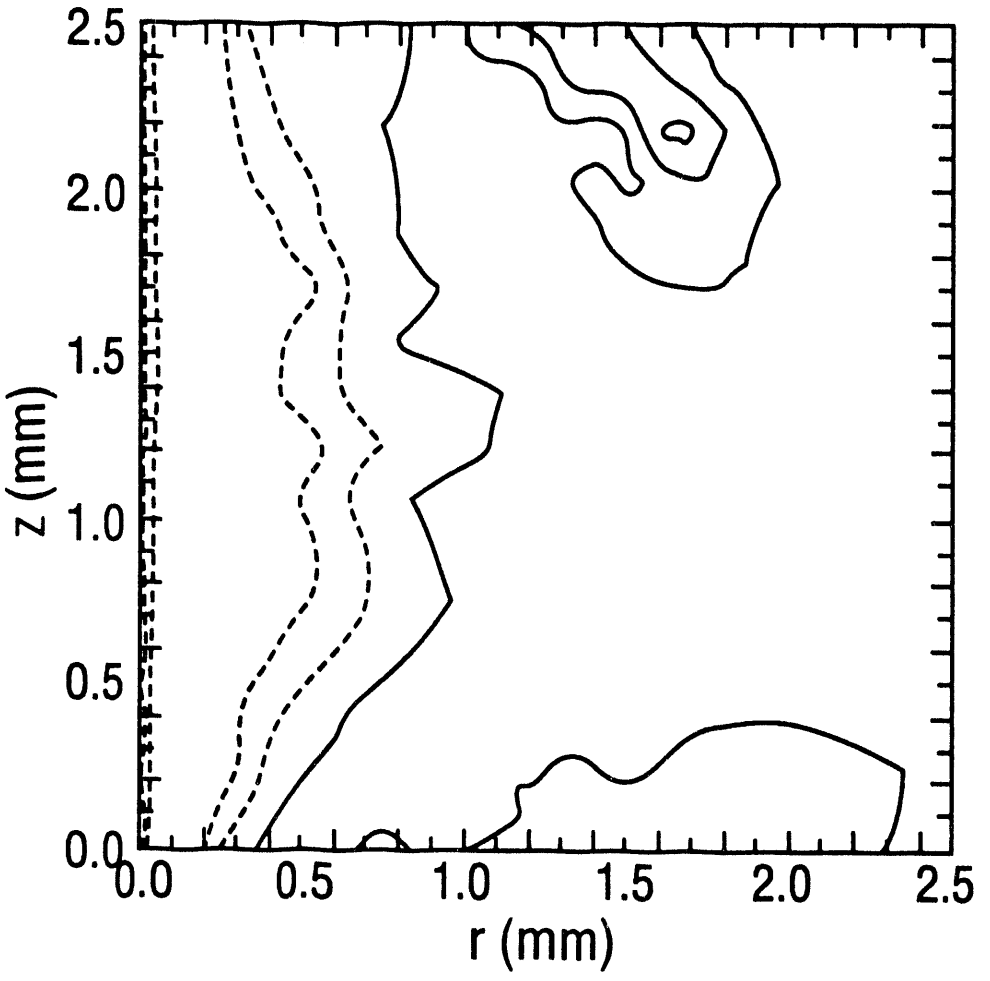

Fig. 4e: Simulation axial current contours, HDZP-I, 50 nsec (85 kA); left-most solid contour: 75 kA; dotted contours, from right: 60, 45, 30 kA.

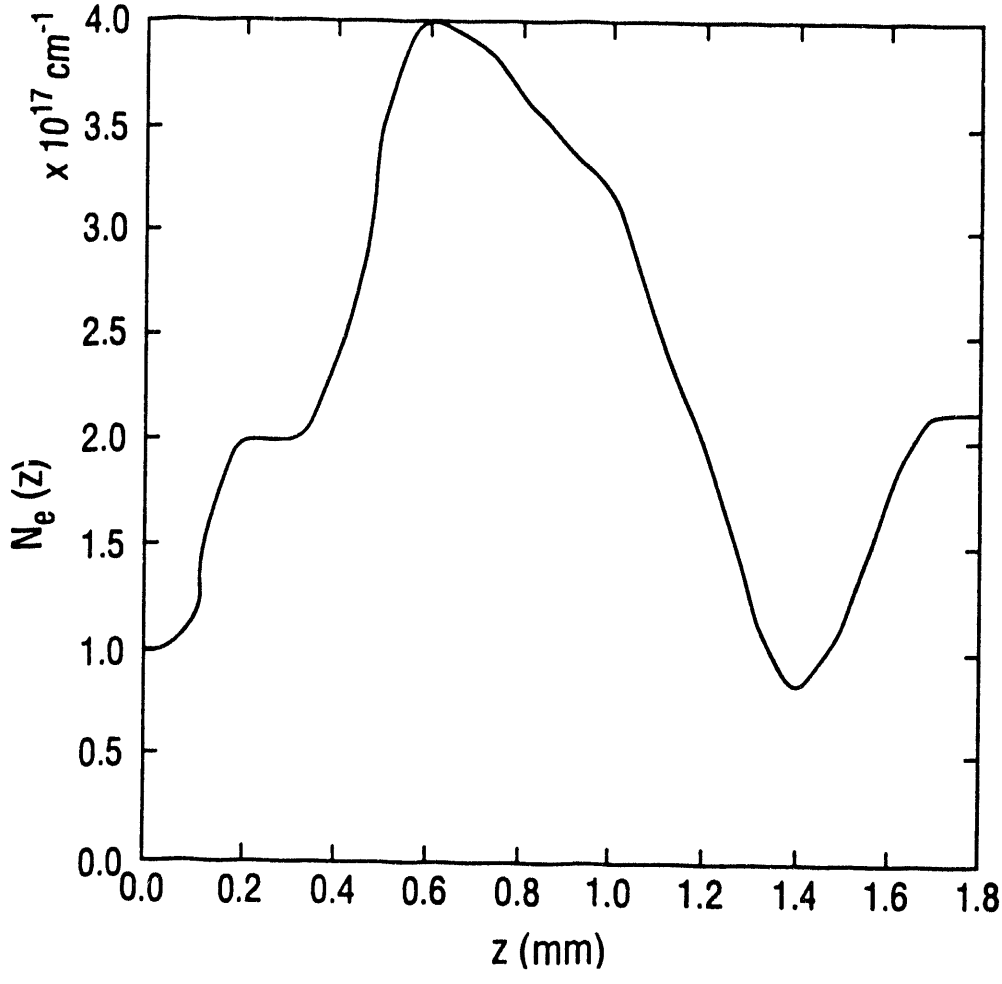

Figs. 5(a-c): Line density vs, axial location: (5a) Experimentally computed total line density vs. axial location, HDZP-II, shot 205, ~20 nsec (~200 kA).

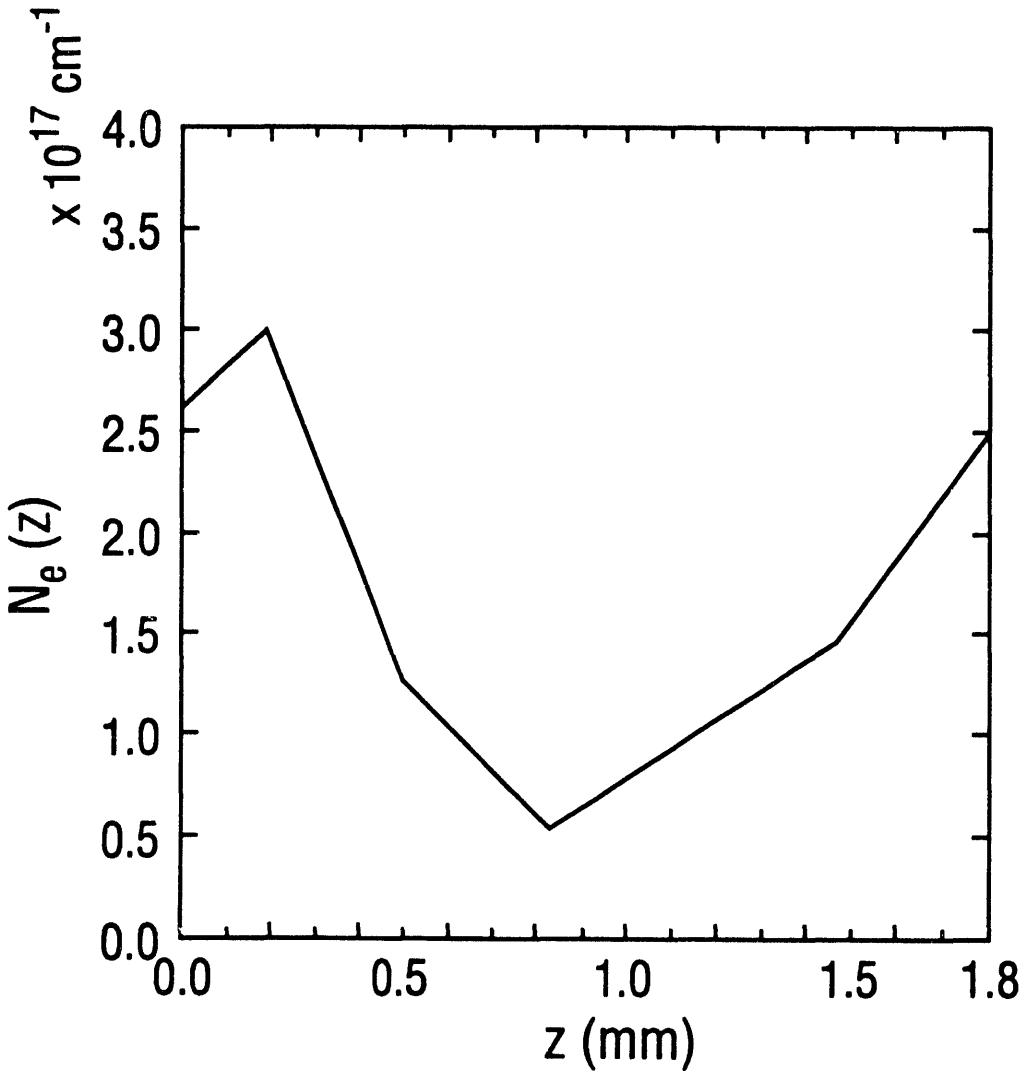

Fig. 5b: Simulation line density, HDZP-II, 32 nsec (230 kA).

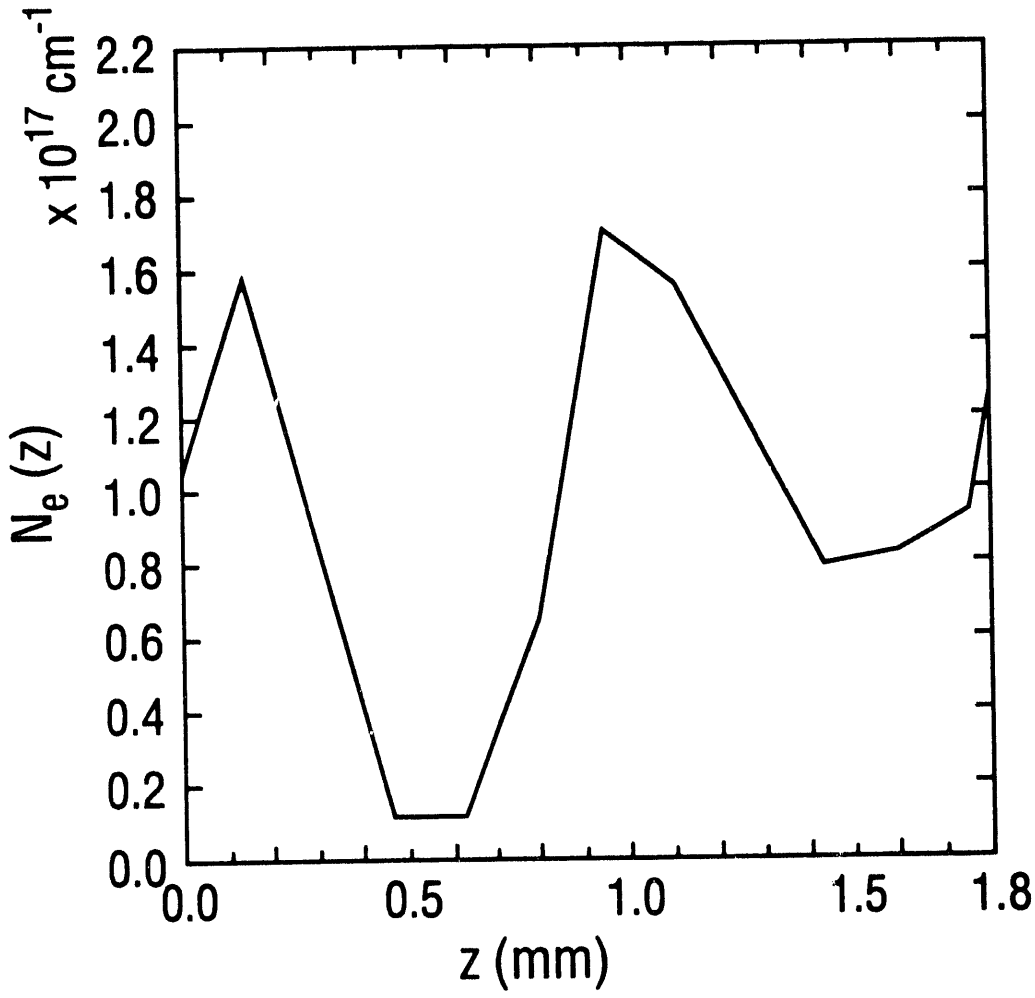

Fig. 5c: Simulation line density, HDZP-I, 44 nsec (70 kA).

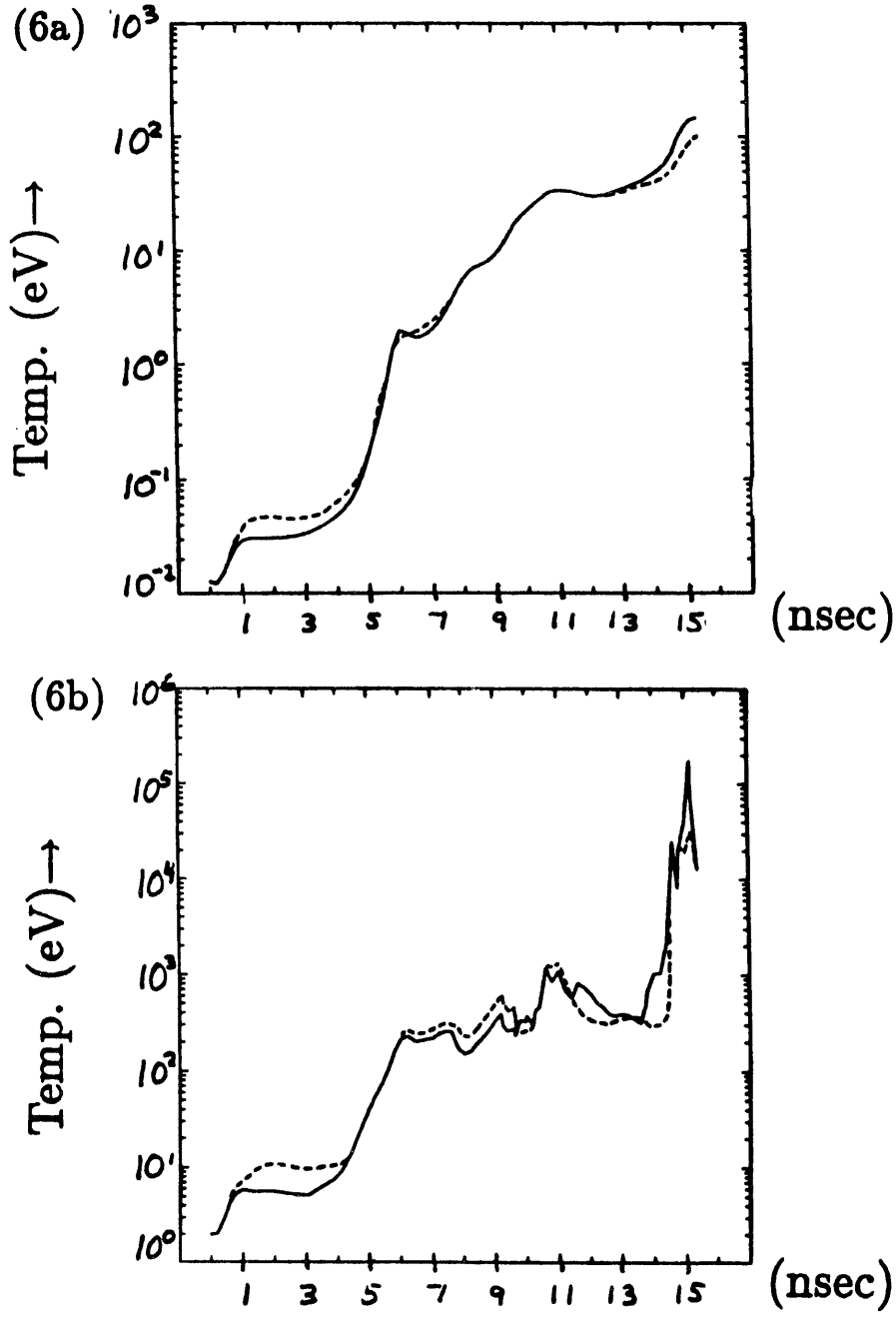

Figs. 6(a-b): Results of two-temperature HDZP-II simulations: (6a) Average (mass-weighted) electron (dotted) and ion (solid) temperatures (eV) vs. time (nsec); (6b) Peak electron (dotted) and ion (solid) temperatures (eV) vs. time (nsec).

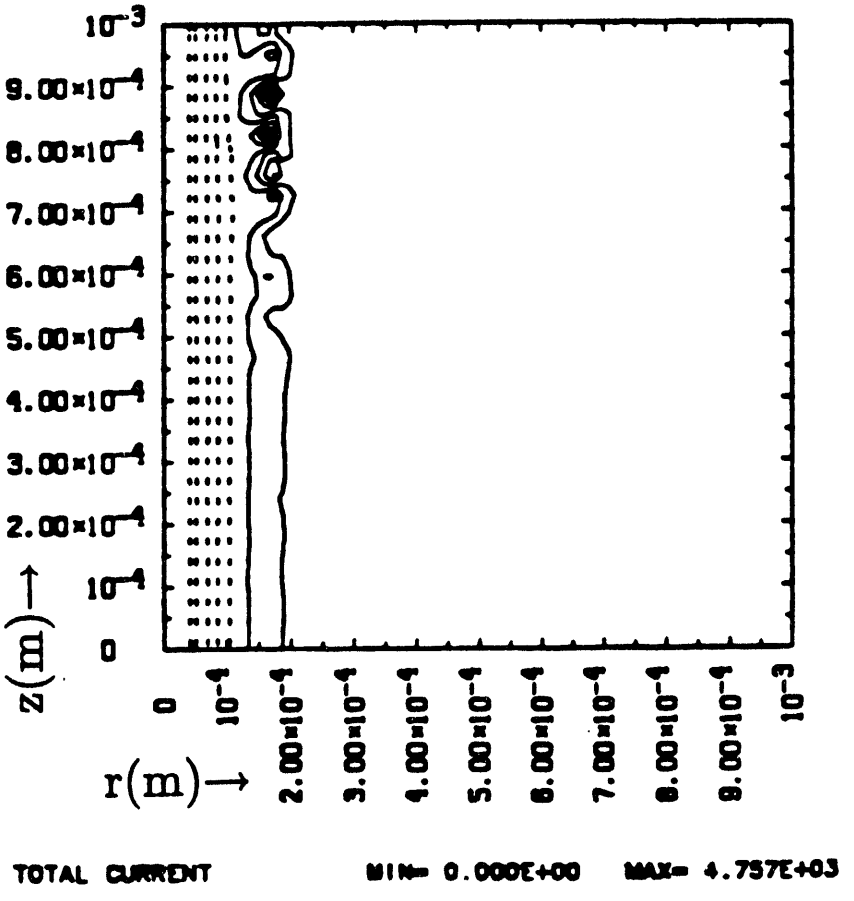

Figs. 7(a-b): Results of explicit Hall term HDZP-II simulations: (7a) Axial current contours, 2.6 nsec.

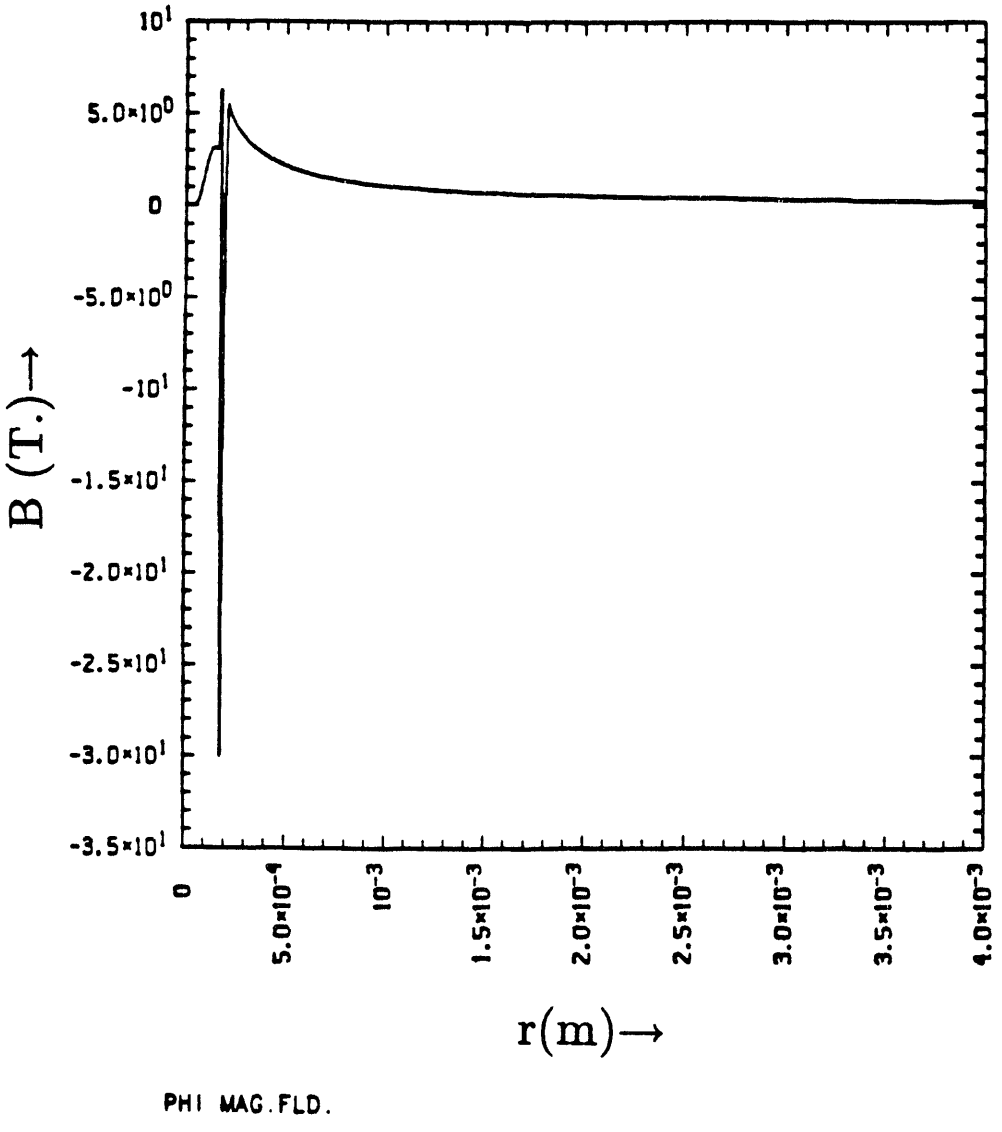

Fig. 7b: Magnetic field (Tesla) vs. radius (m) at axial midsection, 4 nsec.

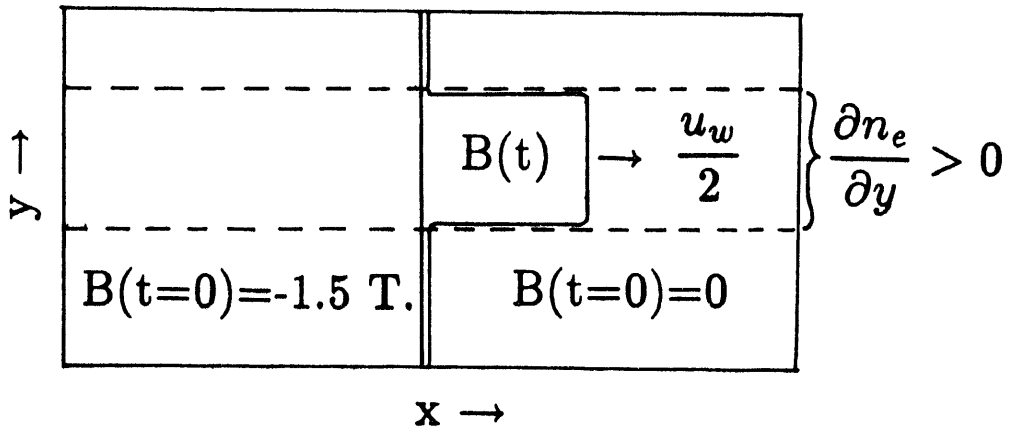

Fig. 8: KMC magnetic penetration problem: At time=0, perpendicular magnetic field is -1.5 Tesla on left half-plane and 0 on right half-plane; field penetrates at speed $u_w/2$ along density ramp channel for time>0.

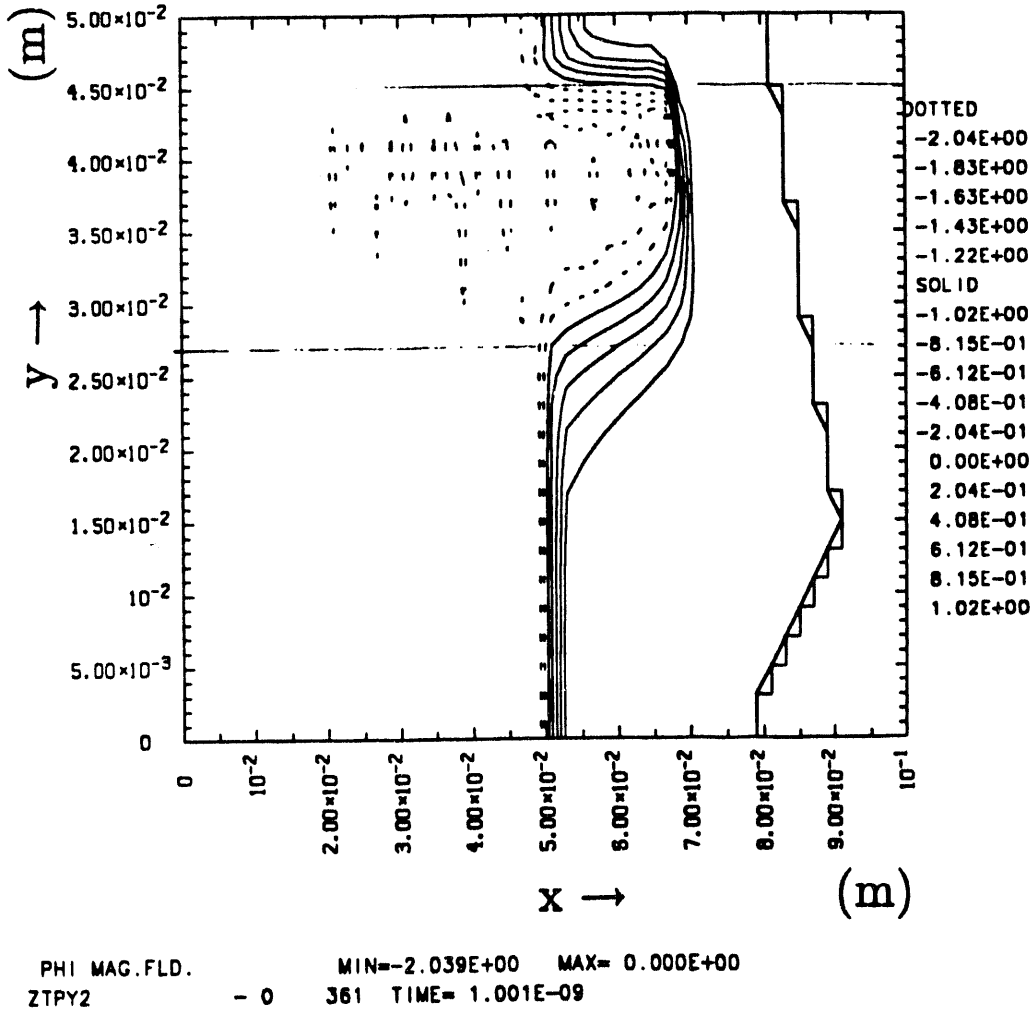

Figs. 9(a-c): KMC problem using implicit donor-cell Hall term: (9a) Magnetic penetration contours (field values in Tesla) at 1 nsec.

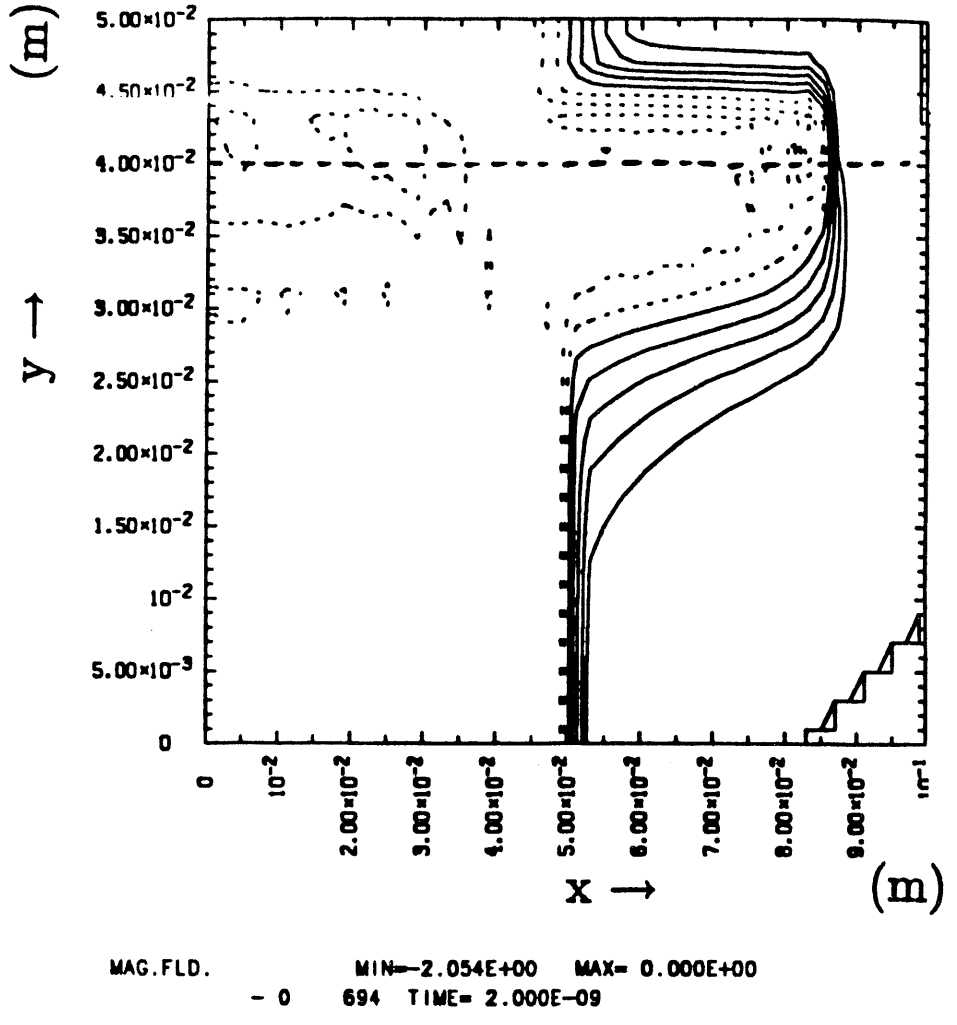

Fig. 9b: Magnetic penetration contours at 2 nsec.

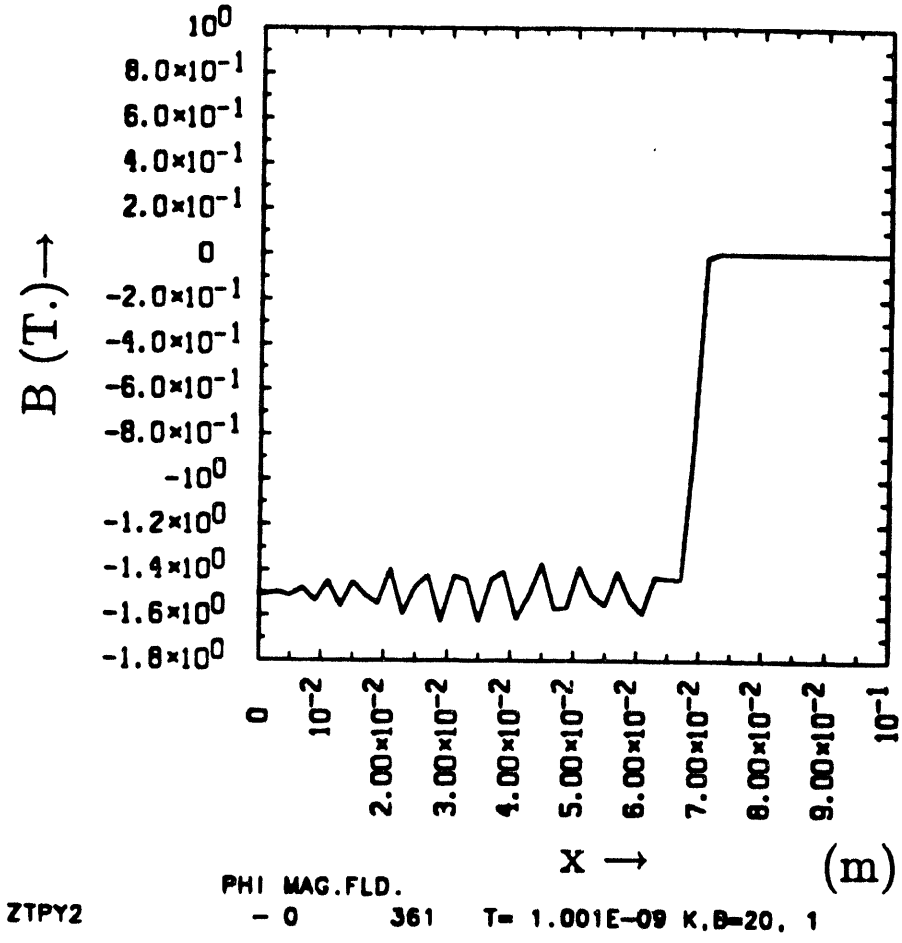

Fig. 9c: Magnetic field (Tesla) vs. distance x (m) along dotted line shown in Fig. 9b, where y=4 cm, at 1 nsec.

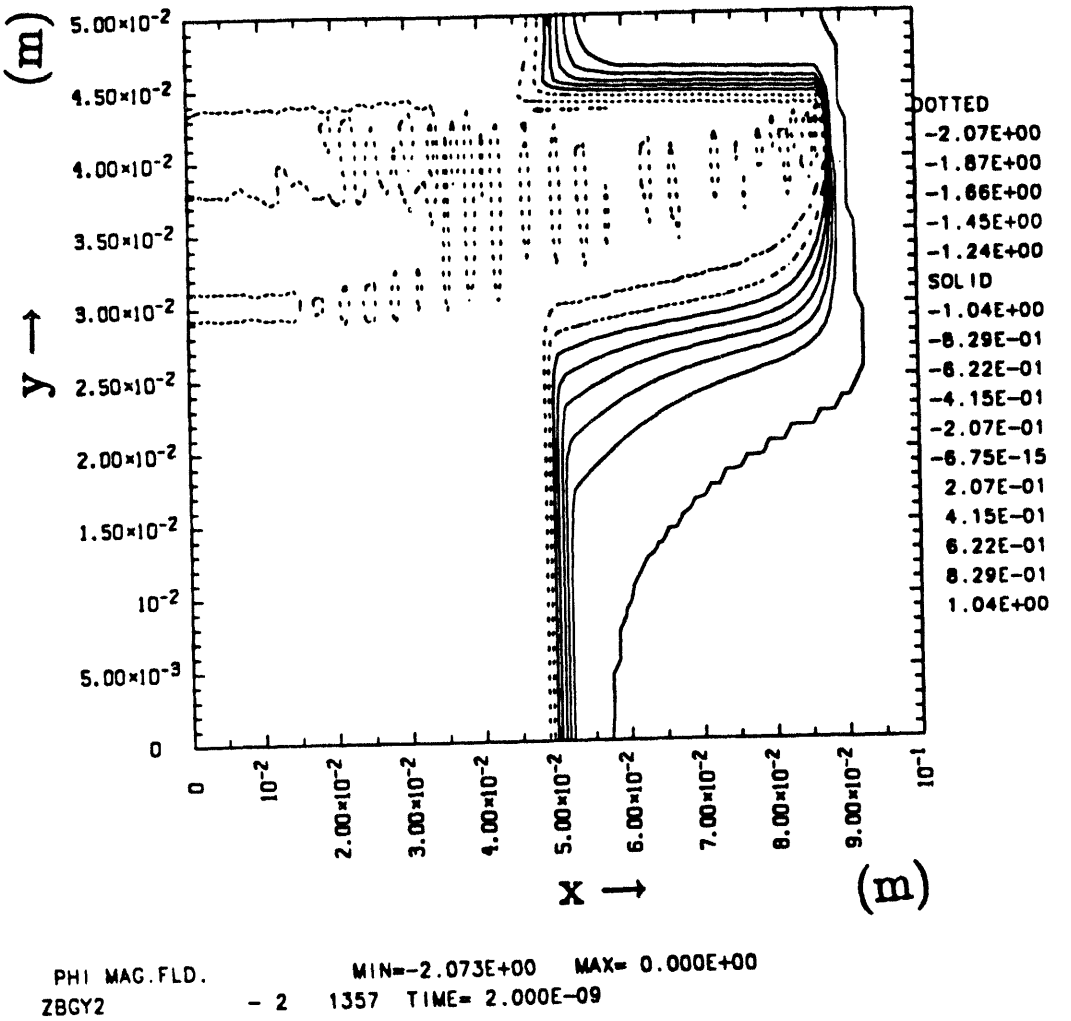

Fig. 10: KMC problem, implicit donor-cell Hall term, $\Delta x/2$ (finer spatial grid): Magnetic penetration contours (field values in Tesla) at 2 nsec.

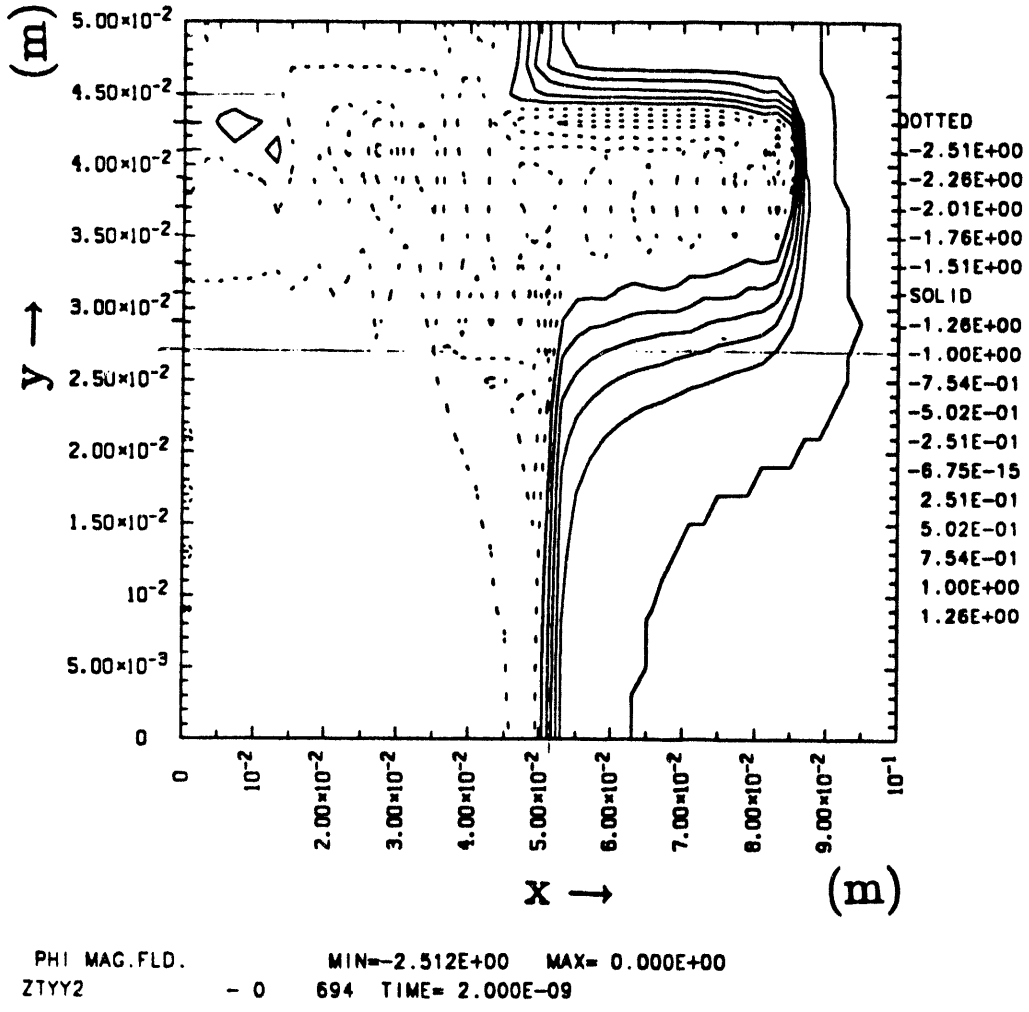

Fig. 11: KMC problem, implicit hybrid donor-cell/space-centered Hall term: Magnetic penetration contours (field values in Tesla) at 2 nsec.

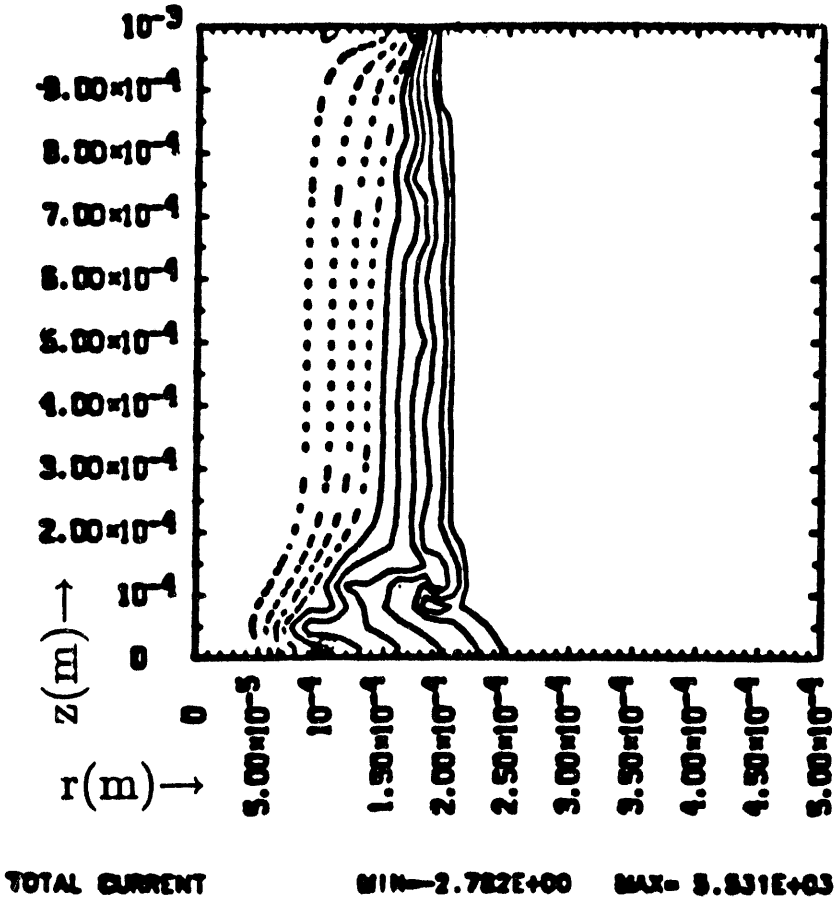

Figs. 12(a-b): Hall MHD axial boundary effects (HDZP-II simulation): (12a) Axial current contours "pinched" at anode (bottom), 4 nsec.

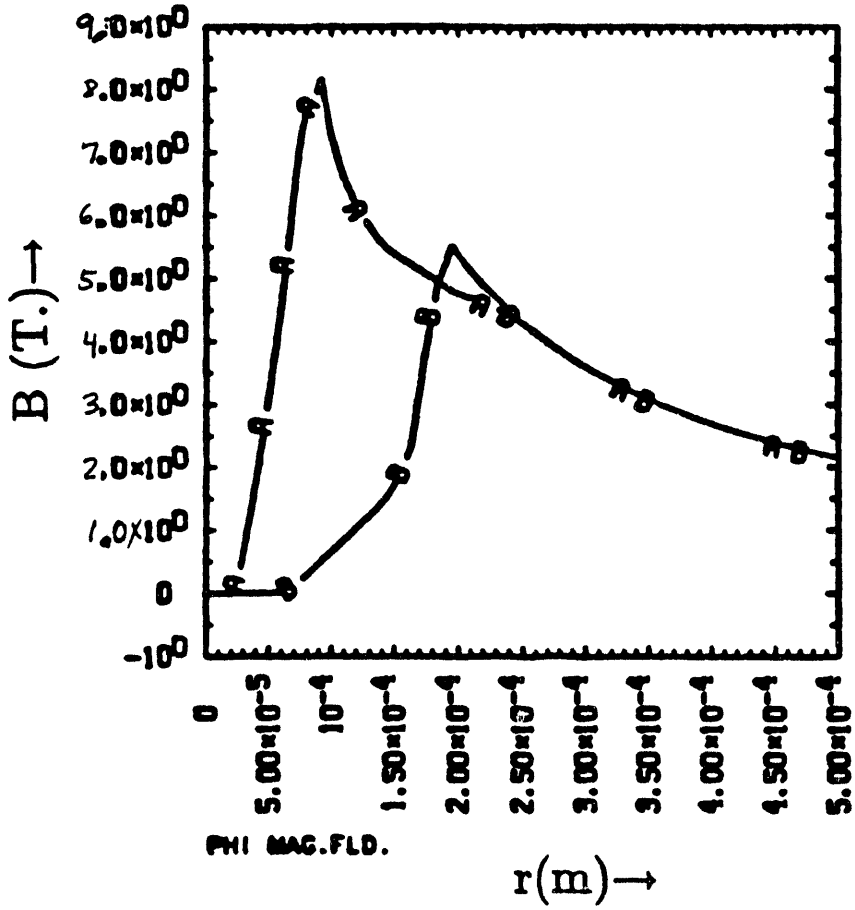

Fig. 12b: Magnetic field (Tesla) vs. radius (m) for axial locations adjacent to anode (line A) and cathode (line B); "piling-up" at anode, 4 nsec.

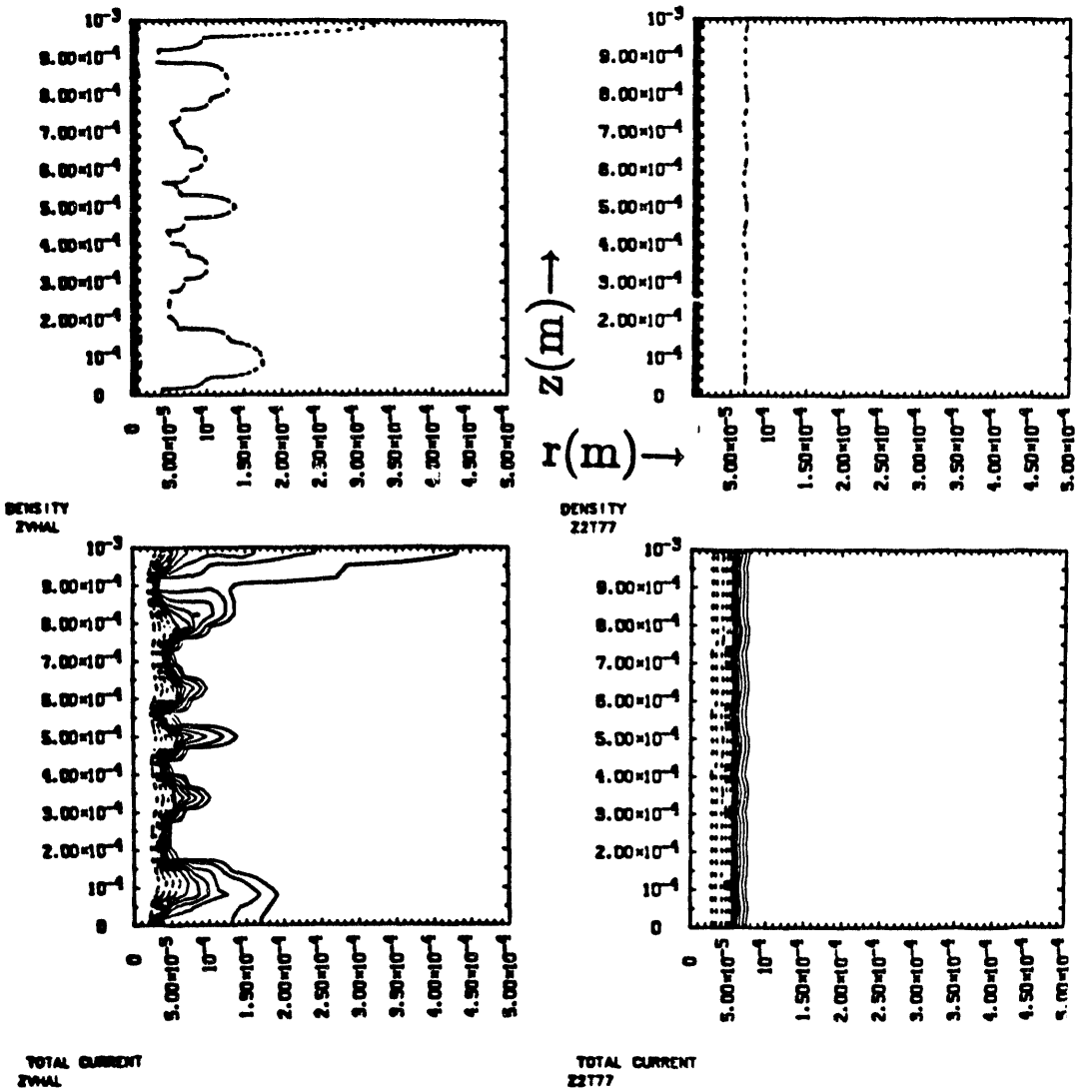

Fig. 13: Density (top) and axial current (bottom) contours, HDZP-II simulations (8 nsec), with (left) and without (right) Hall term: Hall-driven small-wavelength instability development.

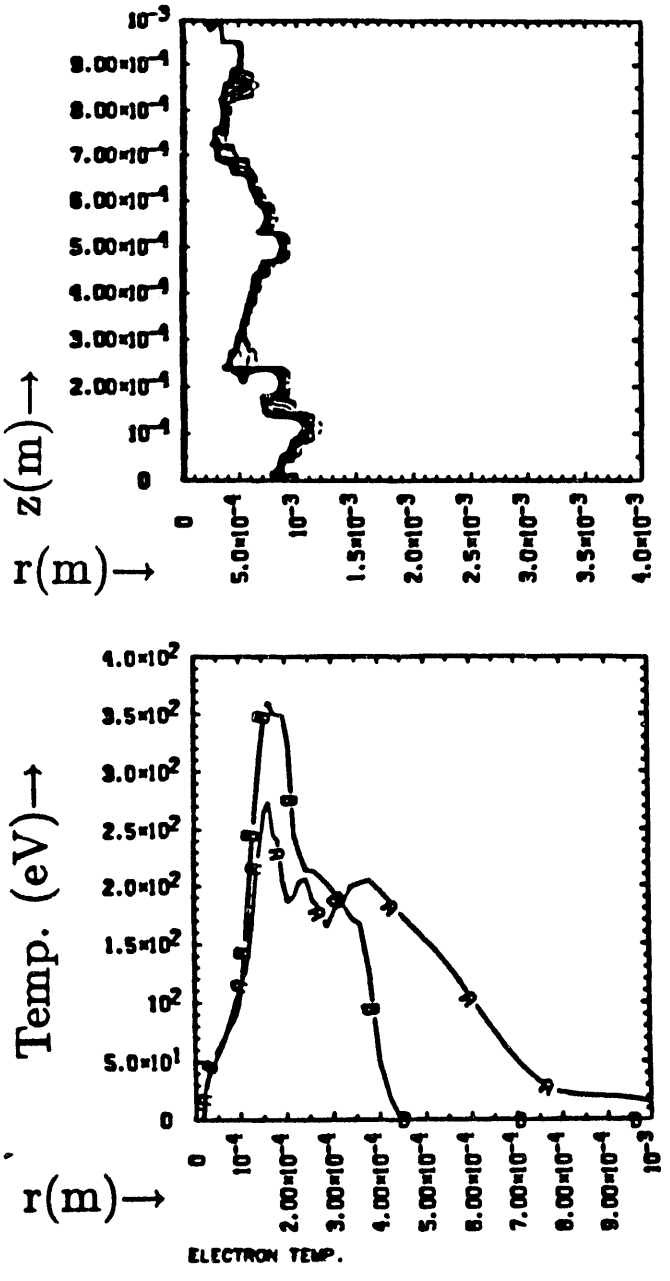

Fig. 14: Full "Hall MHD" model energy convection in $-\vec{J}$ direction: HDZP-II simulation (6.5 nsec); (top) temperature contours; (bottom) temperature (eV) vs. radius (m) for axial locations adjacent to anode (line A) and cathode (line B).

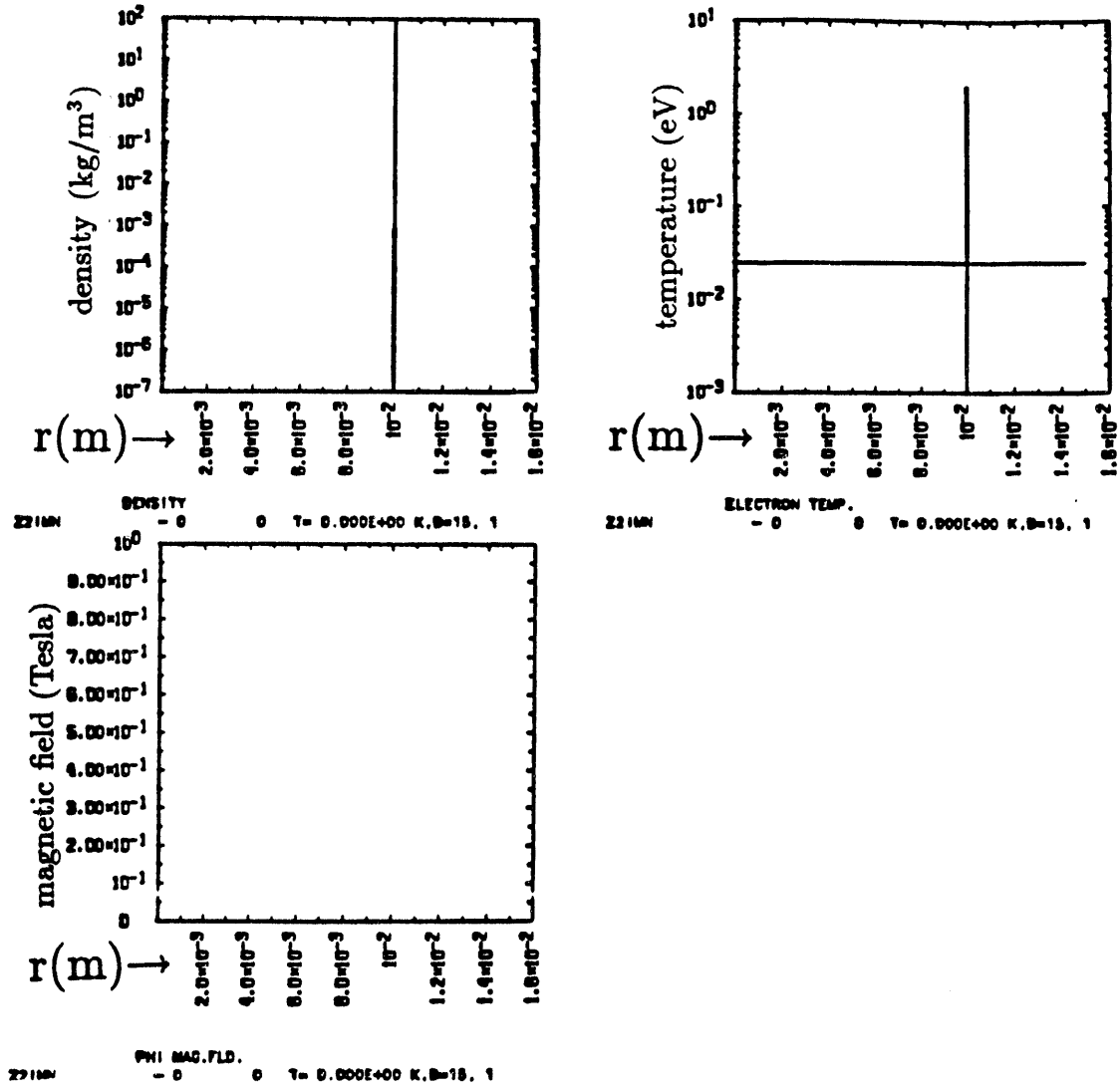

Fig. 15: Initial conditions for deuterium shell implosion simulations: density (kg/m^3), temperature (eV), and magnetic field (Tesla) vs. radius (m) at axial midsection.

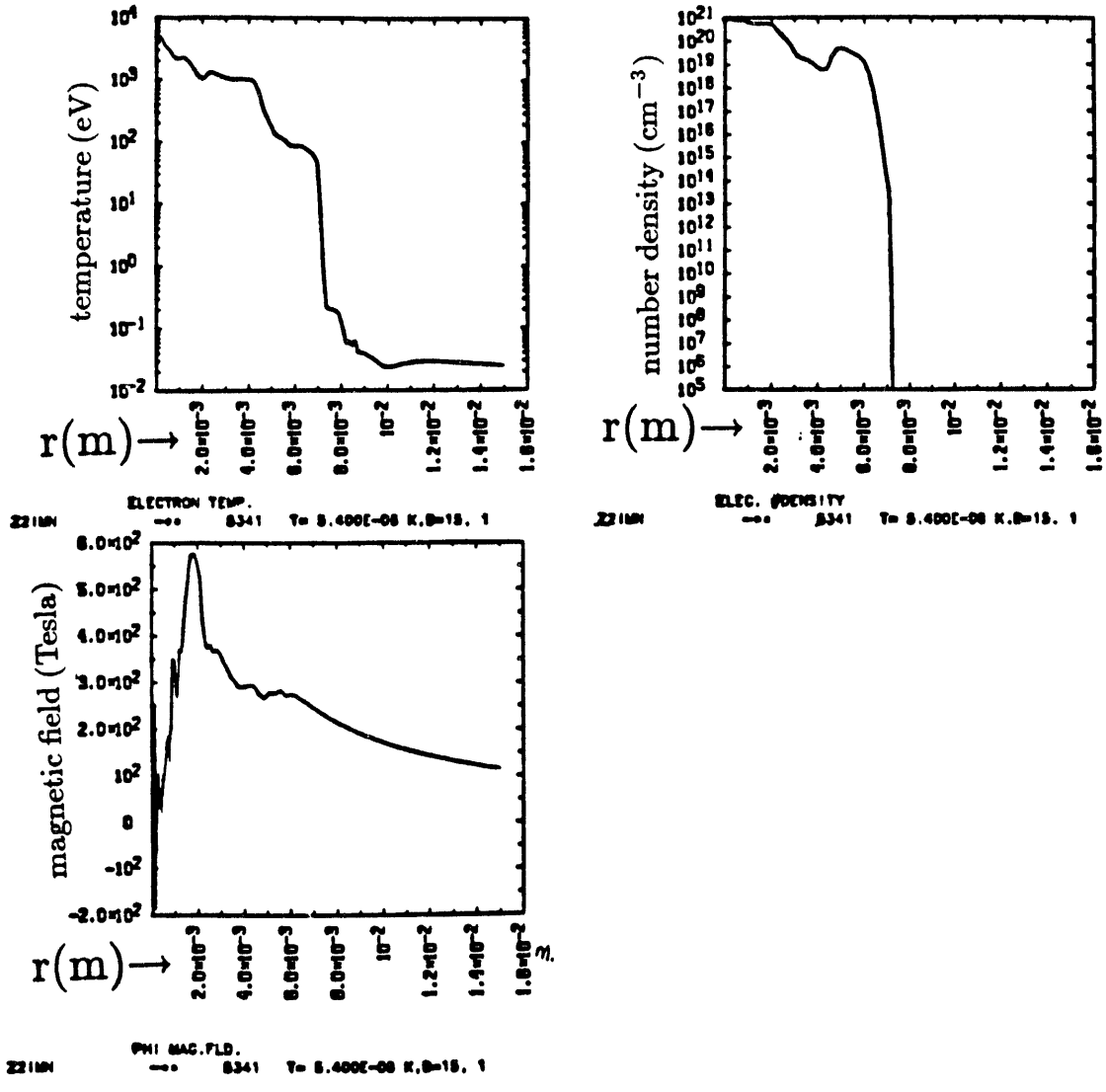

Fig. 16: Conditions at peak convergence of deuterium shell implosion simulation (54 nsec): temperature (eV), magnetic field (Tesla), and number density (cm^{-3}) vs. radius (m) at axial midsection.

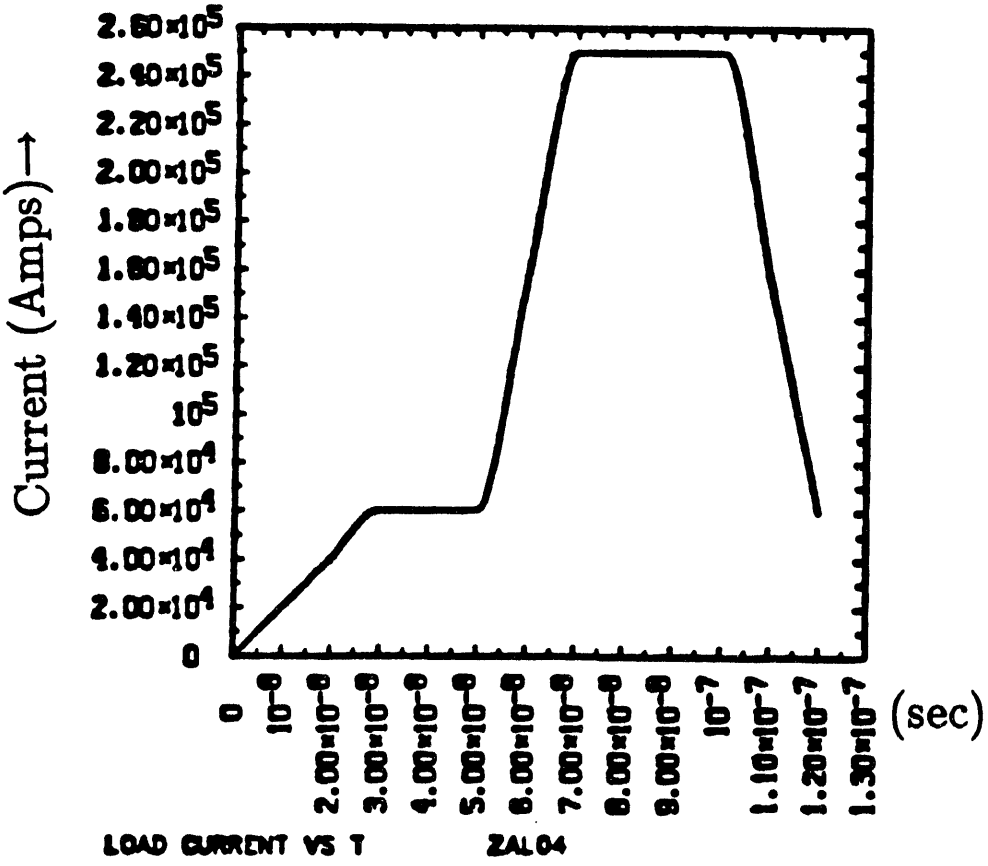

Fig. 17: Experimentally prescribed current (Amps) vs. time (sec) for all-aluminum POW simulation.

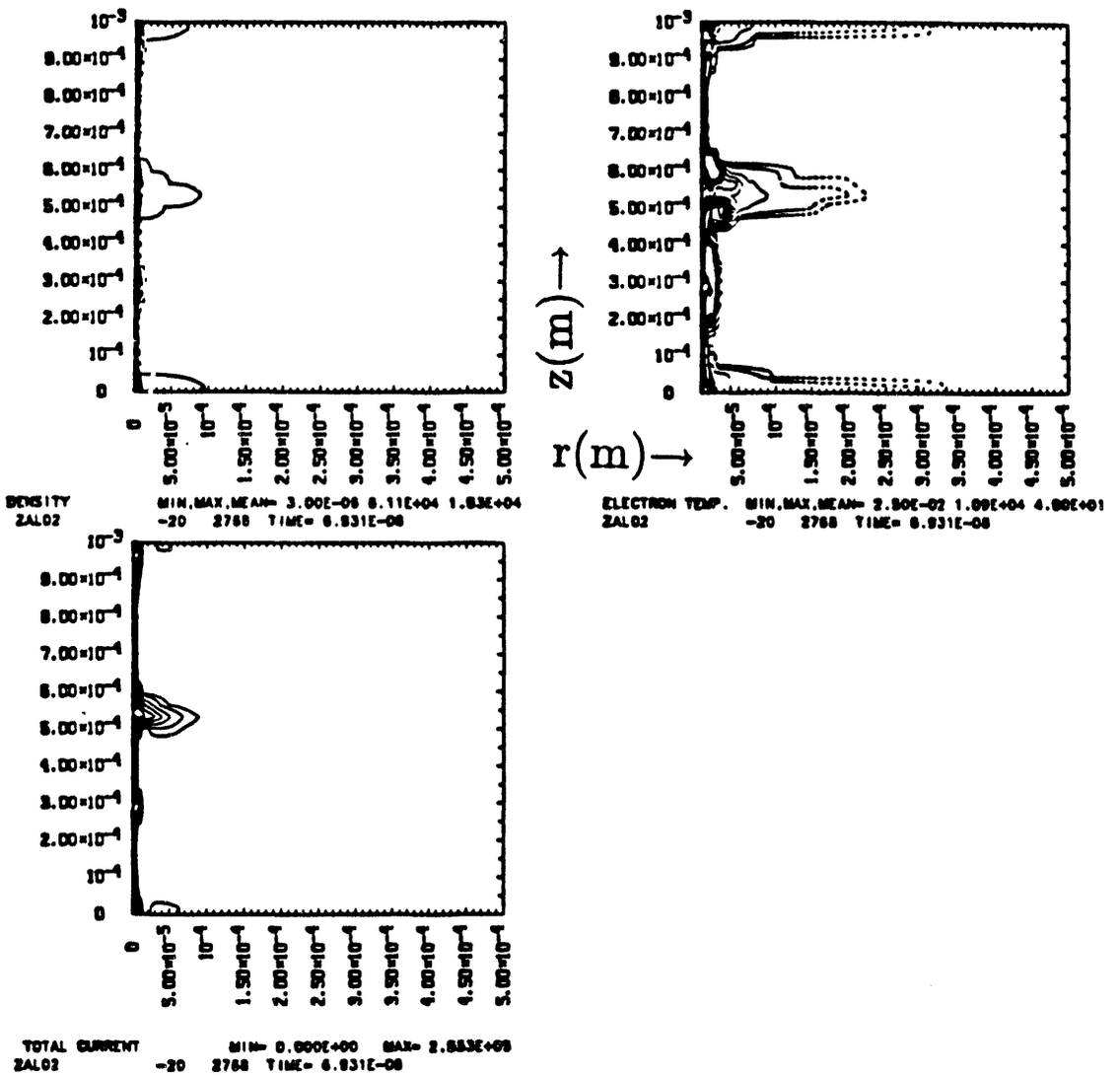

Fig. 18: Aluminum "exploding-wire" simulation, ~69 nsec: density, temperature, current contours.

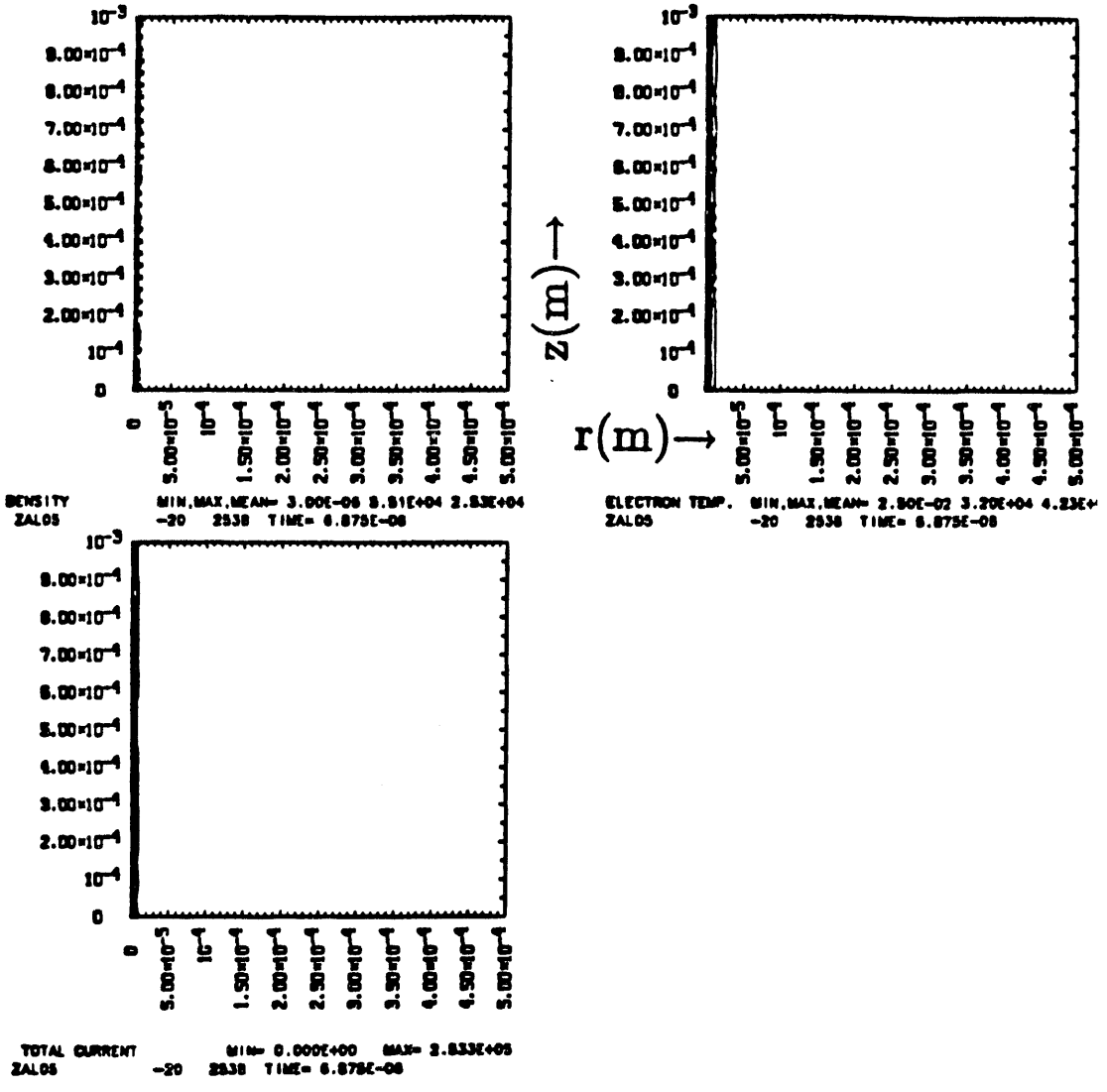

Fig. 19: Aluminum POW simulation, ~69 nsec: density, temperature, current contours.

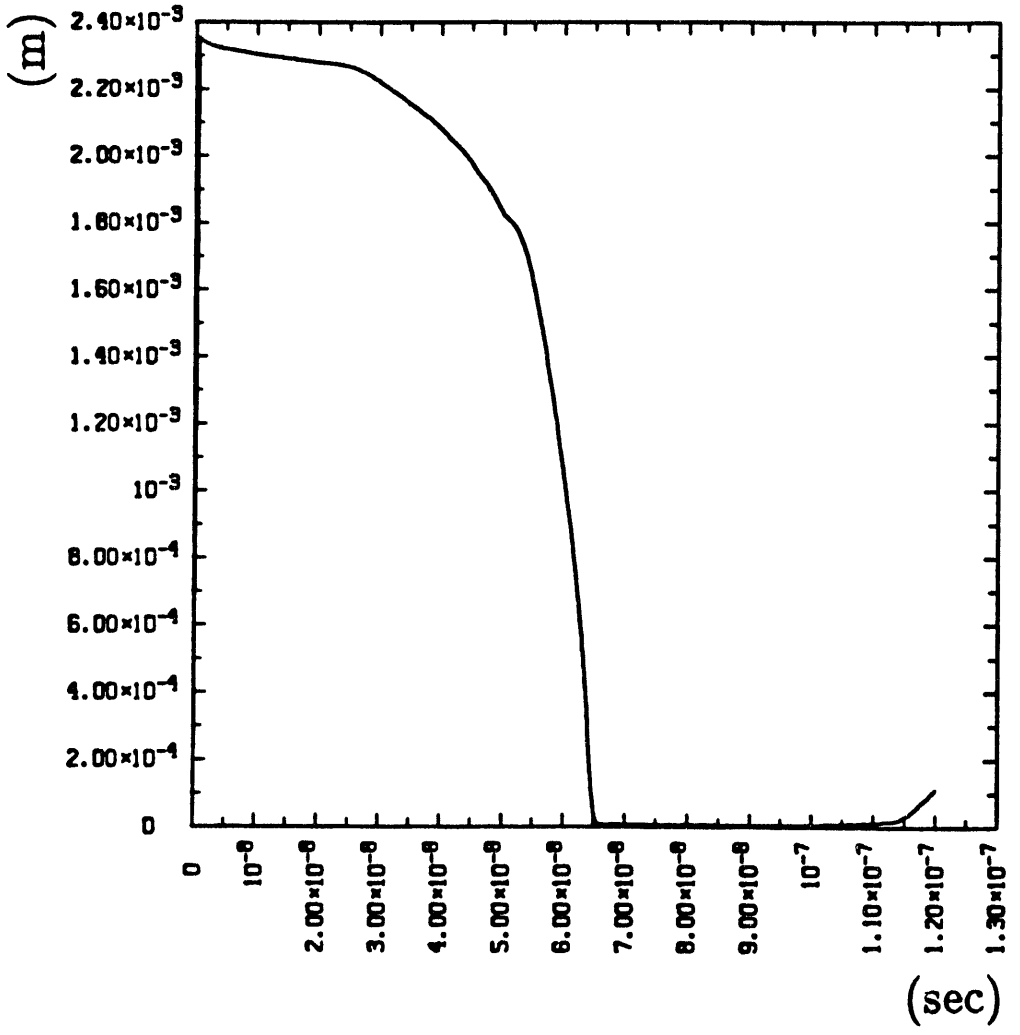

Figs. 20(a-b): Radius (m) within which 90% of total axial current is contained vs. time (sec), 1-d POW simulations: (20a) Aluminum POW simulation.

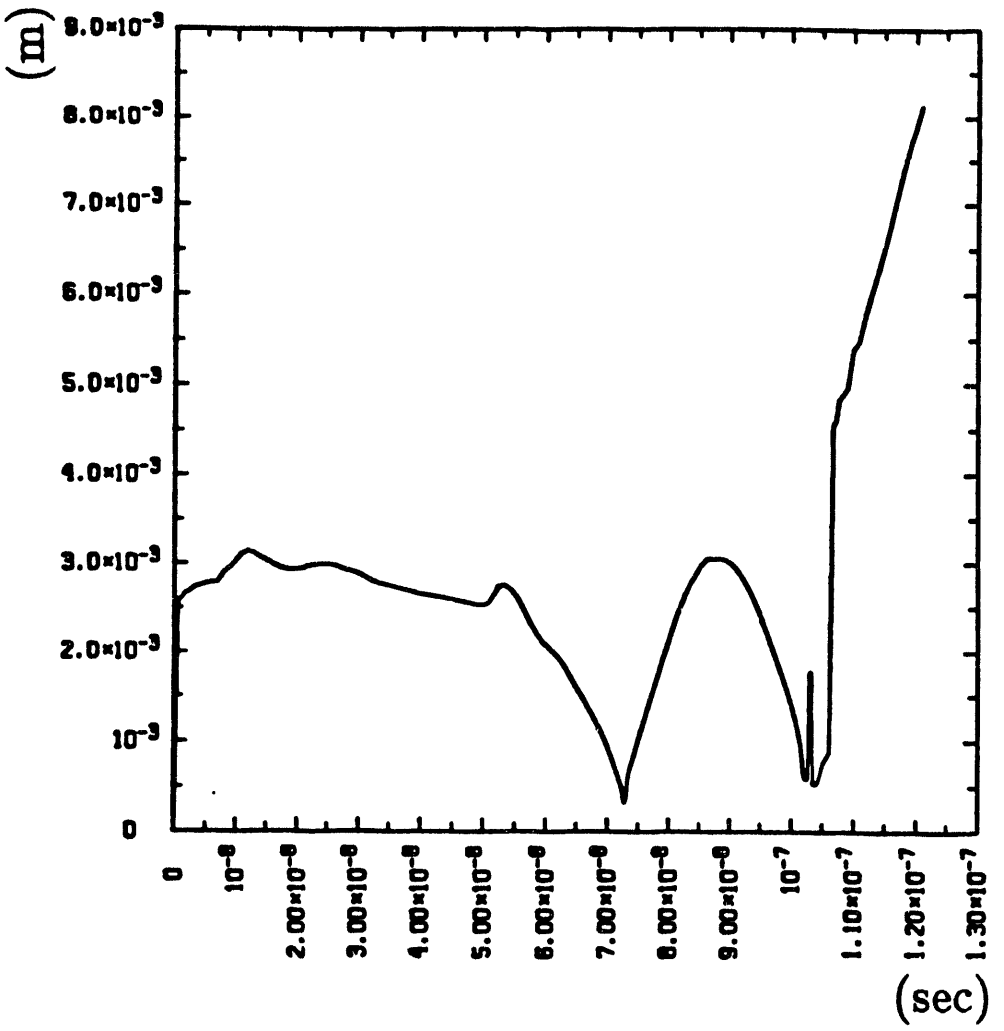

Fig. 20b: Deuterium POW simulation.

REFERENCES:

1. An excellent account and bibliography of early Z-pinch theory and experiment can be found in Chapters 3 and 7 of S. Glasstone and R. H. Lovberg, Controlled Thermonuclear Reactions (R. E. Krieger Publishing Co., Malabar, Florida, reprint 1975); additional fundamental papers on the Z-pinch include References 5-7, 18, and 87.
2. J. D. Sethian, A. E. Robson, K. A. Gerber, and A. W. DeSilva, Phys. Rev. Lett. **59**, 892 (1987); **59**, 1790(E) (1987).
3. J. E. Hammel and D. W. Scudder, in Proceedings of the Fourteenth European Conference on Controlled Fusion and Plasma Physics, Madrid, Spain, 1987, edited by F. Engelmann and J. L. Alvarez Rivas (European Physical Society, Petit-Lancy, Switzerland, 1987), p. 450.
4. J. E. Hammel, in Dense Z-Pinches, edited by N. R. Pereira, J. Davis, and N. Rostoker (American Institute of Physics, New York, 1989), p. 303.
5. R. S. Pease, Proc. Phys. Soc. B **70**, 11 (1957).
6. S. I. Braginskii, Sov. Phys. JETP **6**, 494 (1958).
7. N. R. Pereira, Phys. Fluids B **2**, 677 (1990).
8. R. L. Hagenson, A. S. Tai, R. A. Krakowski, and R. W. Moses, Nucl. Fusion **21**, 1351 (1981).
9. J. E. Hammel, D. W. Scudder, and J. S. Shlachter, Nucl. Inst. Meth. **207**, 161 (1983).
10. A. E. Robson, in Dense Z-Pinches (Ref. 4), p. 362.
11. M. G. Haines, Proc. Phys. Soc. **76**, 250 (1960).
12. See National Technical Information Service Document No. LA-6203-MS (J. E. Hammel, Los Alamos National Laboratory Report No. LA-6203-MS

(1976); NTIS Prices: PC A02/MF A01). Copies may be ordered from the National Technical Information Service, Springfield, VA 22161.

13. J. D. Sethian, A. E. Robson, K. A. Gerber, and A. W. DeSilva, in Physics of Alternative Magnetic Confinement Schemes, Proceedings of the Workshop Held at Varenna, Italy, 1990, edited by S. Ortolani and E. Sindoni (Societa Italiana di Fisica, Editrice Compositori, Bologna, 1991), p. 511.
14. D. W. Scudder, J. S. Shlachter, J. E. Hammel, F. Venneri, R. Chrien, R. Lovberg, R. Riley, in Physics of Alternative Magnetic Confinement Schemes (Ref. 13), p. 519.
15. M. G. Haines, in Physics of Alternative Magnetic Confinement Schemes (Ref. 13), p. 277.
16. Numerous theoretical and computational investigations, including early work by this author, have suggested m=1 growth rate reduction or stabilization for given plasma profiles (see, for example, Refs. 21-23,25,26,30); none have made a definitive link between these results and actual experiments, which is the intent of the present work, for the m=0 mode.
17. E. S. Figura, G. H. McCall, and A. E. Dangor, Phys. Fluids B **3**, 2835 (1991).
18. B. B. Kadomtsev, in Reviews of Plasma Physics, edited by M. A. Leontovich (Consultants Bureau, New York, 1966), Vol. 2, p. 165.
19. M. Coppins, D. J. Bond, and M. G. Haines, Phys. Fluids **27**, 2886 (1984).
20. M. Coppins, Phys. Fluids B **1**, 591 (1989).
21. I. D. Culverwell and M. Coppins, Phys. Fluids B **2**, 129 (1990).
22. M. G. Haines and M. Coppins, Phys. Rev. Lett. **66**, 1462 (1991).

23. A. H. Glasser, J. E. Hammel, H. R. Lewis, I. R. Lindemuth, R. H. Lovberg, G. H. McCall, R. A. Nebel, P. Rosenau, D. W. Scudder, P. T. Sheehey, and J. S. Shlachter, in Plasma Physics and Controlled Nuclear Fusion Research 1988 (IAEA Vienna, 1989), Vol. 2, p. 557.
24. F. L. Cochran and A. E. Robson, Phys. Fluids B **2**, 123 (1990).
25. G. O. Spies, Plasma Phys. Controlled Fusion **30**, 1025 (1988).
26. P. M. Cox, Plasma Phys. Controlled Fusion **32**, 553 (1990).
27. M. Coppins and J. Scheffel, Phys. Fluids B **4**, 3251 (1992).
28. J. Scheffel, T. Arber, and M. Coppins, in Proceedings of the Third International Conference on Dense Z-Pinches (London, England, April 1993; in press).
29. F. L. Cochran and A. E. Robson, Phys. Fluids B **5**, 2905 (1993).
30. A. H. Glasser and R. A. Nebel, in Dense Z-Pinches (Ref. 4), p. 226.
31. S. I. Braginskii, in Reviews of Plasma Physics, edited by M. A. Leontovich (Consultants Bureau, New York, 1965), Vol. 1, p. 205.
32. D. D. Schnack, D. C. Barnes, Z. Mikic, D. S. Harned, E. J. Caramana, and R. A. Nebel, Comp. Phys. Comm. **43**, 17 (1986).
33. S. I. Braginskii, in Reviews of Plasma Physics (Ref. 31), p. 218, 252.
34. S. I. Braginskii, in Reviews of Plasma Physics (Ref. 31), p. 250-253.
35. I. R. Lindemuth, G. H. McCall and R. A. Nebel, Phys. Rev. Lett. **62**, 264 (1989).
36. I. R. Lindemuth, Phys. Rev. Lett. **65**, 179 (1990).
37. I. R. Lindemuth, in Dense Z-Pinches (Ref. 4), p. 327.
38. See National Technical Information Service Document No. UCRL-52492 (I. R. Lindemuth, University of California Lawrence Livermore Laboratory

Report UCRL-52492 (1979); NTIS Prices: PC E02/MF A01). Copies may be ordered from the National Technical Information Service, Springfield, VA 22161.

39. See National Technical Information Service Document No. DE85011902/XAB (Los Alamos National Laboratory Report No. LA-10160-MS, edited by K. S. Holian (1984); NTIS Prices: PC A16/MF A01). Copies may be ordered from the National Technical Information Service, Springfield, VA 22161.
40. J. P. Freidberg, Ideal Magnetohydrodynamics (Plenum Press, New York, 1987), Ch. 2.
41. M. G. Haines, J. Phys. D **11**, 1709 (1978).
42. R. Balescu, Transport Processes in Plasmas (North-Holland Publishers, New York, 1988), Vol. 1 (Classical Transport Theory), p. 107.
43. R. Balescu, in Transport Processes in Plasmas (Ref. 42), Vol. 1, Ch. 5.
44. S. I. Braginskii, in Reviews of Plasma Physics (Ref. 31), p. 233.
45. J. H. Ferziger, in Numerical Methods for Engineering Application (Wiley-Interscience, New York, 1981), p. 237.
46. F. F. Chen, in Introduction to Plasma Physics and Controlled Fusion, Second Edition (Plenum Press, New York, 1984), p. 89.
47. F. F. Chen, in Introduction to Plasma Physics and Controlled Fusion (Ref. 46), p. 10.
48. J. P. Freidberg, in Ideal Magnetohydrodynamics (Ref. 40), p. 16.
49. S. I. Braginskii, in Reviews of Plasma Physics (Ref. 31), p. 250.
50. J. P. Freidberg, in Ideal Magnetohydrodynamics (Ref. 40), p. 22.
51. R. Balescu, in Transport Processes in Plasmas (Ref. 42), Vol. 1, p. 253.

52. E. Bowers and M. G. Haines, Phys. Fluids **11**, 2695 (1968).

53. R. Balescu, in Transport Processes in Plasmas (Ref. 42), Vol. 1, p. 258.

54. M. G. Haines, in Proceedings of the Third International Conference on Dense Z-Pinches (Ref. 28).

55. D. R. Nicholson, in Introduction to Plasma Theory (John Wiley & Sons, New York, 1983), p. 192.

56. F. F. Chen, in Introduction to Plasma Physics and Controlled Fusion (Ref. 46), p. 179.

57. R. Balescu, in Transport Processes in Plasmas (Ref. 42), Vol. 1, p. 248.

58. S. I. Braginskii, in Reviews of Plasma Physics (Ref. 31), p. 222.

59. J. P. Chittenden and M. G. Haines, J. Phys. D **26**, 1048 (1993).

60. R. B. Bird, W. E. Stewart, and E. N. Lightfoot, in Transport Phenomena (John Wiley & Sons, New York, 1960), p. 730 (A.4-30).

61. I. R. Lindemuth, LLNL Report UCRL-52492 (Ref. 38), p. 10.

62. R. Balescu, in Transport Processes in Plasmas (Ref. 42), Vol. 1, p. 245.

63. S. I. Braginskii, in Reviews of Plasma Physics (Ref. 31), p. 249, 250.

64. S. I. Braginskii, in Reviews of Plasma Physics (Ref. 31), p. 217, 273.

65. T. J. Dolan, in Fusion Research (Pergamon Press, New York, 1982), Vol. 1, p. 43.

66. J. D. Huba, J. G. Lyon, and A. B. Hassam, Phys. Rev. Lett. **59**, 2971 (1987).

67. A. S. Kingsep, Yu. V. Mokhov, and K. V. Chukbar, Sov. J. Plasma Phys. **10**, 495 (1984).

68. M. G. Haines, Proc. Phys. Soc. **77**, 643 (1961).

69. M. G. Haines, Plasma Phys. Contr. Fusion **31**, 759 (1989).

70. M. G. Haines, J. Phys. D **11**, 1709 (1978).

71. J. P. Freidberg, in Ideal Magnetohydrodynamics (Ref. 40), p. 21, 22.

72. F. F. Chen, in Introduction to Plasma Physics and Controlled Fusion (Ref. 46), p. 1.

73. The formulas for λ_D, ω_{pe}, etc. in section 2.5 are largely taken from two sources: F. F. Chen, in Introduction to Plasma Physics and Controlled Fusion (Ref. 46), p. 351, and D. L. Book, in NRL Plasma Formulary (Naval Research Laboratory Publication 177-4405, Washington, D. C., 1990), p. 28.

74. J. H. Ferziger, in Numerical Methods for Engineering Application (Ref. 45), p. 255.

75. J. Douglas and J. Gunn, Num. Math. **6**, 628 (1964).

76. J. H. Ferziger, in Numerical Methods for Engineering Application (Ref. 45), p. 253.

77. I. R. Lindemuth, J. Comp. Phys. **18**, 119 (1975).

78. I. R. Lindemuth, in LLNL Report UCRL-52492 (Ref. 38), p. 26.

79. I. R. Lindemuth, Appl. Phys. Lett. **40**, 462 (1982).

80. J. H. Ferziger, in Numerical Methods for Engineering Application (Ref. 45), p. 162, etc.

81. I. R. Lindemuth, J. Comp. Phys. **25**, 104 (1977).

82. P. Sheehey, I. R. Lindemuth, R. H. Lovberg, and R. Riley Jr., in Beams '92, Proceedings of the Ninth International Conference on High-Power Particle Beams, edited by D. Mosher and G. Cooperstein (National Technical Information Service NTIS PB92-206168, Springfield, VA, 1992), Vol. 3, p. 1990.

83. P. Sheehey, J. Hammel, I. Lindemuth, R. Lovberg, R. Riley Jr., D. Scudder, and J. Shlachter, Phys. Fluids B **4**, 3698 (1992).

84. P. Sheehey and I. R. Lindemuth, in Proceedings of the Third International Conference on Dense Z-Pinches (Ref. 28).

85. P. Rosenau, R. A. Nebel, and H. R. Lewis, Phys. Fluids B **1**, 1233 (1989).

86. M. Coppins, I. D. Culverwell, and M. G. Haines, Phys. Fluids **31**, 2688 (1989).

87. W. H. Bennett, Phys. Rev. **45**, 890 (1934).

88. N. A. Bobrova, T. L. Razinkova, and P. V. Sasorov, in Megagauss Fields and Pulsed Power Systems, edited by V. M. Titov and G. A. Shvetsov (Nova Science Publishers, New York, 1990), p. 725; also same authors (private communication, 1992).

89. R. H. Lovberg, in Proceedings of the Third International Conference on Dense Z-Pinches (Ref. 28).

90. J. P. Chittenden, in Proceedings of the Third International Conference on Dense Z-Pinches (Ref. 28).

91. I. R. Lindemuth, R. C. Kirkpatrick, R. E. Reinovsky, P. T. Sheehey, R. S. Thurston, and F. J. Wysocki, in Proceedings of the Sixth International Conference on Megagauss Magnetic Field Generation and Related Topics (Albuquerque, New Mexico, November, 1992; in press).

92. I. R. Lindemuth and R. C. Kirkpatrick, Nucl. Fusion **23**, 263 (1983).

93. W. Kies, H. Bachmann, K. Baumung, J. M. Bayley, H. Bluhm, G. Decker, M. Malzig, D. Rusch, W. Ratajczak, O. Stoltz, C. van Calker, J. Westheide, and G. Ziethen, J. Appl. Phys. **70**, 7261 (1991).

94. F. J. Wessel, B. Etlicher, and P. Choi, Phys. Rev. Lett. **69**, 3181 (1992);

also see P. Choi, et al, and V. Smirnov, et al, in Proceedings of the Third International Conference on Dense Z-Pinches (Ref. 28).

95. J. H. Ferziger, in Numerical Methods for Engineering Application (Ref. 45), p. 60.
96. J. H. Ferziger, in Numerical Methods for Engineering Application (Ref. 45), p. 235.
97. R. J. Mason, P. L. Auer, R. N. Sudan, B. V. Oliver, C. E. Seyler, and J. B. Greenly, Phys. Fluids B **5**, 1 (1993).
98. J. H. Ferziger, in Numerical Methods for Engineering Application (Ref. 45), p. 246.
99. J. H. Ferziger, in Numerical Methods for Engineering Application (Ref. 45), p. 237.
100. P. J. Roache, in Computational Fluid Dynamics (Hermosa Publishers, Albuquerque, 1982), p. 67.
101. P. J. Roache, in Computational Fluid Dynamics (Ref. 100), p. 46.
102. J. H. Ferziger, in Numerical Methods for Engineering Application (Ref. 45), p. 141, etc.
103. P. J. Roache, in Computational Fluid Dynamics (Ref. 100), p. 42, etc.
104. J. H. Ferziger, in Numerical Methods for Engineering Application (Ref. 45), p. 236, 241; also see P. J. Roache (Ref. 100).
105. B. Van Leer, J. Comp. Phys. **23**, 276 (1977).
106. J. P. Boris and D. L. Book, J. Comp. Phys. **20**, 397 (1976).
107. M. G. Haines (private communication, 1993).
108. V. V. Vikhrev and O. Z. Zabajdullin, in Proceedings of the Third International Conference on Dense Z-Pinches (Ref. 28); also, V. V. Vikhrev (pri-

vate communication, 1993).

109. D. H. McDaniel, M. K. Matzen, E. J. McGuire, T. J. Nash, R. B. Spielman, J. Seamen, S. F. Lopez, J. S. McGurn, L. Ruggles, T. L. Gilliland, D. Jobe, and M. Vargas, in Beams '92 Program Abstracts, Ninth International Conference on High-Power Particle Beams (Washington, D. C., 1992), p. 97.

110. P. B. Parks, in Physics of Alternative Magnetic Confinement Schemes (Ref. 13), p. 1083.

111. R. B. Spielman, T. H. Martin, D. H. McDaniel, M. Savage, A. W. Sharpe, and H. N. Woodall, in Proceedings of the Sixth International Conference on Megagauss Magnetic Field Generation and Related Topics (Ref. 91).

112. B. Etlicher (private communication, 1993).

113. F. C. Jahoda and G. A. Sawyer, in Methods of Experimental Physics Part B, edited by R. Lovberg and H. Griem (Academic Press, New York, 1971), Ch. 11.

114. L. D. Landau, E. M. Lifshitz, and L. P. Pitaevskii, Electrodynamics of Continuous Media, Second Edition (Pergamon Press, New York, 1984), p. 291.

115. P. C. Souers, Hydrogen Properties for Fusion Energy (University of California Press, Berkeley, 1986), p. 70.

116. See National Technical Information Service Document No. DE86048592/ XAB (A. C. Hindmarsh, Argonne National Laboratory/ National Energy Software Center Report No. ANL/NESC-592; NTIS Price: CP T15). Copies may be ordered from the National Technical Information Service, Springfield, VA 22161.

117. J. P. Freidberg, in Ideal Magnetohydrodynamics (Ref. 40), p. 54.

118. D. R. Nicholson, in Introduction to Plasma Theory (Ref. 55), p. 196.

119. A. S. Kingsep, K. V. Chukbar, and V. V. Yankov, in Reviews of Plasma Physics, edited by B. B. Kadomtsev (Consultants Bureau, New York, 1990), Vol. 16, p. 243.

120. F. F. Chen, in Introduction to Plasma Physics and Controlled Fusion (Ref. 46), p. 70.

121. F. F. Chen, in Introduction to Plasma Physics and Controlled Fusion (Ref. 46), p. 23.

•U.S. GOVERNMENT PRINTING OFFICE 1994-0-573-024/87066

END

DATE
FILMED
2/24/94